AMORPHOUS PHARMACEUTICAL SOLIDS: SURFACE ENRICHMENT OF COMPONENTS AND CONTROL OF LIQUID-CRYSTALLINE ORDER

by
Junguang Yu

A dissertation submitted in partial fulfillment of the requirements for the degree of

Doctor of Philosophy
(Pharmaceutical Sciences)

at the $\label{eq:consin-madison} \mbox{UNIVERSITY OF WISCONSIN-MADISON} \mbox{ } 2023$

Date of final oral examination: 10/25/2023

The dissertation is approved by the following members of the Final Examination Committee:

Lian Yu, Professor, School of Pharmacy

Mark D. Ediger, Professor, Department of Chemistry

Seungpyo Hong, Professor, School of Pharmacy

Quanyin Hu, Assistant Professor, School of Pharmacy

ACKNOWLEDGEMENTS

Upon completion of my doctoral dissertation, I would like to seize this moment to express my sincere gratitude to all those who have made meaningful contributions to my doctoral journey and enriched my experience at the University of Wisconsin-Madison.

First and foremost, I want to express my deepest gratitude to my advisor, Professor Lian Yu. Your dedication to the pursuit of good science has been a constant source of inspiration. You've not only pushed me to work hard but also encouraged me to think critically before diving into any promising research endeavor. Thank you for keeping me focused and teaching me the art of conducting science the right way. Your mentorship has not only sharpened my research skills but has also instilled in me a profound appreciation for science.

I feel deeply honored to have Professor Mark D. Ediger, Professor Seungpyo Hong, and Professor Quanyin Hu as my thesis committee members. Prof. Ediger, your insightful suggestions to our projects have been instrumental in advancing my scientific skills, and for that, I'm sincerely grateful. Prof. Hong, thank you for your valuable guidance on my thesis research. Prof. Hu, thank you for raising insightful questions that have enriched my research.

My experience in the Lian Yu lab would not have been complete without the incredible support of my fellow colleagues. I would like to express my gratitude towards Dr. Rattavut Teerakapibal, Dr. Chengbin Huang, Dr. Zhenxuan Chen, Dr. Yue Gui, Dr. Xin Yao, and Dr. Yuhui Li for their mentorship and support during my research. In addition, I would like to thank Dr. Travis Powell, Dr. Yinshan Chen and Dr. Men Zhu for the kind help and useful advice during my job search. I would also like to thank the current Yu lab members: Kennedy Borchardt-Setter, Amy Neusaenger, Caroline Fatina and Erika Jackson. Your contributions have been

indispensable in our projects, and I truly appreciate your support in our scientific explorations. I hope you all continue to find joy and success in your scientific pursuits.

My journey was further enriched by the opportunity to collaborate with talented scientists. I would like to extend my heartfelt appreciation to Dr. Feng Qian, whose guidance led me into the field of pharmaceuticals. I'm deeply grateful to Dr. Ranko Richert for our outstanding collaboration in the field of dielectric spectroscopy. A heartfelt thanks goes to Dr. Ilia Guzei for his invaluable assistance in conducting my X-ray scattering experiments. Also thanks for BMS collaborators, Dr. Yuchuan Gong, Dr. Chailu Que, Dr. Ho-wah Hui, and Dr. Lian Huang for the opportunity to explore the fascinating surface enrichment of components in amorphous formulation. Special thanks are due to my AbbVie internship mentors, Dr. Geoff Zhang and Dr. Xiaochun Lou, for their unwavering support and expert guidance throughout my internship.

I've had the privilege of forming some incredible friendships with people who've been there for me through thick and thin. I want to express my heartfelt thanks to Dr. Xihan Ji, Shi Chen, Dr. Shenyi Wang, Hongxuan Chen, Chengshuang Zhou, Ruxing Fu, Shiuan-Haur Su and Xuanxin Hu. Also, thanks to Hoyomix for their exceptional music, which never fails to brighten my day. Moreover, I couldn't have overcome the obstacles I faced without the love and support of my family. Their encouragement has been a tremendous driving force in keeping me moving forward. Thank you from the bottom of my heart for being there with me.

Table of Contents

Abstract	vii
Chapter 1: Introduction	1
1.1 Glass formation by cooling liquids	2
1.2 Surface segregation	3
1.3 Determination of surface composition by X-ray photoelectron spectroscopy	5
1.4 Anisotropic glasses	5
1.5 Contributions of this thesis	7
1.6 References	10
Chapter 2: Surface Enrichment of Surfactants in Amorphous Drugs: An X-Ray	
Photoelectron Spectroscopy Study	17
2.1 Abstract	18
2.2 Introduction	18
2.3 Experimental section	21
2.4 Results and discussion	23
2.5 Conclusions.	32
2.6 Acknowledgements	33
2.7 References	33
Chapter 3: Kinetics of Surface Enrichment of a Polymer in a Glass-Forming Mo	lecular
Liquid	37
3.1 Abstract	38
3.2 Introduction	38
3.3 Experimental section	40

3.4 Results and discussion	43
3.5 Conclusions	54
3.6 Acknowledgements	55
3.7 References	55
Chapter 4: Structures of Glasses Created by Multiple Kinetic Arrests	60
4.1 Abstract	61
4.2 Introduction	61
4.3 Experimental section	63
4.4 Results	65
4.5 Discussion	78
4.6 Conclusions	82
4.7 Acknowledgements	83
4.8 References	84
Chapter 5: Engineering the Glass Structure of a Discotic Liquid Crystal by	Multiple
Kinetic Arrests	88
5.1 Abstract	89
5.2 Introduction	89
5.3 Experimental section	92
5.4 Results and discussion	93
5.5 Conclusions	106
5.6 Acknowledgements	108
5.7 References	108
Chapter 6: Future Work	112

6.4 References	110
6.3 Aging of glasses created by multiple kinetic arrests	115
6.2 Surface distribution of surfactant enrichment in amorphous solid dispersion	114
6.1 Effects of surface enrichment of surfactants on surface crystallization and wetting	112

Abstract

This dissertation contributes to two areas of glass science: (1) surface enrichment of components in a multi-component glass and (2) glasses with tunable liquid-crystalline order.

Glasses have liquid-like uniformity and compositional flexibility and crystal-like strength, with numerous applications in optics, electronics, food science, and pharmaceutics. Amorphous drugs are more soluble and sometimes more bioavailable than crystalline drugs, providing a general tool for the delivery of poorly soluble drugs. In the first area, we show that the surface composition of an amorphous drug formulation can be vastly different from its bulk composition. A surfactant, a key formulation ingredient, can enrich strongly on the surface up to near purity and the degree of enrichment is controlled by the relative surface activities of the components. A polymer, another key ingredient, can also be surface-enriched with an enrichment rate governed by the rate of polymer diffusion through the bulk. The surface enrichment phenomenon impacts the stability and performance of amorphous formulations.

In the second area, we demonstrate that organic glasses can be prepared in which the liquid-crystalline (LC) order can be systematically controlled. For rod-like and discotic mesogens, the LC order in a glass is controlled by the kinetic arrest of a slow relaxation mode (end-over-end rotation for rods, head-to-tail flip for discs). As a result, each glass has not one, but two internal (fictive) temperatures, with the higher value associated with the regularity of molecular packing and the lower value with the spacing between molecules. Our finding helps understand the complex structure of a glass. Together these two contributions expand the tool box of glass engineering for applications in pharmaceutics and organic electronics.

Chapter 1

Introduction

Amorphous solids and glasses are important materials. A glass has liquid-like homogeneity and offers compositional flexibility, enabling its applications in optics and electronics. A glass has higher free energy than its crystalline counterpart, and therefore higher solubility, faster dissolution, and sometimes improved bioavailability. These benefits make amorphous formulations a useful tool for delivering poorly soluble drugs.

This dissertation is concerned with two areas of glass science: surface enrichment of components in amorphous solid dispersions and control of liquid-crystalline order. Chapter 1 provides background for this thesis. Chapter 2 reports the surface enrichment of surfactants in amorphous solid dispersions. Chapter 3 investigates the kinetics of surface enrichment. Chapter 4 studies the effect of multiple kinetic arrests on the structures of molecular glasses with liquid-crystalline order. Chapter 5 describes the glass engineering of a discotic liquid crystal by multiple kinetic arrests. Chapter 6 suggests future work that could benefit from the knowledge developed in this dissertation.

In this chapter, the following topics will be discussed: the glass formation process, surface segregation and its determination, and the control of liquid-crystalline order in glasses.

1.1 Glass formation by cooling liquids

When a liquid is cooled below its freezing point, crystallization may occur, leading to a sudden decrease of volume or enthalpy (Figure 1). If crystallization is avoided, a supercooled liquid forms⁶ and further cooling produces an amorphous solid, called a glass.⁷ The glass formation is a kinetic process and it is possible to prepare different glasses by different cooling rates.^{8,9} Typically at the glass transition temperature T_g , the liquid's relaxation time is about 100 s,¹⁰ and its bulk diffusion constant is about 10^{-20} m²/s.^{11,12}

Figure 2 illustrates the structural difference between a crystal and a glass, using SiO₂ as an example. Crystalline SiO₂ exhibits regular packing with both short- and long-range order, while amorphous SiO₂ only possesses short-range order.¹³

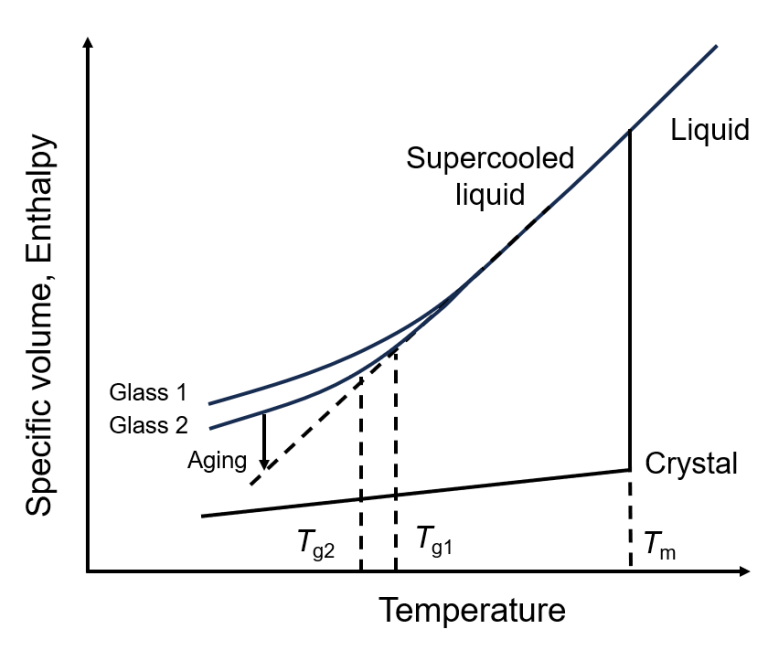


Figure 1. Schematic of specific volume or enthalpy of a liquid as a function of temperature. The glassy state depends on the cooling rate. During aging, a glass evolves towards the equilibrium liquid.

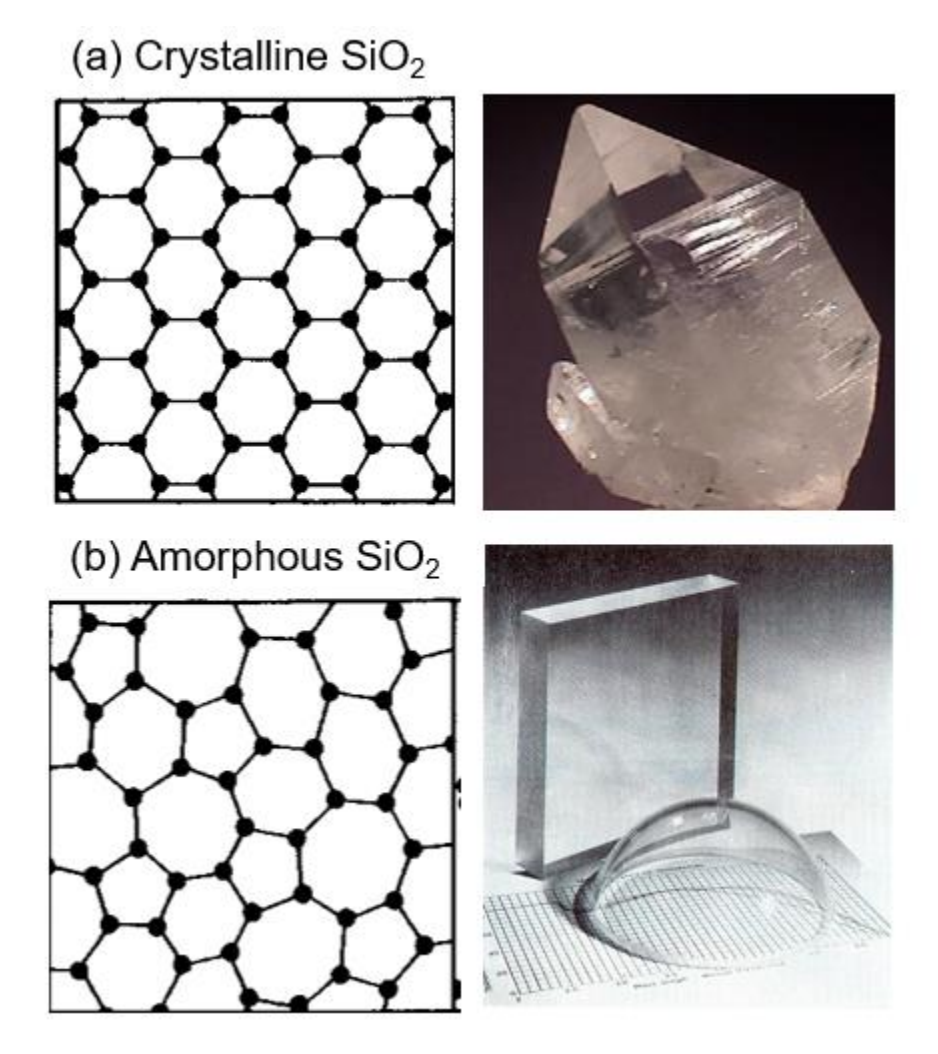


Figure 2. Comparison between (a) crystalline SiO₂ and (b) amorphous SiO₂. Crystals have both short- and long-range order while glasses only have shot-range order.

1.2 Surface segregation

For a single-phase, multi-component liquid, the surface composition can differ significantly from the bulk. For example, Figure 3 shows the surface enrichment of surfactants at an air/water interrace. Surfactant molecules are amphiphilic and exhibit a preferred orientation with the hydrophobic tails up to minimize surface energy. ^{14,15} This phenomenon, referred to as surface segregation, also occurs in polymer solution. ^{16,17} Polystyrene, for example, absorbs to the

surface of dimethyl sulfoxide, ¹⁸ and is depleted at the surface of toluene. ¹⁹ Surface segregation occurs as it is thermodynamically favorable to populate a surface with components that have lower surface energy. ^{16, 20}

Interface phenomena have a strong influence on materials properties, including physical stability,²¹ wetting,²² powder flow,²³ and tabletability.²⁴ In the case of dairy products, the surface of whole milk powder can be significantly enriched with fat due to the lower surface energy.^{25,26} The surface enrichment of fat reduces the wetting of milk powder, and makes it readily susceptible to oxidation and subsequent rancidity.²⁷

The surface segregation phenomenon remains poorly understood for amorphous drug formulations.²⁸ The need for a deeper understanding is highlighted by the recent findings that molecules can be extremely mobile at the surface of amorphous drugs.²¹ This high surface mobility leads to fast surface crystallization, and failure of the amorphous formulation.²⁹ The surface enrichment of highly mobile ingredients, such as surfactants, is likely to increase local mobility and accelerate crystallization, in addition to altering the wetting and dissolution characteristics. Meanwhile, the kinetics of surface segregation remains unknown, which can impact the change in formulation performance during storage.

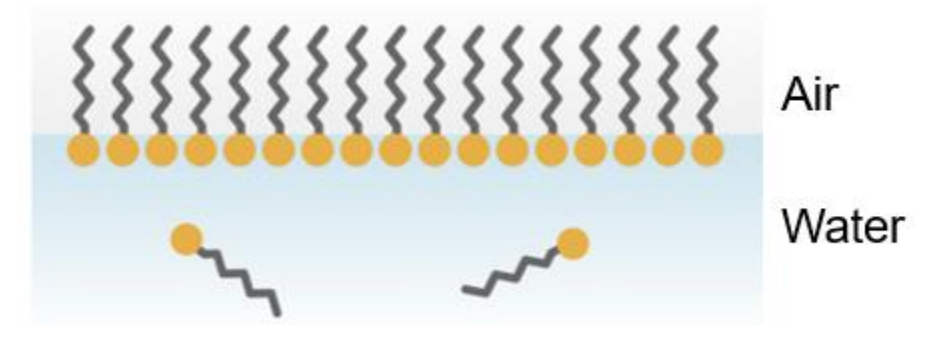


Figure 3. Surfactant enrichment at the air/water interface. Surfactants are oriented at the interface with hydrophobic tails up to minimize surface energy.

1.3 Determination of surface composition by X-ray photoelectron spectroscopy

Surface compositions can be quantitively determined by X-ray photoelectron spectroscopy (XPS). 30,31 XPS relies on Einstein's photoelectric effect. An atom, when irradiated by high energy X-ray, can emit photoelectrons. The binding energy of the photoelectron can be calculated by $E_{\text{binding}} = hv - E_{\text{kinetic}}$, where hv is the energy of the X-ray and E_{kinetic} is the measured kinetic energy of the photoelectron. The binding energy is specific for an atom, its electronic orbital, and its state of ionization and protonation. Photoelectrons cannot travel long distances (several nanometers in an organic solid), which makes XPS a surface-analytical technique. 32,33,34

1.4 Anisotropic glasses

The structure of a glass is usually considered isotropic, a result of its isotropic liquid precursor.^{35,36} Recent works have highlighted the importance of anisotropic glasses, which can be viewed as the hybrid materials between crystals and traditional glasses. These glasses exhibit highly ordered and anisotropic structures, with order parameters bordering on values for crystals, and their structural order can be different and tunable, depending on the process conditions.

Anisotropic glasses can be obtained by physical vapor deposition (PVD)² and spin-coating.³⁷ In the case of PVD, the material is condensed from a vapor onto a substrate.^{38,39} During deposition, the surface molecules are highly mobile, and can adopt the preferred orientation and layering at the interface before being incorporated into the bulk glass by later-depositing molecules.⁴⁰ The molecular orientation in the glass can be controlled by varying the substrate temperature or deposition rate,⁴¹ which enables the fine-tuning of properties such as density, structural order, and stability.

Another method of preparing anisotropic glasses is to vitrify a precursor liquid that has structural order such as a liquid crystal (LC). LCs possess liquid-like fluidity and crystal-like order in some dimensions. LCs are useful materials for displays and sensors as they can be rapidly organized in terms of molecular orientations and positions by temperature or external fields. ⁴² As Figure 5a shows, upon cooling, a thermotropic LC of rod-like molecules transforms from the isotropic liquid to a nematic and/or a smectic liquid. In the nematic phase, the rod axis tends towards the LC director but the molecular centers of mass are disordered; in the smectic phase, the molecules are further organized into layers. ⁴³ Similarly, for a discotic LC in Figure 5b, the disc-like molecules transform from the isotropic liquid to a columnar liquid where molecules are assembled into columns. ^{44,45} When further cooled, some LC systems undergo a glass transition, and the LC order is frozen into the glass. ^{46,47}

Recent works have shown that a LC transition can be avoided partially or completely at moderate cooling rates, and the LC order trapped in glasses can be different and tunable. 48,49,50

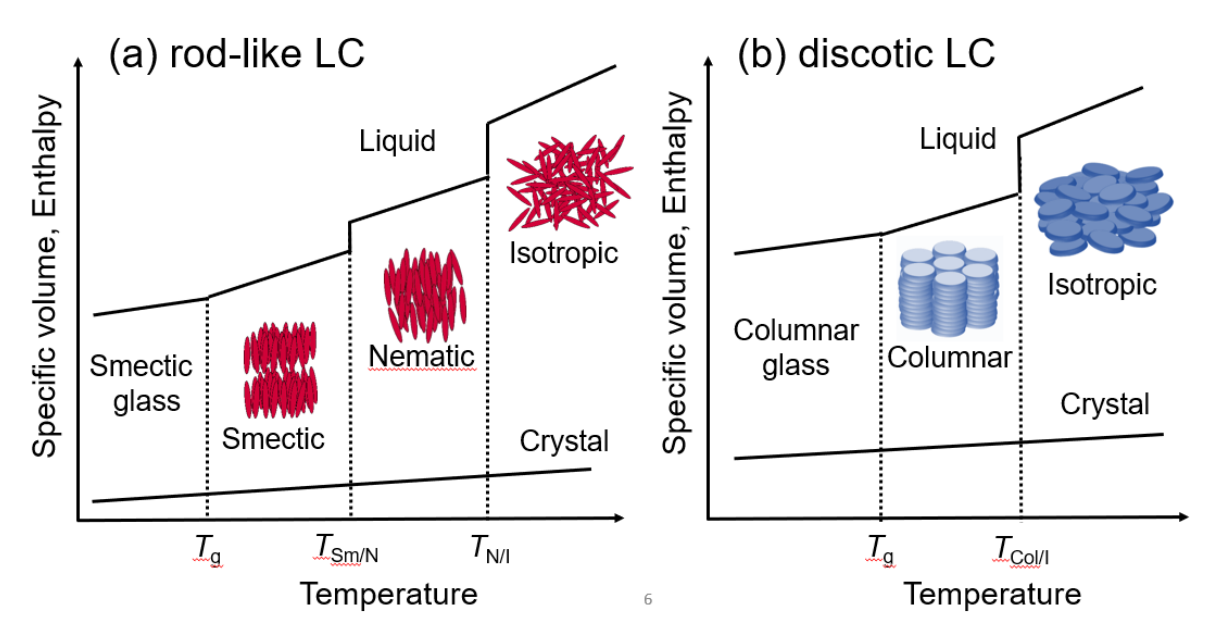


Figure 5. Phase transitions upon cooling a LC composed of (a) rod-like and (b) discotic mesogens

For the rod-like LC molecules, the smectic order trapped in glasses is controlled by the kinetic arrest of the end-over-end rotation. Similarly, for the discotic LC molecules, the control of columnar order is associated with the kinetic arrest of the disc-tumbling. This ability is relevant for the optimization of the physical state of amorphous materials to improve their performance.

1.5 Contributions of this thesis

This dissertation focuses on two areas of amorphous materials: surface enrichment of components in amorphous formulations and control of liquid crystalline order. In the context of surface enrichment, this dissertation extends the previous observation of surface segregation in alloys and polymer solution to amorphous pharmaceutical materials. This study developed a quantitative and accurate XPS method for determining surface composition of amorphous materials. Furthermore, it reports the first example of strong surface enrichment of surfactants in amorphous drug formulations, and a predictive tool for the kinetics of surface enrichment of polymers. For the control of liquid-crystalline order, a notable breakthrough is that we observed two groups of freezing temperatures in a single-component glass, corresponding to the kinetic arrests of two relaxation modes. We find that the same principle applies to both rod-like and discotic mesogens, allowing for a broad application in glass engineering.

In Chapter 2, we find that the surface of amorphous drugs can be significantly enriched with surfactants. The surface coverage can reach up to 100%, without phase separation in the bulk. In all the systems investigated, we observed significant surface enrichment of surfactants. For acetaminophen containing different surfactants (Span 20, Span 80, Tween 20, Tween 80), the strongest surface enrichment occurred for the most lipophilic Span 80, resulting in nearly complete surface coverage. For the same surfactant Span 80 doped in different drugs, the surface

enrichment of surfactants increases with the hydrophilicity of the drug matrix (decreasing log P). These effects arise because surfactants possess lower surface energy and tend to enrich the interface. This study highlights the potentially large difference between the surface and bulk compositions of an amorphous formulation, which is expected to have a substantial impact on the stability, wetting, and dissolution.

Chapter 3 further investigated the kinetics of surface enrichment of polymers. The bulk-miscible system of maltitol containing polyvinylpyrrolidone (PVP) was studied as a model. The surface PVP concentration is significantly higher than the bulk, by up to a factor of 170, and the effect increases with the molecular weight of PVP. At a freshly created surface, we observed the evolution of surface PVP concentration, and the rate is controlled by the bulk diffusion of the polymer. The polymer diffusion coefficient obtained from the kinetics of surface enrichment is consistent with that calculated from the Stokes–Einstein equation. Our finding provides a method of measuring the kinetics of surface enrichment in an amorphous material, and allows prediction of the equilibrium time of surface composition.

Chapter 4 discovers multiple kinetics arrests in a liquid-crystalline glass, itraconazole (ITZ). We applied X-ray scattering to characterize different ITZ glasses prepared by different cooling rates. We find that each glass is characterized by not one, but two fictive temperatures T_f (the temperature at which a chosen order parameter is frozen in the equilibrium liquid). The higher T_f is associated with the regularity of smectic layers and lateral packing, while the lower T_f with the molecular spacings between and within smectic layers. The two freezing temperatures can further be associated with the two relaxation modes observed by dielectric spectroscopy: the slower δ mode (end-over-end rotation) is associated with the freezing of the regularity of molecular packing and the faster α mode (rotation about the long axis) with the freezing of the

spacing between molecules. Our finding suggests a way to selectively control the structural features of glasses. Application of this principle could lead to glasses with tailor-made properties for applications in organic electronics and pharmaceutics.

Chapter 5 further extends the observation of multiple kinetic arrests to a glass-forming discotic liquid crystal, Phenanthro[1,2,3,4,ghi]perylene-1,6,7,12,13,16-hexacarboxylic hexaester (PNP). X-ray scattering has been used to characterize the columnar packing and the π stacking. In the equilibrium liquid state, we observed concurrent development of π stacking and columnar packing, as indicated by the proportional relationship between the scattering intensities of the two structural orders. Upon cooling into the glassy state, the π - π distance shows a kinetic arrest with a change in the thermal expansion coefficient (TEC) from 321 to 109 ppm/K, while the intercolumnar spacing exhibits a constant TEC of 113 ppm/K. Furthermore, we show that it is possible to prepare glasses with a wide range of columnar and π stacking orders, including zero order, by different cooling rates. For each glass, the columnar order and the π stacking order correspond to a much hotter liquid than its enthalpy and π - π distance, with the difference between the two fictive temperatures exceeding 100 K. By comparison with the relaxation map obtained by dielectric spectroscopy, we find that the δ mode (disk tumbling within a column) controls the columnar order and the π stacking order trapped in the glass, while the α mode (disk spinning about its axis) controls the enthalpy and the π - π spacing. Our finding is relevant for controlling the different structural features of a molecular glass to optimize its properties.

Chapter 6 suggests directions for future work that could benefit from the above discoveries. Following the study of surface enrichment of surfactants, we propose to further study its impact on surface crystallization and wetting. Given that surfactants are highly mobile, and the hydrophobic tails point up to the air, the surface enrichment of surfactants is expected to

promote surface crystallization, resulting in poor physical stability. We propose to use atomic force microscopy (AFM) to characterize the surface topography of surfactant enrichment. This study is expected to answer whether surfactants are uniformly distributed on the surface, or if there exist segregated domains. In the context of control of liquid-crystalline order in glasses, we propose to study the evolution of liquid-crystalline order during glass aging. This study will investigate how the two groups of fictive temperatures evolve towards equilibrium and whether the pathway can be described using classical models typically applied to normal glasses.

1.6 References

(1) Zallen, R. The physics of amorphous solids; John Wiley & Sons, 2008.

- (3) Law, D.; Schmitt, E. A.; Marsh, K. C.; Everitt, E. A.; Wang, W.; Fort, J. J.; Krill, S. L.; Qiu, Y. Ritonavir–PEG 8000 amorphous solid dispersions: in vitro and in vivo evaluations. *Journal of pharmaceutical sciences* 2004, *93* (3), 563-570.
- (4) Newman, A.; Knipp, G.; Zografi, G. Assessing the performance of amorphous solid dispersions. *Journal of pharmaceutical sciences* 2012, *101* (4), 1355-1377.
- (5) Bhujbal, S. V.; Mitra, B.; Jain, U.; Gong, Y.; Agrawal, A.; Karki, S.; Taylor, L. S.; Kumar, S.; Zhou, Q. T. Pharmaceutical amorphous solid dispersion: A review of manufacturing strategies. *Acta Pharmaceutica Sinica B* 2021, *11* (8), 2505-2536. Yu, L. Amorphous pharmaceutical solids: preparation, characterization and stabilization. *Advanced drug delivery reviews* 2001, *48* (1), 27-42.

⁽²⁾ Ediger, M. D.; de Pablo, J.; Yu, L. Anisotropic vapor-deposited glasses: hybrid organic solids. *Accounts of chemical research* 2019, 52 (2), 407-414.

- (6) Ediger, M. D.; Angell, C. A.; Nagel, S. R. Supercooled liquids and glasses. *The journal of physical chemistry* 1996, *100* (31), 13200-13212.
- (7) Angell, C. A. Formation of glasses from liquids and biopolymers. *Science* 1995, 267 (5206), 1924-1935.
- (8) Moynihan, C. T.; Easteal, A. J.; De Bolt, M. A.; Tucker, J. Dependence of the fictive temperature of glass on cooling rate. *Journal of the American Ceramic Society* 1976, *59* (1-2), 12-16.
- (9) Simon, S.; Sobieski, J.; Plazek, D. Volume and enthalpy recovery of polystyrene. *Polymer* 2001, 42 (6), 2555-2567.
- (10) Angell, C. A.; Ngai, K. L.; McKenna, G. B.; McMillan, P. F.; Martin, S. W. Relaxation in glassforming liquids and amorphous solids. *Journal of applied physics* 2000, 88 (6), 3113-3157.
- (11) Swallen, S. F.; Bonvallet, P. A.; McMahon, R. J.; Ediger, M. Self-diffusion of trisnaphthylbenzene near the glass transition temperature. *Physical review letters* 2003, *90* (1), 015901.
- (12) Swallen, S. F.; Ediger, M. Self-diffusion of the amorphous pharmaceutical indomethacin near T g. *Soft Matter* 2011, 7 (21), 10339-10344.
- (13) Wright, A. C. Neutron scattering from vitreous silica. V. The structure of vitreous silica: What have we learned from 60 years of diffraction studies? *Journal of non-crystalline solids* 1994, *179*, 84-115.
- (14) Kronberg, B.; Holmberg, K.; Lindman, B. *Surface chemistry of surfactants and polymers*; John Wiley & Sons, 2014.

- (15) Rasing, T.; Shen, Y.; Kim, M. W.; Valint Jr, P.; Bock, J. Orientation of surfactant molecules at a liquid-air interface measured by optical second-harmonic generation. *Physical Review A* 1985, *31* (1), 537.
- (16) Siow, K.; Patterson, D. Surface thermodynamics of polymer solutions. *The Journal of Physical Chemistry* 1973, 77 (3), 356-365.
- (17) De Gennes, P. d. Polymer solutions near an interface. Adsorption and depletion layers. *Macromolecules* 1981, *14* (6), 1637-1644.
- (18) Bloch, J.; Sansone, M.; Rondelez, F.; Peiffer, D.; Pincus, P.; Kim, M.-W.; Eisenberger, P. Concentration profile of a dissolved polymer near the air-liquid interface: X-ray fluorescence study. *Physical review letters* 1985, *54* (10), 1039.
- (19) Lee, L.; Guiselin, O.; Lapp, A.; Farnoux, B.; Penfold, J. Direct measurements of polymer depletion layers by neutron reflectivity. *Physical review letters* 1991, 67 (20), 2838.
- (20) Prigogine, I.; Marechal, J. The influence of differences in molecular size on the surface tension of solutions. IV. *Journal of colloid science* 1952, 7 (2), 122-127.
- (21) Yu, L. Surface mobility of molecular glasses and its importance in physical stability. *Advanced drug delivery reviews* 2016, *100*, 3-9.
- (22) Li, Y.; Yu, J.; Hu, S.; Chen, Z.; Sacchetti, M.; Sun, C. C.; Yu, L. Polymer nanocoating of amorphous drugs for improving stability, dissolution, powder flow, and tabletability: The case of chitosan-coated indomethacin. *Molecular pharmaceutics* 2019, *16* (3), 1305-1311.
- (23) Jange, C. G.; Ambrose, R. K. Effect of surface compositional difference on powder flow properties. *Powder Technology* 2019, *344*, 363-372.
- (24) Shi, L.; Sun, C. C. Overcoming poor tabletability of pharmaceutical crystals by surface modification. *Pharmaceutical research* 2011, 28, 3248-3255.

- (25) Vignolles, M.-L.; Jeantet, R.; Lopez, C.; Schuck, P. Free fat, surface fat and dairy powders: interactions between process and product. A review. *Le Lait* 2007, 87 (3), 187-236.
- (26) Kim, E. H.-J.; Chen, X. D.; Pearce, D. Surface composition of industrial spray-dried milk powders. 1. Development of surface composition during manufacture. *Journal of Food Engineering* 2009, *94* (2), 163-168.
- (27) Nijdam, J.; Langrish, T. The effect of surface composition on the functional properties of milk powders. *Journal of Food Engineering* 2006, 77 (4), 919-925.
- (28) Chen, Z.; Yang, K.; Huang, C.; Zhu, A.; Yu, L.; Qian, F. Surface enrichment and depletion of the active ingredient in spray dried amorphous solid dispersions. *Pharmaceutical Research* 2018, *35* (2), 38.
- (29) Wu, T.; Yu, L. Surface crystallization of indomethacin below T g. *Pharmaceutical research* 2006, *23* (10), 2350-2355.
- (30) Chastain, J.; King Jr, R. C. Handbook of X-ray photoelectron spectroscopy. *Perkin-Elmer*, *USA* 1992, 261.
- (31) Seah, M. The quantitative analysis of surfaces by XPS: A review. *Surface and Interface Analysis* 1980, 2 (6), 222-239.
- (32) Seah, M. P.; Dench, W. Quantitative electron spectroscopy of surfaces: A standard data base for electron inelastic mean free paths in solids. *Surface and interface analysis* 1979, *I* (1), 2-11.
- (33) Roberts, R.; Allara, D.; Pryde, C.; Buchanan, D.; Hobbins, N. Mean free path for inelastic scattering of 1.2 kev electrons in thin poly (methylmethacrylate) films. *Surface and Interface Analysis* 1980, 2 (1), 5-10.

- (34) Wagner, C.; Davis, L.; Zeller, M.; Taylor, J.; Raymond, R.; Gale, L. Empirical atomic sensitivity factors for quantitative analysis by electron spectroscopy for chemical analysis. *Surface and interface analysis* 1981, *3* (5), 211-225.
- (35) Warren, B. X-ray determination of the structure of liquids and glass. *Journal of Applied Physics* 1937, 8 (10), 645-654.
- (36) Benmore, C. J. X-Ray Diffraction from Glass. Modern Glass Characterization 2015, 1-30.
- (37) Nardes, A. M.; Kemerink, M.; Janssen, R. A.; Bastiaansen, J. A.; Kiggen, N. M.; Langeveld,
- B. M.; Van Breemen, A. J.; De Kok, M. M. Microscopic understanding of the anisotropic conductivity of PEDOT: PSS thin films. *Advanced Materials* 2007, *19* (9), 1196-1200.
- (38) Gómez, J.; Jiang, J.; Gujral, A.; Huang, C.; Yu, L.; Ediger, M. Vapor deposition of a smectic liquid crystal: highly anisotropic, homogeneous glasses with tunable molecular orientation. *Soft Matter* 2016, *12* (11), 2942-2947.
- (39) Gujral, A.; Gómez, J.; Jiang, J.; Huang, C.; O'Hara, K. A.; Toney, M. F.; Chabinyc, M. L.; Yu, L.; Ediger, M. Highly organized smectic-like packing in vapor-deposited glasses of a liquid crystal. *Chemistry of Materials* 2017, 29 (2), 849-858.
- (40) Bishop, C.; Thelen, J. L.; Gann, E.; Toney, M. F.; Yu, L.; DeLongchamp, D. M.; Ediger, M. D. Vapor deposition of a nonmesogen prepares highly structured organic glasses. *Proceedings of the National Academy of Sciences* 2019, *116* (43), 21421-21426.
- (41) Bishop, C.; Bagchi, K.; Toney, M. F.; Ediger, M. Vapor deposition rate modifies anisotropic glassy structure of an anthracene-based organic semiconductor. *The Journal of Chemical Physics* 2022, *156* (1), 014504.
- (42) Collings, P. J.; Goodby, J. W. *Introduction to liquid crystals: chemistry and physics*; Crc Press, 2019.

- (43) Seddon, J. M. Structural studies of liquid crystals by X-ray diffraction. *Handbook of liquid crystals* 1998, *1*, 635-679.
- (44) Prasad, S. K.; Rao, D. S.; Chandrasekhar, S.; Kumar, S. X-Ray studies on the columnar structures of discotic liquid crystals. *Molecular Crystals and Liquid Crystals* 2003, *396* (1), 121-139.
- (45) Kaafarani, B. R. Discotic liquid crystals for opto-electronic applications. *Chemistry of Materials* 2011, 23 (3), 378-396.
- (46) Tsuji, K.; Sorai, M.; Seki, S. New finding of glassy liquid crystal—A non-equilibrium state of cholesteryl hydrogen phthalate. *Bulletin of the Chemical Society of Japan* 1971, *44* (5), 1452-1452.
- (47) Wedler, W.; Demus, D.; Zaschke, H.; Mohr, K.; Schäfer, W.; Weissflog, W. Vitrification in low-molecular-weight mesogenic compounds. *Journal of Materials Chemistry* 1991, *1* (3), 347-356.
- (48) Teerakapibal, R.; Huang, C.; Gujral, A.; Ediger, M. D.; Yu, L. Organic glasses with tunable liquid-crystalline order. *Physical review letters* 2018, *120* (5), 055502.
- (49) Chen, Z.; Yu, J.; Teerakapibal, R.; Meerpoel, L.; Richert, R.; Yu, L. Organic glasses with tunable liquid-crystalline order through kinetic arrest of end-over-end rotation: the case of saperconazole. *Soft Matter* 2020, *16* (8), 2025-2030.
- (50) Chen, Z.; Bishop, C.; Thoms, E.; Bock, H.; Ediger, M. D.; Richert, R.; Yu, L. Controlling the Columnar Order in a Discotic Liquid Crystal by Kinetic Arrest of Disc Tumbling. *Chemistry of Materials* 2021, *33* (12), 4757-4764.

Chapter 2

Surface Enrichment of Surfactants in Amorphous Drugs: An X-Ray Photoelectron Spectroscopy Study

Junguang Yu, Yuhui Li, Xin Yao, Chailu Que, Lian Huang, Ho-Wah Hui, Yuchuan Gong, Feng Qian, Lian Yu

As published in

Molecular pharmaceutics, 2022, 19(2): 654-660.

DOI: 10.1021/acs.molpharmaceut.1c00786

2.1 Abstract

Surfactants are commonly incorporated into amorphous formulations to improve the wetting and dissolution of hydrophobic drugs. Using X-ray photoelectron spectroscopy (XPS), we find that a surfactant can significantly enrich at the surface of an amorphous drug, up to 100 % coverage, while maintaining bulk miscibility. We compared four different surfactants (Span 80, Span 20, Tween 80, and Tween 20) in the same host acetaminophen and the same surfactant Span 80 in four different hosts (acetaminophen, lumefantrine, posaconazole, and itraconazole). For each system, the bulk concentrations of the surfactants were 0, 1, 2, 5, and 10 wt %, which cover the typical concentrations in amorphous formulations, and component miscibility in the bulk was confirmed by DSC. For all systems investigated, we observed significant surface enrichment of the surfactants. For acetaminophen containing different surfactants, strongest surface enrichment occurred for the most lipophilic Span 80 (lowest HLB), with nearly full surface coverage. For the same surfactant Span 80 doped in different drugs, the surface enrichment effect increases with the hydrophilicity of the drug (decreasing log P). These effects arise because low-surface-energy molecules (or molecular fragments) tend to enrich at a liquid/vapor interface. This study highlights the potentially large difference between the surface and bulk compositions of an amorphous formulation. Given their high mobility and low glass transition temperature, the surface enrichment of surfactants in an amorphous drug can impact its stability, wetting, and dissolution.

2.2 Introduction

Amorphous Solid Dispersion (ASD) is a widely used technology to enhance the solubility and bioavailability of poorly soluble drugs. A typical ASD contains a drug, a polymer and a

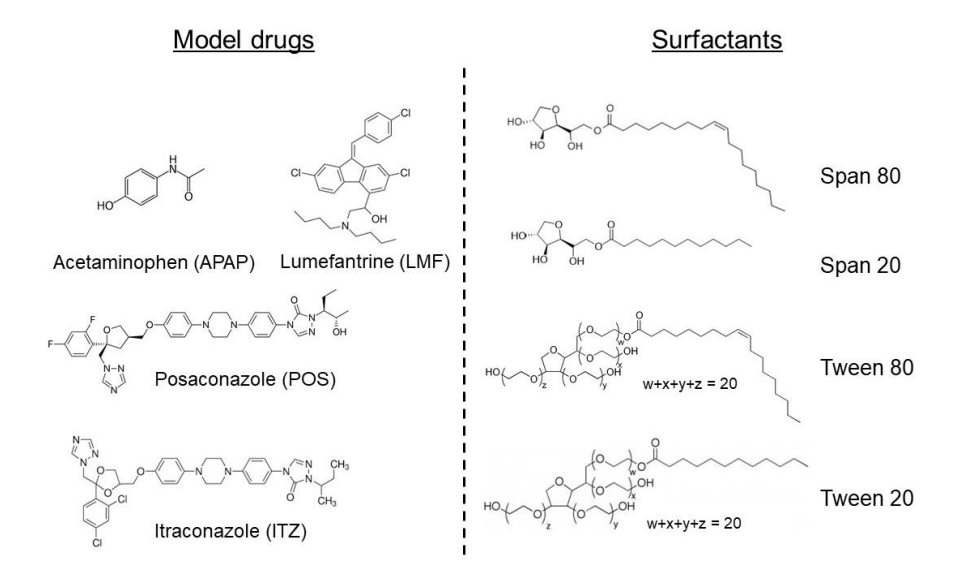
surfactant. With a typical concentration of 5–10 wt %, the surfactant facilitates the wetting and dissolution of the usually hydrophobic drug² and serves as a plasticizer to lower the processing temperature of hot melt extrusion (HME).³

A surfactant is known to enrich at the surface of an aqueous solution. In this process, the surfactant's hydrophobic tail is excluded from water and its hydrophilic head remains in contact with the aqueous medium, thus lowering the surface energy of the system.⁴ Although the surface enrichment effect has been extensively studied for surfactants in aqueous solutions, the phenomenon is less well understood for surfactants in hydrophobic solvents where the solvent also has low surface energy and thus competes with the surfactant for surface enrichment.^{5, 6} To our knowledge, the surface enrichment effect has never been studied for surfactants in ASDs.

The need to understand whether a surfactant is enriched at the surface of an ASD is highlighted by the recent finding⁷ that molecules can be extremely mobile at the surface of amorphous drugs. This high surface mobility in turn leads to fast surface crystallization^{8,9} and failure of the amorphous formulation. Given that common pharmaceutical surfactants have high mobility and low glass transition temperature T_g , ¹⁰ their enrichment at the surface of ASDs would increase local mobility and accelerate crystallization. The surface enrichment of surfactants is also expected to alter the wetting and dissolution characteristics of the ASD.

In this study we utilized X-ray photoelectron spectroscopy (XPS)¹¹⁻¹³ to investigate the surface enrichment effects of surfactants in amorphous drugs. Scheme 1 and Table 1 show the drugs and surfactants used in this study. Four common pharmaceutical surfactants (Span 80, Span 20, Tween 80, and Tween 20) were studied. These surfactants have systematically changing structures. For example, Span 80 and Tween 80 have the same hydrophobic tail but Tween 80 has a larger hydrophilic head group; Span 80 and Span 20 have the same hydrophilic head but Span

80 has a longer hydrophobic tail. We compare the four surfactants in the same host acetaminophen (APAP), as well as the same surfactant Span 80 in four different drug hosts (acetaminophen, lumefantrine, posaconazole, and itraconazole). The surfactant concentrations used (0–10 wt %) cover the typical concentrations in ASDs, and component miscibility in the bulk was confirmed by DSC. For all systems investigated, we observed significant surface enrichment of the surfactants. For different surfactants doped in acetaminophen, strongest surface enrichment occurred for the most lipophilic Span 80 (lowest HLB), with its surface concentration approaching 100 %. For the same surfactant Span 80 doped in different drugs, the surface enrichment effect increases with the hydrophilicity of the drug (decreasing $\log P$). These effects are explained by the tendency for component segregation at the liquid/vapor interface to minimize surface energy. Our results highlight the potentially large difference between the surface composition and the bulk composition of an ASD. Given their high mobility and low $T_{\rm g}$, the surface enrichment of surfactants can potentially accelerate surface crystallization and alter the wetting and dissolution of amorphous particles.



Scheme 1. Model drugs and surfactants used in this study.

Table 1. Physical properties of the drugs and surfactants used in this study

Compound	Formula	T _g onset (K)	$\log P$
Acetaminophen (APAP, pain medicine)	C ₈ H ₉ NO ₂	294	0.46^{14}
Lumefantrine (LMF, antimalarial)	$C_{30}H_{32}Cl_3NO$	292	$2.9^{15, 16}$
Posaconazole (POS, antifungal)	$C_{37}H_{42}F_2N_8O_4$	332	4.77^{17}
Itraconazole (ITZ, antifungal)	$C_{35}H_{38}Cl_{2}N_{8}O_{4}$	330	5.66^{18}

Surfactant	Formula	HLB	a
Span 80	C ₂₄ H ₄₄ O ₆	4.3	Most lipophilic
Span 20	$C_{18}H_{34}O_{6}$	8.6	
Tween 80	$C_{64}H_{124}O_{26}$	15	
Tween 20	$C_{58}H_{114}O_{26}$	16.7	Most hydrophilic

^aHLB: Hydrophilic-Lipophilic Balance. The values are from Ref. 19.

2.3 Experimental Section

Materials. Acetaminophen (APAP, 99.0 %) was purchased from Sigma-Aldrich (St. Louis, MO). Itraconazole (ITZ, 98 %) was purchased from Alfa Aesar (Ward Hill, MA). Posaconazole (POS) was a gift from Merck (Kenilworth, NJ). These three drugs were used as received. Lumefantrine (LMF, 97 %) was purchased from Nanjing Bilatchem Industrial Co. (Nanjing, China) and used after re-crystallization from CH₂Cl₂ solution. Surfactants Span 20, Span 80, Tween 20 and Tween 80 were obtained from Sigma-Aldrich (St. Louis, MO) and used as received.

Sample preparation. 200 mg total of a drug containing 10 wt % or 20 wt % surfactant was mixed by grinding with 0.4 mL ethanol in a mortar. Dilution of the 10 wt % mixture yielded the 1 wt % mixture; dilution of the 20 wt % mixture yielded the 2 wt % and 5 wt % mixtures.

About 5 mg of each mixture prepared above was melted approximately 20 K above its melting point on a coverslip for several minutes to a transparent droplet and quenched to room temperature by contact with an aluminum block. The samples were stored in a capped plastic tube filled with Drierite before XPS analysis. After measurements, the samples remained amorphous and transparent without crystallization.

Differential scanning calorimetry (DSC). The glass transition of each mixture was measured by a TA Q2000 differential scanning calorimeter. Each sample of 4–7 mg was placed in a crimped aluminum pan. The glass transition temperature $T_{\rm g}$ was measured during heating at 10 K/min after vitrifying a melt by cooling at 10 K/min. All measurements were performed under 50 mL/min N_2 purge.

X-ray photoelectron spectroscopy (XPS). XPS spectra were measured using a Thermo Scientific K-Alpha X-ray Photoelectron Spectrometer with a monochromic Al Kα (1486.6 eV) source. Samples were loaded into a vacuum chamber (~10⁻⁵ Pa) and measured at room temperature (297 K). An electron flood gun was used to neutralize the surface charge for the nonconductive materials of this work. The spot size of measurement was 400 μm. A survey scan for all the possible elements was performed at step size of 1 eV and passing energy of 200 eV. High-resolution scans for elements of interest were performed at step size of 0.1 eV step and passing energy of 50 eV. For quantitative measurement of atomic ratios, high-resolution scans were used. XPS spectra were analyzed using the Avantage Data System. Calibration of binding energy was

made by shifting the observed carbon peak (C 1s) to 285.0 eV.²⁰ The baseline for integration was obtained from a smart baseline function in Avantage.

2.4 Results and Discussion

XPS method validation. When a solid is irradiated by an X-ray, surface atoms can emit photoelectrons.²¹ From the energies of the X-ray and the emitted electrons, the binding energy can be calculated for the atoms from which photoelectrons originate. An XPS spectrum is a plot of the photoelectron count against binding energy where each peak corresponds to a specific atom and electronic orbital.²² Using the Relative Sensitivity Factors (RSF), the photoelectron counts can be converted to the atomic fractions.²³ Because electrons travel only a short distance through solids, XPS is surface sensitive. The XPS intensity as a function of penetration depth, x, is given by $I = I_0 \exp(-x/\lambda)$, where the decay length λ is approximately 3 nm for photoelectrons originating from nitrogen (N 1s) and oxygen (O 1s) in organic compounds.^{24, 25} In practice, only photoelectrons from a surface layer less than $3\lambda \approx 9$ nm thick are detected.

Our first task was to validate the XPS method for measuring the surface concentrations of amorphous drugs. For this purpose, we investigated 10 *pure* compounds for which no surface enrichment or depletion occurs. These compounds are collected in Table 2. Each compound was measured in the form of an amorphous film prepared by melt-quenching; one or two spots were measured in each sample. For each compound, a specific atomic ratio is

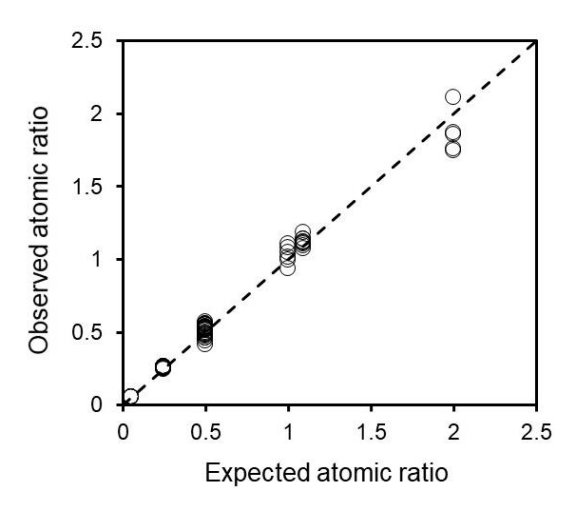


Figure 1. XPS measured atomic ratios plotted against theoretical values for pure compounds in Table 2. The dash line indicates perfect agreement.

determined by XPS and compared with the theoretical value from the molecular formula. For example, for APAP, the measured N/O ratio is 0.508 (0.035) and the theoretical ratio is 0.5. The ratio method was adopted to eliminate systematic errors; for example, it avoids the carbon peak that is prone to error from contamination. Table 2 shows that the XPS method accurately determined the atomic ratios, with a mean absolute error of 5 %. In Figure 1, the measured and theoretical atomic ratios are plotted against each other, again verifying a close agreement and absence of systematic error.

Table 2. XPS measured atomic ratios vs. expected values for pure compounds

Model drugs	Formula	Ratio	Expected	Observed	Std. dev.	% difference
Acetaminophen	C ₈ H ₉ NO ₂	N/O	0.5	0.508	0.035	1.5
Celecoxib	$C_{17}H_{14}F_3N_3O_2S$	S/O	0.5	0.525	0.014	5.0
Indomethacin	$C_{19}H_{16}CINO_4$	Cl/O	0.25	0.256	0.006	2.3
Itraconazole	$C_{35}H_{38}Cl_2N_8O_4\\$	N/O	2	1.867	0.147	-6.6
Ketoconazole	$C_{26}H_{28}Cl_2N_4O_4$	Cl/N	0.5	0.480	0.015	-3.9
Lumefantrine	$C_{30}H_{32}Cl_3NO$	N/O	1	1.033	0.075	3.3
Maltitol	$C_{12}H_{24}O_{11}$	C/O	1.09	1.118	0.031	2.5
Posaconazole	$C_{37}H_{42}F_2N_8O_4$	F/O	0.5	0.529	0.049	5.8
PVP K30 ^a	(C ₆ H ₉ NO) _n	N/O	1	1.017	0.038	1.7
TPD ^b	$C_{38}H_{32}N_2$	N/C	0.053	0.053	0.001	1.3

^aPVP K30: Polyvinylpyrrolidone K30

Different surfactants in the common host APAP. In this work, we systematically compared the surface concentrations of four surfactants (Span 20, Span 80, Tween 20, and Tween 80; see Scheme 1) in the common host APAP. To prepare for this study, we established by DSC that all four surfactants are miscible with the host in the concentration range investigated (0–10 wt %). Figure 2a shows the typical DSC results for APAP doped with Span 80. We

^bTPD: *N*,*N* '-Bis(3-methylphenyl)-*N*,*N* '-diphenylbenzidine

observe a single glass transition in each sample and a continuous shift of the glass transition temperature T_g with surfactant concentration. This indicates surfactant-host miscibility in the bulk. If the components were phase separated, two glass transitions would be observed and the two T_g s would not vary with concentration.²⁶

In Figure 2b, the $T_{\rm g}$ of each surfactant-APAP system is plotted against the surfactant concentration. The $T_{\rm g}$ of each surfactant is below the ambient temperature. Thus, a decrease of T_g is expected with increasing concentration of the surfactant¹⁰, and this is indeed observed. The decrease of T_g is observed in the entire range investigated (0-20 wt %). This range covers the concentration range used (0–10 wt %) for the surface-enrichment study, meaning component miscibility in the bulk exists for all our samples. It is intriguing that in Figure 2b, three surfactants approximately fall in one group, while Span 80 separates from the group, showing the smallest decrease of $T_{\rm g}$ at the same concentration. This could be a consequence of Span 80 being the most lipophilic surfactant of the group (lowest HLB,

see Table 1), while APAP is a hydrophilic compound.

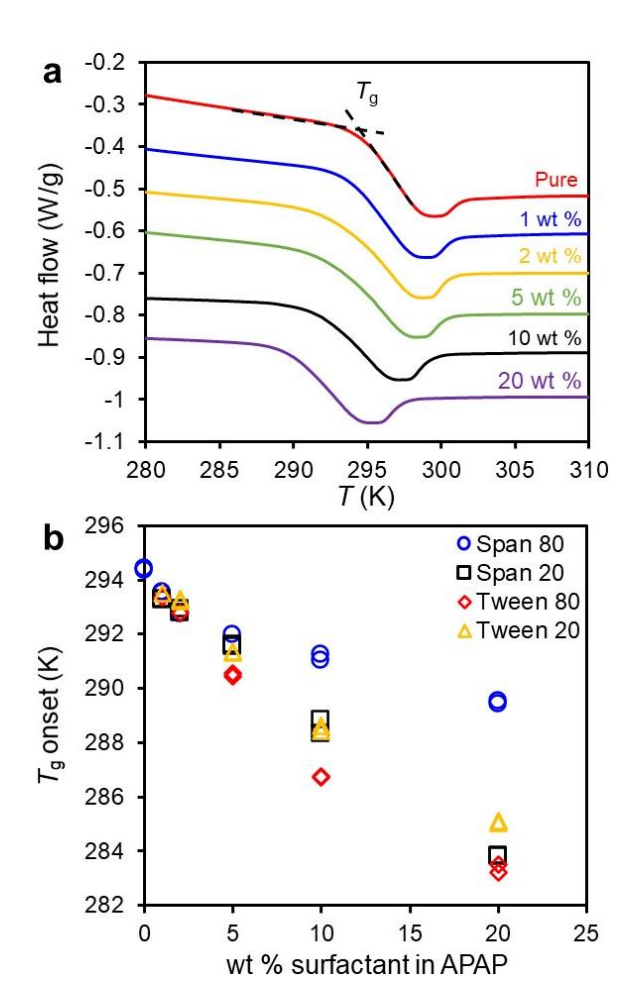


Figure 2. (a) DSC results for Span 80 doped APAP at concentrations indicated. The onset of glass transition temperature $T_{\rm g}$ is indicated. (b) $T_{\rm g}$ vs. surfactant concentration for APAP doped with Span 80, Span 20, Tween 80, and Tween 20.

Figure 3a shows the typical XPS result for measuring the surface concentration of a surfactant. In this case, the system is APAP doped with Span 80. The pure APAP spectrum has three prominent peaks for carbon (285 eV), nitrogen (400 eV) and oxygen (533 eV).²² The areas of these peaks are related to the surface atomic composition. For pure APAP, we obtain an N/O atomic ratio of $k = 0.508 \pm 0.035$, very close to the formula value of 0.5.

In the presence of surfactant
Span 80 at only 1 wt %, the nitrogen
peak diminishes and it almost vanishes
at 5 and 10 wt %. This effect is seen
more clearly in Figure 3b where only
the nitrogen peaks are shown. These
peaks have been normalized by the
oxygen peaks; that is, these spectra
directly report the N/O ratio at the
surface. As Span 80 concentration

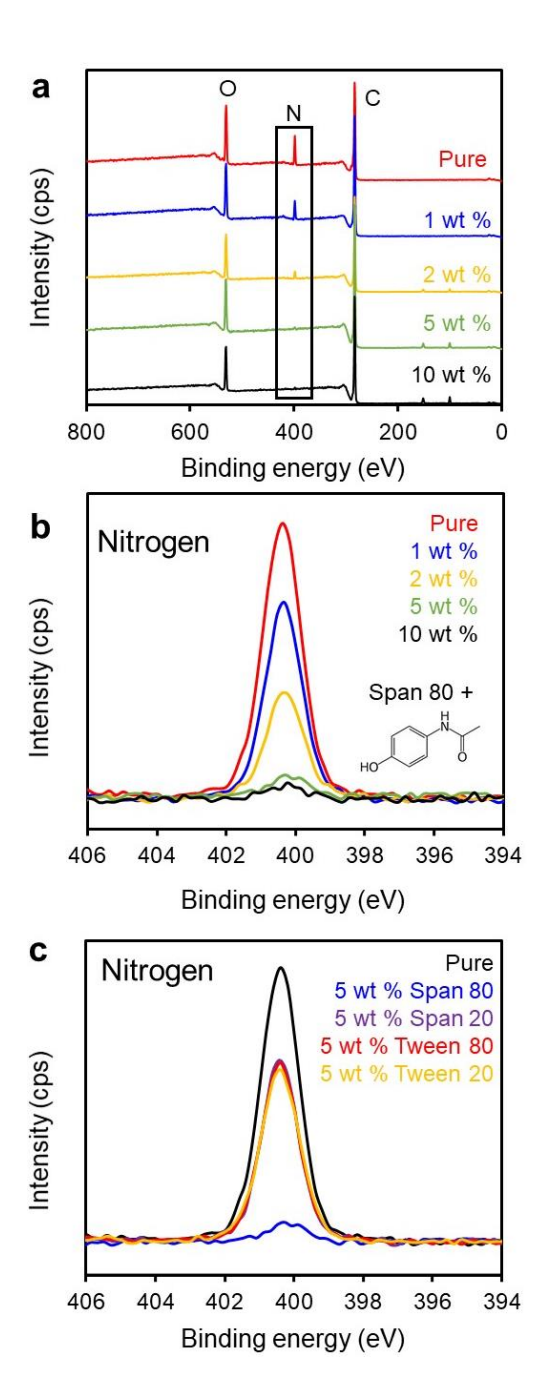


Figure 3. (a) Survey XPS spectra of pure APAP and APAP doped with Span 80 at concentrations indicated. (b) High-resolution scans of the nitrogen peak for samples in (a). (c) High-resolution scans of the nitrogen peak for APAP doped with 5 wt % of different surfactants indicated. In (b) and (c), the intensity has been normalized by the oxygen peak.

increases, the nitrogen peak decreases. Given that Span 80 has no nitrogen atoms, this result indicates that the surface is significantly covered by Span 80.

Figure 3c shows the nitrogen XPS spectra of amorphous APAP doped with 4 different surfactants: Span 80, Span 20, Tween 80 and Tween 20, all at 5 wt %. In all cases, the nitrogen peak is reduced relative to pure APAP. Since none of these surfactants has nitrogen atoms, this indicates surface enrichment for all the surfactants. We also observe a significant difference between the surfactants: the surface nitrogen peak nearly vanishes in the case of Span 80, but still robust in the other cases. This indicates that the surfactants investigated show different degrees of surface enrichment.

To quantify the surface weight-fraction concentration of a surfactant, w_s , we employ the following equation:

$$w_s = \frac{(xk-y)}{M_d} / \left[\frac{xk-y}{M_d} - \frac{zk}{M_s} \right] \tag{1}$$

where k is the observed N/O ratio (RSF already applied), x and y are respectively the numbers of oxygen and nitrogen atoms in the drug molecule (x = 2 and y = 1 for APAP), z is the number of oxygen atoms in the surfactant molecule (z = 6 for Span 80), M_d is the molecular weight of the drug, and M_s is the molecular weight of the surfactant. This equation assumes independent responses of atoms in the region probed by the X-ray.

Figure 4 shows the surface concentration of each surfactant doped in amorphous APAP as a function of its bulk concentration. The dashed line indicates the condition where surface and bulk concentrations are equal (no surface enrichment or deletion). We find that *for every surfactant tested, surface concentration is higher than bulk concentration*. The effect is the

strongest for Span 80: when the bulk concentration is only 2 wt %, the surface concentration is 50 wt % or 25 times higher; when the bulk concentration is 10 wt %, the surface is nearly pure surfactant (90 wt %). The other three surfactants show weaker but highly significant surface enrichment; for example, at 2 wt % bulk concentration, the surface concentration is 10 times higher on average, at 20 wt %. The different behaviors

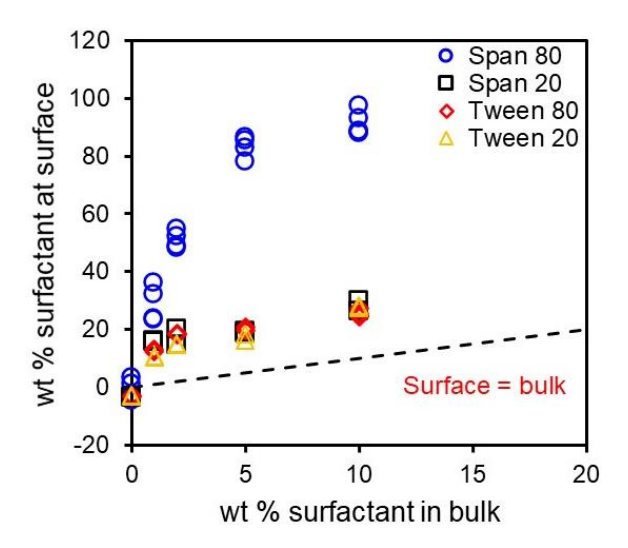


Figure 4. Surface concentration of each surfactant doped in amorphous APAP as a function of its bulk concentration.

of the surfactants are consistent with their hydrophilic-lipophilic balance (HLB, see Table 1). Higher HLB means the surfactant is more hydrophilic on balance. The most lipophilic surfactant Span 80 is expected to have the lowest affinity for the relatively hydrophilic host APAP and show the strongest surface enrichment. It is interesting that despite their different HLB values, Span 20, Tween 80, and Tween 20 have similar degrees of surface enrichment.

Same surfactant Span 80 in

different hosts. In this section, we investigate the surface enrichment behavior of the same surfactant Span 80 in several amorphous drugs. As in the case of APAP doped with different surfactants, we first assess component miscibility in the bulk. Figure 5 shows the $T_{\rm g}$ of each surfactant-drug system

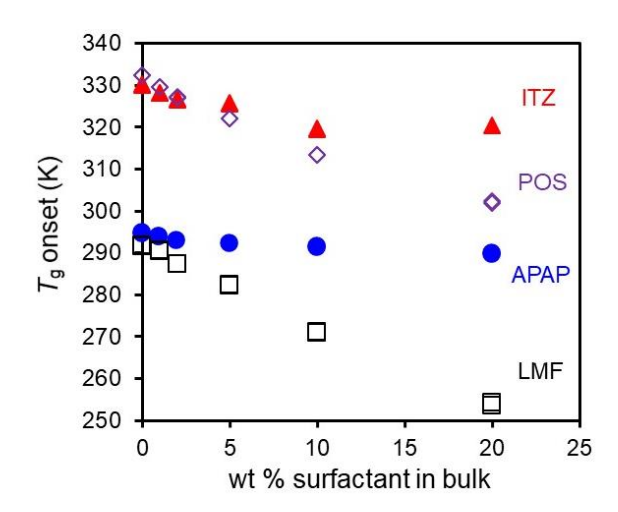


Figure 5. $T_{\rm g}$ vs. surfactant concentration for Span 80 doped in ITZ, POS, APAP and LMF.

as a function of surfactant concentration. We observe that $T_{\rm g}$ generally decreases with surfactant concentration. The concentration range investigated (0–20 wt %) exceeds that used for our surface enrichment study (0–10 wt %), indicating bulk miscibility in all our samples. For ITZ, the decrease of $T_{\rm g}$ is evident up to 10 wt %, but appears to halt between 10 and 20 wt %, suggesting potential immiscibility at higher concentrations. It is interesting that APAP shows the smallest slope of $T_{\rm g}$ decrease with Span 80 concentration. Again, this could arise from the lipophilicity of Span 80 and the hydrophilicity of APAP, leading to a weaker interaction.

Figure 6 shows XPS spectra of the amorphous drugs doped with Span 80. Since the surfactant contains only carbon and oxygen as heavy atoms, we use drug-specific atoms to quantify the change of surface composition when a surfactant is present. As indicated in Figure 6, the drug-specific atoms are: N for APAP; Cl and N for LMF; F and N for POS; Cl and N for ITZ. An inspection of Figure 6 shows that these peaks decrease in the presence of the surfactant. For example, in the presence of 10 wt % Span 80, the N and Cl peaks of LMF decrease significantly, while the O peak increases, indicating surface coverage by the surfactant. The quantitative changes are calculated using the same method

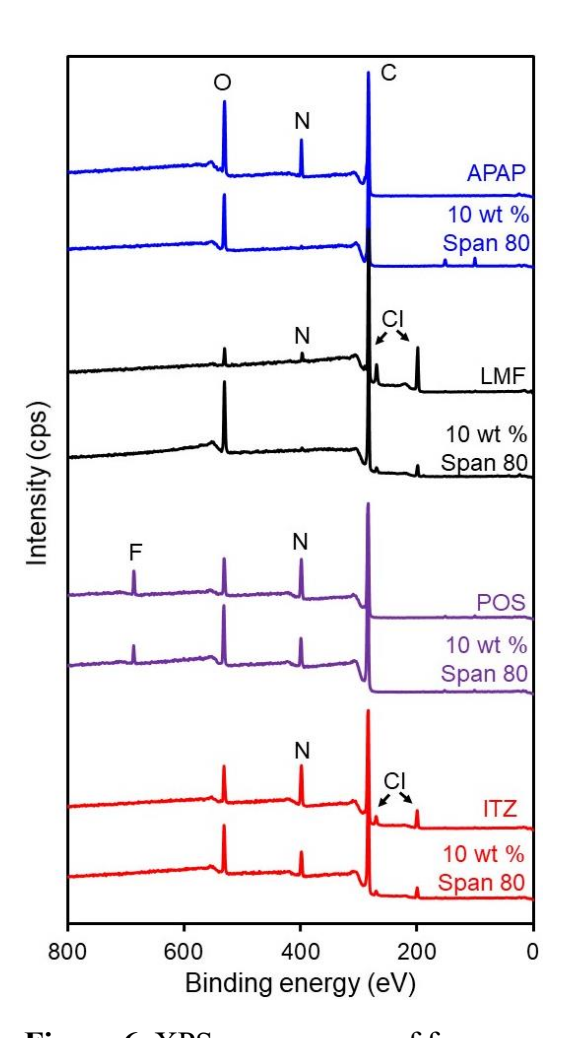


Figure 6. XPS survey scans of four amorphous drugs doped with 10 wt % Span 80. Drug-specific peaks useful for measuring surface concentrations are indicated.

described above. For this purpose, eq. 1 is modified where *k* refers to the X/O ratio, with X being a drug-specific element. When multiple choices of X/O are possible, we use the one whose measured value for the pure compound has the closest agreement with the theoretical ratio. For APAP, LMF and ITZ, N/O is used for this purpose; for POS, F/O is used.

Figure 7a shows the surface concentration of Span 80 in each amorphous drug tested as a function of its bulk concentration. The dashed line indicates the condition of no surface

enrichment or depletion. Regardless of the drug matrix tested, Span 80 shows significant surface enrichment. The effect is the strongest in APAP, followed by LMF, POS, and ITZ, though the ranking is ambiguous at some concentrations. In Figure 7b we plot the surface concentration of Span 80 against the drug's log P with the bulk concentration held constant at 10 wt % (horizontal line). This plot shows a strong correlation between the surface enrichment effect and log P of the drug, with lower log P associated with stronger surface enrichment. Thus, for the systems investigated, the degree of surface enrichment increases as the host matrix becomes more hydrophilic. This result is sensible since a more hydrophilic medium should repel more strongly a hydrophobic

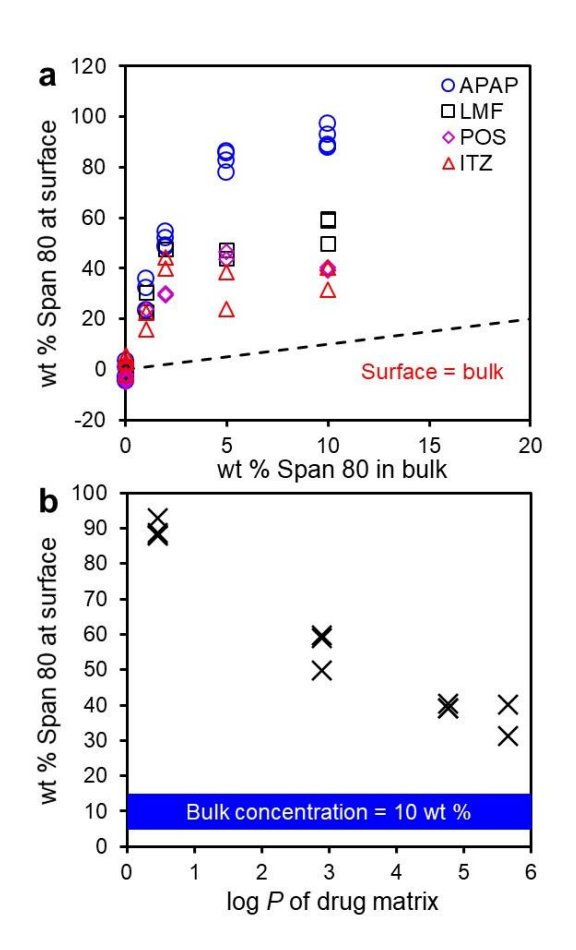


Figure 7. (a) Surface concentration of Span 80 vs. bulk concentration in 4 amorphous drugs. (b) Surface concentration of Span 80 vs. the drug's log *P* at a bulk concentration of 10 wt % (horizontal line).

(lipophilic) component. The most hydrophilic drug of the group (APAP) is thus seen to induce the strongest surface enrichment of Span 80.

Figure 8 presents a schematic summary of the results from this work. We have observed surface enrichment for all surfactants in all the drug matrices tested. The strongest effect was observed with the most lipophilic surfactant Span 80 in the most hydrophilic matrix APAP where a nearly pure surfactant layer is formed at a bulk concentration of 10 wt %. The effect weakens, though still highly significant, with increase of the surfactant hydrophilicity (HLB) and the drug's hydrophobicity. These results are fully

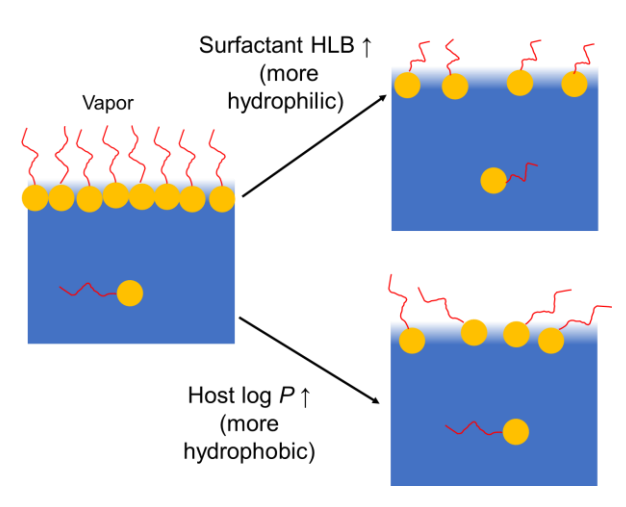


Figure 8. Schematic summary of the results from this work. Surface enrichment occurs in all systems investigated. The effect is strongest for a lipophilic surfactant in a hydrophilic matrix and weakens as the surfactant becomes more hydrophilic and the matrix more hydrophobic.

consistent with the principle of surface reorganization to minimize surface energy. At a liquid/vapor interface, the hydrophobic tail of a surfactant tends to point toward the vapor while the hydrophilic head points toward the liquid. A more hydrophilic liquid such as APAP promotes this orientation, because it excludes the surfactant's hydrophobic tails and welcomes contact with its hydrophilic heads. This low-energy configuration drives the formation of a surface layer enriched in the surfactant. As the surfactant molecule becomes more hydrophilic, there is a stronger attractive interaction with the host molecules, reducing the driving force for surface enrichment. This leads to a lower surface concentration of the surfactant molecules. Likewise, as the host liquid becomes more hydrophobic (more lipophilic), the lipophilic tail of the surfactant

has higher affinity for the host molecules and there is lower energy penalty to expose the host molecules to the vapor phase. This leads to a lower driving force for the enrichment of surfactant molecules at the liquid/vapor interface.

2.5 Conclusions

In this study, we used XPS to measure the surface enrichment effect of surfactants for the first time in amorphous drugs. We investigated four different surfactants (Span 80, Span 20, Tween 80, and Tween 20) in the common host acetaminophen, as well as the same surfactant Span 80 in four different hosts (acetaminophen, lumefantrine, posaconazole, and itraconazole). For each system, the surfactant concentrations were 0, 1, 2, 5, and 10 wt %, which cover the typical concentration in amorphous formulations, and we confirmed component miscibility in the bulk by DSC. For all systems investigated, we observed significant surface enrichment of the surfactants. For different surfactants doped in acetaminophen, strongest surface enrichment was observed for the most lipophilic Span 80 (lowest HLB). For the same surfactant Span 80 doped in different drugs, the surface enrichment effect increases with the hydrophilicity of the drug (decreasing log *P*). These effects are analogous to the surface enrichment of surfactants in aqueous solutions and fully explained by the principle of surface reorganization to minimize interfacial energy. This study highlights the potentially dramatic difference between surface and bulk concentrations in ASDs.

Surface enrichment of surfactants is expected to impact the stability, wetting, and dissolution of amorphous particles. Given their low $T_{\rm g}$, a high surfactant concentration in the surface region means enhanced local mobility, potentially leading to particle aggregation and accelerated crystallization and chemical degradation. In future work, the surface enrichment

effect should be characterized for other components in amorphous formulations (e.g., polymers) and its impact on formulation performance should be better understood. Besides thermodynamic investigations as performed here, it is of interest to determine the kinetics of surface enrichment when a fresh surface is created by fracture.

2.6 Acknowledgements

We thank BMS for supporting this work and the NSF-supported University of Wisconsin Materials Research Science and Engineering Center (DMR-1720415) for partial support and the use of its characterization facility.

2.7 References

- (1) Yu, L. Amorphous pharmaceutical solids: preparation, characterization and stabilization. *Advanced drug delivery reviews* 2001, 48, (1), 27-42.
- (2) Saboo, S.; Bapat, P.; Moseson, D. E.; Kestur, U. S.; Taylor, L. S. Exploring the Role of Surfactants in Enhancing Drug Release from Amorphous Solid Dispersions at Higher Drug Loadings. *Pharmaceutics* 2021, *13*, (5), 735.
- (3) Ghebremeskel, A. N.; Vemavarapu, C.; Lodaya, M. Use of surfactants as plasticizers in preparing solid dispersions of poorly soluble API: selection of polymer–surfactant combinations using solubility parameters and testing the processability. *International journal of pharmaceutics* 2007, 328, (2), 119-129.
- (4) Rasing, T.; Shen, Y.; Kim, M. W.; Valint Jr, P.; Bock, J. Orientation of surfactant molecules at a liquid-air interface measured by optical second-harmonic generation. *Physical Review A* 1985, *31*, (1), 537.

- (5) Peltonen, L. J.; Yliruusi, J. Surface pressure, hysteresis, interfacial tension, and CMC of four sorbitan monoesters at water–air, water–hexane, and hexane–air interfaces. *Journal of colloid and interface science* 2000, 227, (1), 1-6.
- (6) Rodríguez, A.; del Mar Graciani, M.; Angulo, M.; Moyá, M. L. Effects of organic solvent addition on the aggregation and micellar growth of cationic dimeric surfactant 12-3-12, 2Br. *Langmuir* 2007, 23, (23), 11496-11505.
- (7) Yu, L. Surface mobility of molecular glasses and its importance in physical stability. *Advanced drug delivery reviews* 2016, *100*, 3-9.
- (8) Wu, T.; Yu, L. Surface crystallization of indomethacin below T g. *Pharmaceutical research* 2006, 23, (10), 2350-2355.
- (9) Powell, C. T.; Xi, H.; Sun, Y.; Gunn, E.; Chen, Y.; Ediger, M.; Yu, L. Fast crystal growth in o-terphenyl glasses: a possible role for fracture and surface mobility. *The Journal of Physical Chemistry B* 2015, *119*, (31), 10124-10130.
- (10) Amim Jr, J.; Blachechen, L. S.; Petri, D. F. Effect of sorbitan-based surfactants on glass transition temperature of cellulose esters. *Journal of thermal analysis and calorimetry* 2012, *107*, (3), 1259-1265.
- (11) Song, Y.; Zemlyanov, D.; Chen, X.; Su, Z.; Nie, H.; Lubach, J. W.; Smith, D.; Byrn, S.; Pinal, R. Acid-base interactions in amorphous solid dispersions of lumefantrine prepared by spray-drying and hot-melt extrusion using X-ray photoelectron spectroscopy. *International journal of pharmaceutics* 2016, *514*, (2), 456-464.
- (12) Ton-That, C.; Shard, A.; Daley, R.; Bradley, R. Effects of annealing on the surface composition and morphology of PS/PMMA blend. *Macromolecules* 2000, *33*, (22), 8453-8459.

- (13) Chen, Z.; Yang, K.; Huang, C.; Zhu, A.; Yu, L.; Qian, F. Surface enrichment and depletion of the active ingredient in spray dried amorphous solid dispersions. *Pharmaceutical Research* 2018, *35*, (2), 38.
- (14) Sangster, J. LOGKOW databank. *Montreal, Quebec, Canada, Sangster Research Laboratories* 1994.
- (15) Hussain, S.; Chaudhary, V.; Jain, V.; Khar, R. K.; Yadav, M. Formulation and evaluation of liquid crystalline nanoparticles of combination drugs of antimalarials: Preformulation part.
- (16) Babalola, C. P. Experimental determination of the physicochemical properties of lumefantrine. *African journal of medicine and medical sciences* 2013, 42, (3), 209-214.
- (17) Tools, E. A., Models, Estimation Program Interface (EPI) Suite, Version 3.12; US Environmental Protection Agency, Office of Pollution Prevention and Toxics: Washington, DC, 2005. Version.
- (18) O'Neil, M. J.; Smith, A.; Heckelman, P. E. The merck index: An encyclopedia of Chemicals. *Drugs, and Biologicals* 2006, *13*.
- (19) Dinarvand, R.; Moghadam, S.; Sheikhi, A.; Atyabi, F. Effect of surfactant HLB and different formulation variables on the properties of poly-D, L-lactide microspheres of naltrexone prepared by double emulsion technique. *Journal of microencapsulation* 2005, 22, (2), 139-151.
- (20) Hurisso, B. B.; Lovelock, K. R.; Licence, P. Amino acid-based ionic liquids: using XPS to probe the electronic environment via binding energies. *Physical Chemistry Chemical Physics* 2011, *13*, (39), 17737-17748.
- (21) Hüfner, S., *Photoelectron spectroscopy: principles and applications*. Springer Science & Business Media: 2013.

- (22) Chastain, J.; King Jr, R. C. Handbook of X-ray photoelectron spectroscopy. *Perkin-Elmer*, *USA* 1992, 261.
- (23) Wagner, C.; Davis, L.; Zeller, M.; Taylor, J.; Raymond, R.; Gale, L. Empirical atomic sensitivity factors for quantitative analysis by electron spectroscopy for chemical analysis. *Surface and interface analysis* 1981, *3*, (5), 211-225.
- (24) Seah, M. P.; Dench, W. Quantitative electron spectroscopy of surfaces: A standard data base for electron inelastic mean free paths in solids. *Surface and interface analysis* 1979, *1*, (1), 2-11.
- (25) Roberts, R.; Allara, D.; Pryde, C.; Buchanan, D.; Hobbins, N. Mean free path for inelastic scattering of 1.2 kev electrons in thin poly (methylmethacrylate) films. *Surface and Interface Analysis* 1980, 2, (1), 5-10.
- (26) Sun, Y.; Tao, J.; Zhang, G. G.; Yu, L. Solubilities of crystalline drugs in polymers: an improved analytical method and comparison of solubilities of indomethacin and nifedipine in PVP, PVP/VA, and PVAc. *Journal of pharmaceutical sciences* 2010, *99*, (9), 4023-4031.

Chapter 3

Kinetics of Surface Enrichment of a Polymer in a Glass-Forming Molecular Liquid

Junguang Yu, Xin Yao, Chailu Que, Lian Huang, Ho-Wah Hui, Yuchuan Gong, Feng Qian, Lian Yu

As published in

Molecular pharmaceutics, 2022, 19(9): 3350-3357.

DOI: 10.1021/acs.molpharmaceut.2c00484

3.1 Abstract

X-ray photoelectron spectroscopy (XPS) has been used to measure the surface concentration and the surface enrichment kinetics of a polymer in a glass-forming molecular liquid. As a model, the bulk-miscible system maltitol-polyvinylpyrrolidone (PVP) was studied. The PVP concentration is significantly higher at the liquid/vapor interface than in the bulk by up to a factor of 170 and the effect increases with its molecular weight. At a freshly created liquid/vapor interface, the concentration of PVP gradually increases from the bulk value at a rate controlled by bulk diffusion. The polymer diffusion coefficient obtained from the kinetics of surface enrichment agrees with that calculated from viscosity and the Stokes-Einstein equation. Our finding allows prediction of the rate at which the surface composition equilibrates in an amorphous material after milling, fracture, and a change of ambient temperature.

3.2 Introduction

Amorphous (glassy) materials play an essential role in science and technology. An important property of glasses is compositional flexibility. While crystallization rejects impurities, glass formation often accommodates multiple components in a single phase. This leads to optical transparency and continuous tuning of composition. An important multi-component glassy material is the drug-polymer Amorphous Solid Dispersion (ASD), which is increasingly used to enhance the solubility and bioavailability of poorly soluble drugs. A typical ASD contains a drug, a polymer, and a surfactant and can be produced by spray drying, hot melt extrusion, and other methods.

Recent work has highlighted the importance of free surfaces in the fabrication and stability of glasses.⁵ Crystal growth on the surface of a glass can be orders of magnitudes faster than that in

the bulk, a consequence of the greater mobility of surface molecules.⁶ Even in the interior of a glass, fast crystal growth can occur along cracks and through self-propagating micro-fractures.⁷ Meanwhile, fast surface crystallization can be inhibited by an ultra-thin polymer coating.⁸ This coating, in essence, converts highly mobile surface molecules to less mobile bulk molecules. Besides stability, a polymer coating can improve wetting, dissolution, and other properties of an amorphous drug.⁸ All these results underscore the importance of understanding the surface composition and dynamics in developing amorphous materials.

The surface composition of a multi-component amorphous material can be significantly different from its bulk composition.^{9, 10,11,12} This is a consequence of component enrichment or deletion in the surface layer to reduce surface energy. The phenomenon is well known for the aqueous solutions of surfactants and has been observed in spray-dried milk¹³ and drug formulations.^{14, 15} Recently Yu et al. reported that common pharmaceutical surfactants can enrich at the surface of an amorphous drug, sometimes forming a nearly pure layer.¹⁶ The surface segregation of components can potentially impact the stability, wetting, and dissolution of ASDs.

Although the thermodynamics of surface enrichment is reasonably well understood, less is known about its kinetics. For a solution, compositional equilibrium is established quickly at a liquid/vapor interface. For a glass-forming material, however, the timescale for compositional equilibration could be much longer, especially for slow-diffusing macromolecules. If a fresh surface is created in an amorphous solid by fracture or milling, how long will it take for the local concentration to evolve from the initial bulk value to the final surface value? ASDs prepared by melt extrusion are often milled and compacted during tableting, both processes potentially creating fresh surfaces. Conversely, if a polymer coating is applied to an amorphous solid, what is the rate

at which the polymer migrates into the bulk? Answering these questions will help predict the stability of ASDs and the change of their performance over time.

In this study we investigate the kinetics of surface enrichment of a polymer in a glass-forming liquid. As a model the bulk-miscible system maltitol-polyvinylpyrrolidone (PVP) was studied; see Scheme 1 for their structures. Maltitol is a sugar alcohol and well-characterized glass former. PVP is a common excipient in ASDs and in wet granulation.¹⁷ X-ray photoelectron

Scheme 1. Structures of maltitol and PVP.

spectroscopy (XPS) was used to measure the surface concentration of PVP ^{13, 14,16} and its enrichment kinetics. We find that PVP has a strong tendency to enrich at the surface of maltitol and the tendency increases with its molecular weight. The rate of surface enrichment is controlled by the vertical diffusion rate of PVP to reach the surface layer and the extracted diffusion coefficients match reasonably well with those calculated from bulk viscosity and the Stokes-Einstein equation. To our knowledge, this is the first measurement of the kinetics of surface enrichment in an ultra-viscous glass-forming liquid.

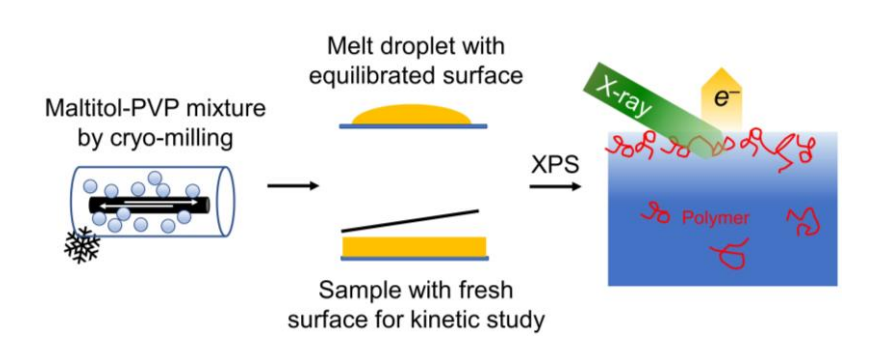
3.3 Experimental Section

Materials. Maltitol (98 %) was purchased from Sigma-Aldrich (St. Louis, MO) and purified by washing with ethanol and drying in an oven at 343-353 K. PVP K12 ($M_w = 2000-3000$ g/mol¹⁸), K15 ($M_w = 8000$ g/mol¹⁸), K30 ($M_w = 44000-54000$ g/mol¹⁸), and K90 ($M_w = 1-2$ M g/mol¹⁸) were obtained from BASF (Florham Park, NJ) and used as received. 1-Ethyl-2-

pyrrolidone (98 %, "VP monomer") was purchased from Sigma-Aldrich (St. Louis, MO) and used as received.

Sample Preparation. Scheme 2 illustrates the steps of sample preparation and analysis. Maltitol-PVP mixtures were prepared by cryo-milling¹⁹ (SPEX CertiPrep model 6750, Metuchen,

NJ) using liquid nitrogen as coolant, followed by melting. Each mixture was 1 g and milled at 10 Hz for 5 cycles (5 min per cycle, 2 min cooldown between cycles). For a mixture



Scheme 2. Sample preparation and analysis.

in the 10–40 wt % PVP range, the ingredients were weighed and milled together. The 1 wt % mixture was obtained by diluting the 10 wt % mixture followed by cryo-milling. The 0.1 wt % mixture was obtained by diluting the 1 wt % mixture followed by cryo-milling.

Two kinds of open-surface samples were prepared. For the first kind, a 5 mg powder was melted at 430–440 K (the melting point of maltitol is 423 K) on a glass coverslip to form a droplet and held for 30 min to degas. The sample was cooled to 298 K for XPS analysis. For the second kind, a 20 mg powder was melted and degassed as above. An aluminum foil was placed on the droplet to form a flat liquid film. The sample was cooled to 298 K and the foil was removed just before analysis. The sample of the first kind was used to study a well-equilibrated liquid surface and the sample of the second kind to study a freshly made surface and the kinetics of surface enrichment. In both cases, the sample thickness was approximately 20 µm, much thicker than the probe depth of XPS (~10 nm) and the thickness of the polymer-enriched layer at the liquid/air

interface (\sim 10 nm). ^{11,12} To assess potential contamination from the Al foil, the XPS spectrum of Al (2p orbital, near 75 eV²⁰) was scanned and none was detected.

To measure the kinetics of surface enrichment, samples of the second kind (Al foil removed) were stored in a home-made mini-oven maintained at a target temperature (stable within ± 0.5 K). The oven was placed in a sealed bag loaded with Drierite. The samples were periodically removed for analysis and returned to the mini-oven for further annealing until the next time point. In each experiment, a pure maltitol sample was included as control to check for cross-contamination by observing the PVP-specific nitrogen peak in the XPS spectrum. The pure maltitol control never developed a nitrogen peak during the experiment.

Differential Scanning Calorimetry (DSC). A TA Q2000 differential scanning calorimeter (New Castle, DE) was used to determine the miscibility between maltitol and PVP. Each sample of 5–10 mg was loaded in a crimped aluminum pan. The glass transition temperature $T_{\rm g}$ was measured as the onset during heating at 10 K/min after cooling at 10 K/min under 50 mL/min N₂ purge.

X-ray Photoelectron Spectroscopy (XPS). The experimental procedure and its validation has been described in Ref. ¹⁶. Briefly, the instrument was a Thermo Scientific X-ray Photoelectron Spectrometer (Waltham, MA) with an Al Kα (1486.6 eV) source. The measurements were performed in vacuum (10⁻⁵ Pa) at 297 K. An electron flood gun was used to neutralize the surface charge for the non-conductive samples. The X-ray spot size was 400 μm. Two positions in each sample were randomly chosen for measurements. A survey for all possible elements was performed at 1 eV step and passing energy of 200 eV. High-resolution scans for quantitative measurements of elements of interest were performed at 0.1 eV step and passing energy of 50 eV. XPS spectra were analyzed using the Thermo Scientific Avantage Data System. Peak positions were calibrated

against the C 1s peak at 285.0 eV. The baseline for integration was obtained using a smart baseline function in the Avantage Data System. Based on the previous validation against 10 pure compounds, the error of the method was 5 % in atomic concentration.¹⁶

3.4 Results and Discussion

Polymer-host Miscibility. We established by DSC that PVP is miscible with maltitol in the bulk in the concentration range investigated (0–10 wt %). For this purpose, maltitol's glass

transition temperature ($T_{\rm g}$) was measured as a function of polymer concentration. Figure 1 shows that with increasing PVP concentration, $T_{\rm g}$ increases up to 40 wt % PVP (using PVP K12 as an example). Since PVP K12 has higher $T_{\rm g}$ (375 K) than maltitol (318 K), this increase is expected and indicates that the two components are miscible at least up to 20 wt %. The miscibility of PVP with maltitol is consistent with its miscibility with other polyalcohols. 22

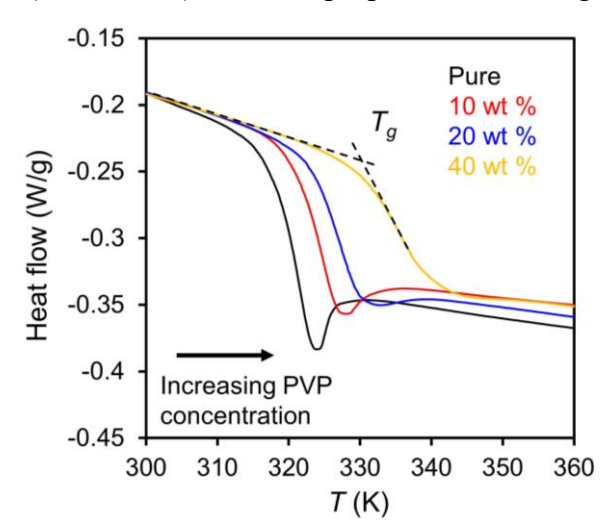


Figure 1. DSC traces showing the glass transition in maltitol doped with PVP K12. The increase of T_g with PVP concentration indicates that maltitol and PVP are miscible at least up to 20 wt %.

Surface Enrichment of PVP in Amorphous Maltitol. Figure 2 illustrates our measurement by XPS of the surface concentration of PVP in amorphous maltitol. Figure 2a shows the survey spectra for pure maltitol and maltitol doped with PVP K12 at different concentration. The peaks labeled C, O, and N correspond to the element carbon (C 1s, 285 eV), oxygen (O 1s, 533 eV), and nitrogen (N 1s, 399 eV); the area of each peak is proportional to the surface atomic

concentration of the corresponding element. These samples have been annealed for long times (see below) so that the surface composition has equilibrated. The nitrogen peak, unique to PVP (Scheme 1), is used to measure the PVP concentration. The pure maltitol shows only the C and O peaks, at a ratio of 1.12 ± 0.03 (n = 9), in agreement with the theoretical value based on its molecular formula, 1.09. The PVP K12 doped maltitol (0.1–10 wt %) all show a N peak, see Figure 2b, indicating its presence in the surface layer. The N peak is detected even at the lowest bulk concentration tested (0.1 wt %) and increases with increasing PVP concentration. In Figure 2b, the intensity of each N peak has been normalized by the intensity of the O peak so that the peak area is proportional to the N/O ratio at the surface.

Eq. 1 is used to calculate the surface concentration of PVP:

$$w_p = \frac{\frac{11k}{M_0}}{\frac{11k}{M_0} + \frac{1-k}{M_p}} \tag{1}$$

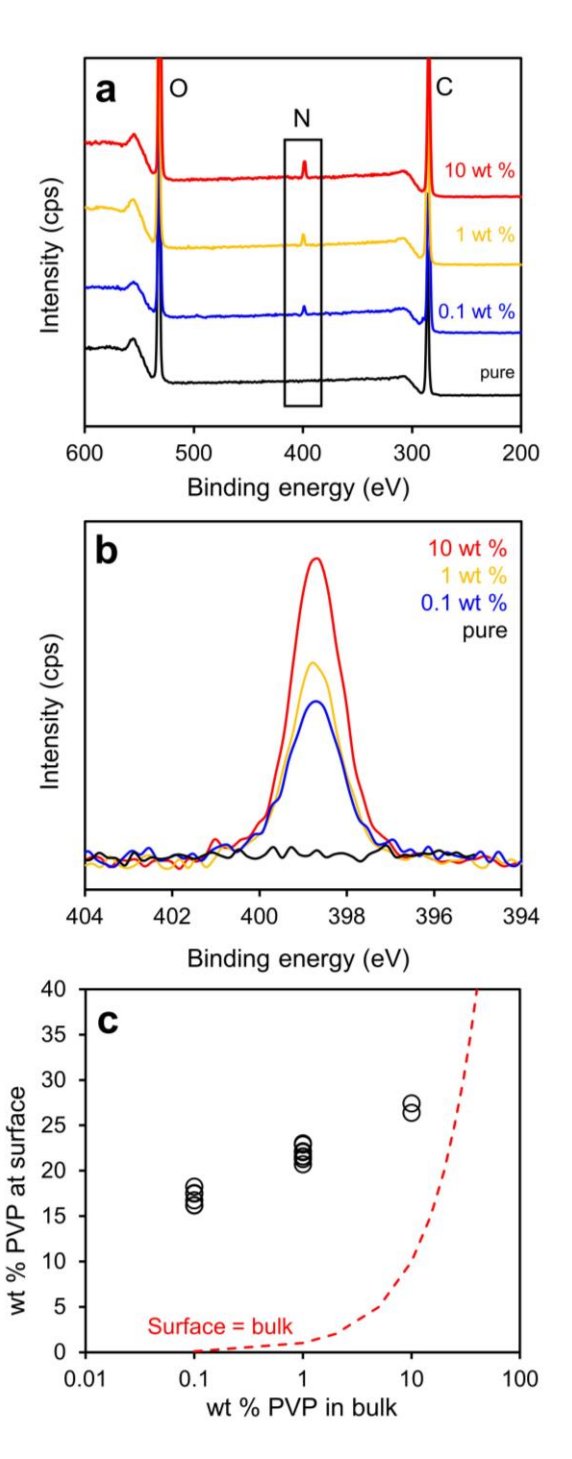


Figure 2. (a) XPS survey scans of maltitol containing PVP K12. (b) High-resolution scans of the N peak. The intensity is normalized by the O peak so the peak area is proportional to the N/O ratio. (c) Surface concentration of PVP K12 vs bulk concentration.

where w_P is the weight fraction of the polymer, M_P is the molecular weight of the monomer, M_0 is the molecular weight of maltitol, and k is the measured N/O atomic ratio. This equation assumes independent responses of atoms in the region probed by the X-ray.

Figure 2c shows the calculated surface concentration of PVP K12 in amorphous maltitol as a function of its bulk concentration. The curve indicates the condition of equal concentrations at the surface and in the bulk. We find that the polymer's surface concentration is significant higher than its bulk value. At 0.1 wt % bulk concentration, the surface concentration is 17 wt %, corresponding to a surface-enrichment factor of 170. The surface concentration of PVP increases as its bulk concentration increases, and the increase is approximately linear on the logarithm of the bulk concentration. A similar relation has been reported for the surface enrichment of a polymer solution. 9,23

For a binary solution, the component with lower surface tension is expected to enrich in the liquid/vapor interface and thus lower the overall surface energy.^{9, 14} The Prigogine-Maréchal model provides a quantitative model of this effect building on the Flory-Huggins model of polymer-solvent interactions.^{9, 23} As Scheme 1 shows, maltitol is a polyol with many polar hydroxyl groups and PVP is less polar and expected to have a lower surface energy than maltitol. As a result, we expect PVP to enrich on the surface of amorphous maltitol. (At present, the surface energies of maltitol and PVP are unknown, but we can make a rough assessment based on their analogs. Glycerol, a smaller polyol than maltitol, has a surface energy of 63.4 mN/m at 293 K.²⁴ The dimer of vinyl pyrrolidone ("VP dimer") has a surface tension of 39.8 mN/m at 299 K.¹⁴ Using these values as a guide, we expect PVP to have lower surface tension than maltitol and be the component of surface enrichment.)

Figure 3 shows how the surface concentration of PVP in amorphous maltitol changes with its molecular weight (MW), while the bulk concentration was kept constant at 1 wt %. As the MW increases, the surface concentration increases slightly. Note that the "VP monomer" shows very little surface enrichment. The surface energy of a polymer is expected to increase with its MW.²⁵ Thus, the trend observed is not driven by surface energy;

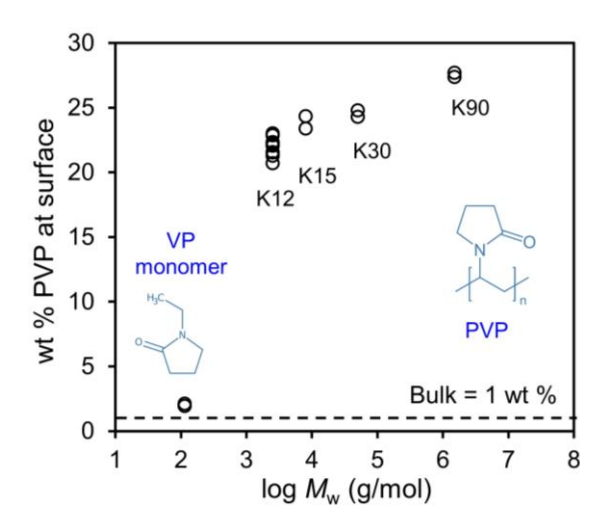


Figure 3. Surface concentration of PVP vs its molecular weight at a constant bulk concentration (1 wt %).

otherwise a decrease of surface concentration is expected with increasing MW. A possible cause for the observed effect is the reduced entropy penalty of surface segregation for larger molecules from a small-molecule host (in the Flory-Huggins theory, the entropy of mixing of a small molecule with a polymer decreases as the polymer's MW increases). 9, 23

Kinetics of Polymer Surface Enrichment. Figure 4a shows the evolution of the N peak in the XPS spectrum as a freshly prepared surface of PVP K12-doped maltitol is annealed. The bulk concentration of the polymer is 1 wt % and the annealing temperature is 328 K ($T_g + 10$ K). At time zero, no nitrogen peak was detected; with annealing, the N peak grew. This indicates an increase of the polymer concentration at the surface. Figure 4b shows the surface concentration of PVP as a function of annealing time. For the sample in Figure 4a (red symbols), the surface concentration of PVP increases from undetectable at time zero to 18 wt % after 7 days. The increase was fast initially and slowed down over time.

For comparison, Figure 4b also shows the data for an open-surface sample of the same bulk composition that had been equilibrated at a high temperature and cooled to 328 K. Initially, this sample had a high surface concentration of PVP (22 wt %) because of equilibration at high

temperature. During storage at 328 K, the surface concentration decreased slightly and stabilized at 19 wt %. This concentration agrees within experimental error with the value reached by the fresh-surface sample in Figure 4a that had been annealed only at 328 K. These two samples had different histories and approached the equilibrium state from two opposite directions. The fact that they approached the same equilibrium state indicates that the final concentration reached is the true equilibrium for surface concentration.

We interpret the results in Figure 4 as follows. For the freshly made open-surface sample in Figure 4a, the initial surface concentration of PVP was at the bulk value (1 wt %), which is below the detection limit of XPS. With annealing at 328 K, PVP's surface concentration increased and eventually plateaued. For the sample whose surface had

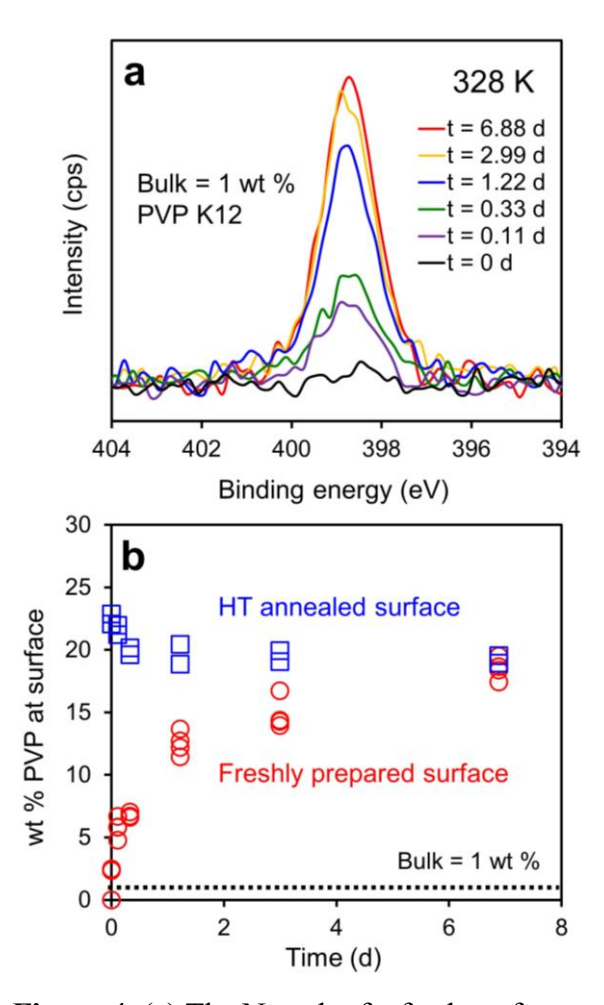


Figure 4. (a) The N peak of a fresh surface of maltitol containing 1 wt % PVP K12 at 328 K ($T_{\rm g}$ + 10 K). The intensity has been normalized by the O peak so each peak area is proportional to the surface N/O value. (b) Surface concentration of PVP vs annealing time for the sample in (a) and for an opensurface sample of the same bulk composition that had been equilibrated at high temperature before annealing at 328 K.

been equilibrated at a high temperature, the initial PVP surface concentration was high and during annealing at 328 K, only a small adjustment of surface concentration took place, reflecting the temperature effect on equilibrium surface concentration. For both samples, the evolution of the surface concentration provided information on the kinetics of surface enrichment.

Figure 5a shows the kinetics of surface enrichment of PVP at different temperatures in maltitol containing 1 wt % PVP K12. The evolution is faster at higher temperature, and in the temperature range investigated, the rate of surface enrichment spans 4 orders of magnitude. In Figure 5a, the data at different temperatures are plotted against the logarithm of time, and in this format, appear parallel to each other. This suggests that they can be collapsed to a master curve multiplying the measurement time at each temperature by a factor a_T . Figure 5b shows that this is indeed

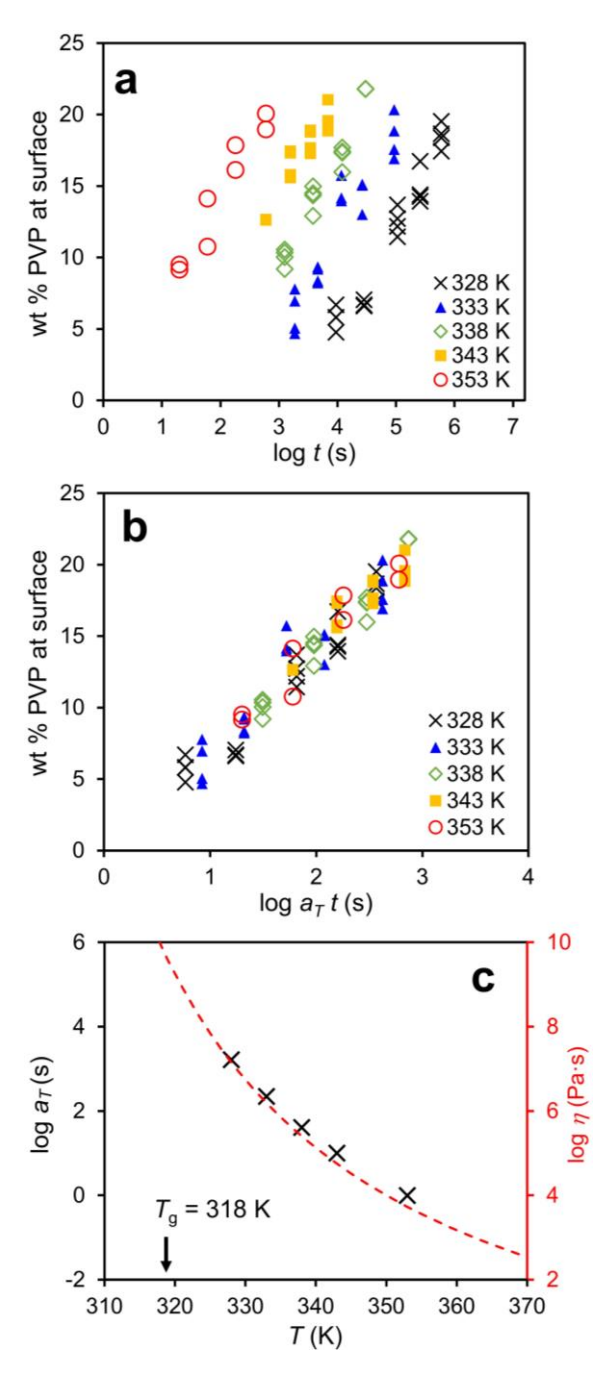
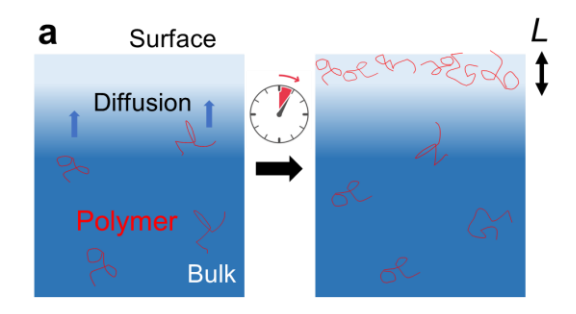


Figure 5. (a) Evolution of PVP surface concentration at different temperatures for maltitol containing 1 wt % PVP K12. (b) Master curve formed by laterally shifting the data in (a). a_T is the shift factor. (c) Temperature dependence of the shift factor a_T . The curve is the viscosity of maltitol plotted using the second y axis.

the case. This is the so-called time-temperature-superposition (TTS) behavior. According to TTS, if the surface concentration evolves as f(t) at one temperature, the evolution is given by $f(a_T t)$ at a different temperature. The factor a_T indicates the relative rates of surface enrichment at different temperatures. In forming the master curve in Figure 5b, a_T is set to 1 at 353 K.

Figure 5c shows the shift factor a_T as a function of temperature. We find that a_T increases with cooling and the temperature dependence closely follows that of maltitol's viscosity,²⁷ plotted using the second y axis. This result indicates that the kinetics of PVP surface enrichment is strongly correlated with the bulk dynamics of the host medium. Surface enrichment requires the diffusion of polymer chains from the bulk to the surface region and according to the Stokes-Einstein relation, the diffusion rate of dilute polymer chains is inversely proportional the solvent viscosity.²⁸ This is precisely the observed



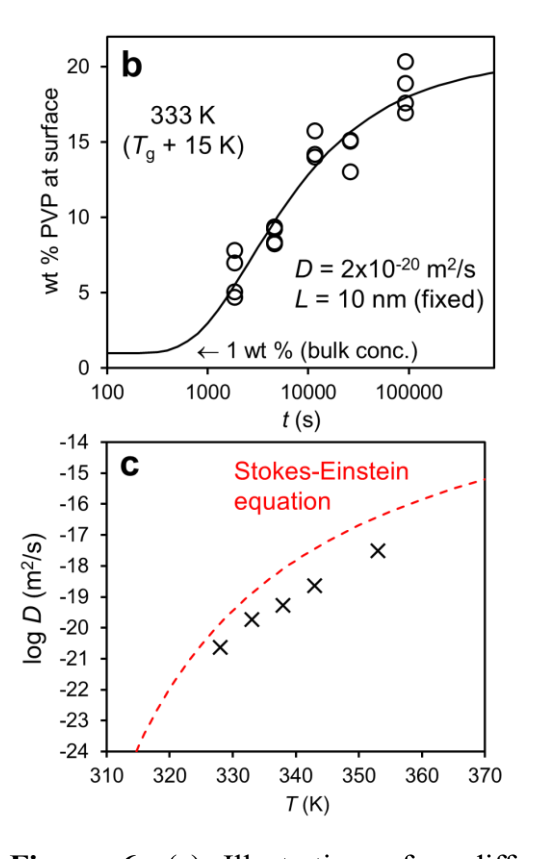


Figure 6. (a) Illustration of a diffusion-controlled surface enrichment process. (b) An example of fitting the observed enrichment kinetics to eq. 3. From the fit we obtain the diffusion coefficient D for the surface enrichment of PVP in maltitol. (c) D plotted against temperature. The curve is the bulk diffusion coefficient of dilute PVP in maltitol calculated from viscosity and the Stokes-Einstein equation.

relation in Figure 5c. Later we will quantitatively compare the diffusion coefficients calculated from the surface-enrichment kinetics and the Stokes-Einstein relation.

Building on the idea above, we use a simple diffusion model to fit the observed kinetics of surface enrichment. We imagine an adsorption process where polymer molecules diffuse from a half-space of uniform initial concentration to the free surface, saturating at the equilibrium surface concentration (Figure 6a). At equilibrium, the concentration profile of the polymer is expected to have a characteristic length on the order of 10 nm. 11,12 We assume that XPS probes the molecules within a surface layer of thickness $L \sim 10$ nm. 16 For this process, the amount observed in the probed layer is given by:

$$M(t) = A \left[1 - \operatorname{erf} \left(\frac{L}{\sqrt{4Dt}} \right) \right] + M(0)$$
 (2)

where M(0) is the amount present at time zero, M(t) is the amount at time t, D is the diffusion coefficient, and A is the increase of the amount detected at equilibrium. This equation is analogous to that for the diffusion of a thin, high-concentration surface layer into a uniform half-space and can be derived in the same way with a change of sign and boundary condition.²⁹

Dividing eq. 2 by L (probe depth) and the probe area, we obtain:

$$c(t) = \Delta c \left[1 - \operatorname{erf} \left(\frac{L}{\sqrt{4Dt}} \right) \right] + c(0) \quad (3)$$

where c(0) is the initial concentration, c(t) is the concentration at time t, and Δc is the change of concentration at equilibrium.

Figure 6b illustrates a typical fitting result. In this sample, T = 333 K, c(0) = 1 wt % (bulk concentration), and L is assumed to be 10 nm (probe depth of XPS). The fit is reasonably good and from it we obtain the diffusion coefficient for the surface enrichment of PVP K12 in maltitol: log $D(m^2/s) = -19.7$. This and other values of D are plotted in Figure 6c against temperature. The

curve in Figure 6c is the bulk diffusion coefficient of dilute PVP in maltitol calculated from the Stokes-Einstein equation:

$$D = k_{\rm B}T/(6\pi\eta R_{\rm g}) \qquad (4)$$

where η is maltitol's viscosity²⁷ and $R_{\rm g}$ is the radius of gyration of the polymer. For PVP K12, $R_{\rm g}=1.23$ nm in an aqueous solution according to quasi-elastic light scattering³⁰ and we assume the same value holds for maltitol as solvent. Figure 6c shows a reasonable agreement between the polymer diffusion coefficients for surface enrichment and bulk diffusion (from eq. 4). The D values for surface enrichment appear to be smaller (by a factor of ~10), but the difference could arise from the errors in $R_{\rm g}$ and the assumed probe depth of XPS. In fact, it seems more surprising that the diffusion rates in the surface region are so *similar* to those in the bulk, a point to be discussed below.

Vertical and Lateral Diffusion in the Surface Layer. Molecules in the surface region of a liquid have different structure and dynamics from those in the bulk. In a molecular glass, surface diffusion is often vastly faster than bulk diffusion.⁵ For a multicomponent liquid, the surface composition generally differs from the bulk composition. Given these effects, it might come as a surprise that PVP diffusion in the near-surface region of maltitol has about the same rate as that in the bulk (Figure 6c). Several factors could contribute to this result. First, the diffusion measured in this work is the *vertical* migration of polymer chains toward the surface (Figure 6a), whereas the surface diffusion measured in the previous work (e.g., through the flattening of surface gratings)⁵ is the *lateral* migration of molecules. These two rates need not be the same. For polystyrene, the vertical diffusion rate near the surface was measured using isotope-labeled layers and found to be slower than bulk diffusion.³¹ Second, maltitol is a hydrogen-bonded liquid and its lateral surface diffusion is substantially slower than that in non-associating van der Waals liquids.³²

This is a result of the robustness of hydrogen bonds: on going from the bulk to the surface, the number of hydrogen bonds per molecule does not change significantly, leaving the activation barrier for diffusion largely unchanged. Third, even for the lateral surface migration, a polymer may have much lower mobility than a small molecule. This is not only because a polymer is larger but also because it may penetrate deeper into the bulk where mobility is low.³³ This would anchor the polymer chains and limit their lateral center-of-mass migration. Together, these effects make the observed polymer diffusion rate for surface enrichment essentially the same as that for bulk diffusion.

Significance for ASD stability and performance. The key result of this work is that the polymer concentration at the surface of an ASD can deviate from its bulk concentration and the rate at which the surface concentration equilibrates is controlled by the rate of polymer diffusion through the host medium. It is important to note that throughout this process, the components

remain miscible in the bulk and the concentration change occurs only in the surface layer. Because the surface is only a small portion of the overall material, the surface enrichment effect will not significantly alter the bulk concentration. We now consider the significance of our finding in the development of ASDs.

We first consider the timescale for the surface concentration to equilibrate after the creation of a fresh surface. Figure 7

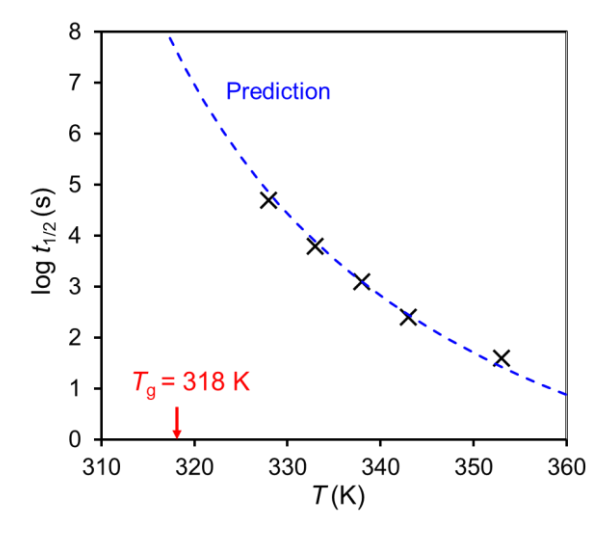


Figure 7. $t_{1/2}$ for the surface enrichment of PVP K12 in amorphous maltitol. $t_{1/2}$ is the time for the surface concentration to reach the halfway between the initial bulk value and the equilibrium surface value. The symbols are the measured data; the curve is the scaled viscosity.

shows the surface equilibration time of PVP K12 in maltitol as a function of temperature. We plot the time for the surface composition to reach the midpoint between the initial bulk concentration and the equilibrium surface concentration, $t_{1/2}$. The symbols are the measured data points (Figure 5a), ranging from minutes to one day. The curve is the viscosity of maltitol that has been scaled to coincide with the measured points. The good match between the data points and the scaled viscosity allows us to predict the surface equilibration time at lower temperatures. A decrease of temperature from the region of measurement would quickly slowdown the surface enrichment process. This is a consequence of the rapid rise of viscosity with cooling in a glass-forming molecular liquid. At T_g (318 K), $t_{1/2}$ is predicted to be one year. The result in Figure 7 pertains to PVP in the molecular weight (MW) grade K12 and a change of MW is expected to alter the polymer's diffusivity and its $t_{1/2}$ value. In the framework of the Stokes-Einstein relation (eq. 4), this effect can be estimated from the dependence of the polymer's R_g on MW. According to eq. 4, $D \propto R_g^{-1}$ and $t_{1/2} \propto D^{-1} \propto R_g$. For PVP, changing the MW grade from K12 to K90 increases R_g by a factor of 15,30 and is expected to decrease D and increase $t_{1/2}$ by the same factor.

The slow equilibration of a polymer's surface concentration in an amorphous system at low temperatures (near T_g or below) explains why a surface-deposited polymer nano-coating on an amorphous drug can persist for a long time, with little sign of migration into the bulk. This enables the coating to suppress surface mobility and inhibit surface crystallization. The long-lasting coating has additional benefits of improving wetting and dissolution. Conversely, if fresh surfaces are created in an amorphous formulation by milling or fracture, the surface composition might not equilibrate immediately but would evolve slowly during storage. The evolution could be accelerated by heating above T_g and possibly by exposure to moisture. The effects discussed above pertain to the slow-diffusing polymers. For a high-mobility component in an ASD (e.g., a

surfactant),¹⁶ the rate of surface equilibration should be faster than that of a polymer. If a fresh surface is created in an ASD, the surfactant will likely migrate to the surface faster than the polymer, causing a local segregation of excipients.

Recently, Yao et al. reported that crystal nucleation is vastly enhanced at the liquid/vapor interface of D-arabitol relative to the bulk and selects a different polymorph.³⁴ They found that this process is inhibited by a PVP in trace amount because of the surface-enrichment effect. At a bulk concentration of 20 ppm, the surface concentration of PVP K30 is 15 % or 10⁴ times higher, leading to significant inhibition of surface nucleation. This example illustrates a potentially significant effect of polymer surface enrichment on drug crystallization in an ASD. The magnitude of the effect will vary system to system, depending on the surface concentration of the polymer, on the surface-to-volume ratio, and on whether crystal nucleation or growth is considered.

3.5 Conclusions

Using XPS we have measured the kinetics of surface enrichment of a polymer in a glassforming molecular liquid for the first time. We observe a strong tendency for the polymer PVP to
enrich on the surface of amorphous maltitol and this occurs while the two components are fully
miscible in the bulk. The rate of surface enrichment is controlled by the diffusion of the polymer
from the bulk to the surface. The enrichment kinetics at different temperatures show timetemperature superposition (TTS) and the multiplicative factors have the same temperature
dependence as the bulk viscosity of the host medium. Fitting the enrichment kinetics as diffusioncontrolled adsorption yielded diffusion coefficients in reasonable agreement with those calculated
from the Stokes-Einstein relation.

Our results are relevant for understating and developing amorphous materials. An amorphous material generally contains multiple components and generally has free surfaces. The free surfaces may be present in the as-prepared materials or created by grinding, fracture, and tableting. This and other studies¹¹⁻¹⁶ have shown that the surface composition of an amorphous material can be vastly different from its bulk composition even though the components are fully miscible in the bulk. This means that the properties of the material in the surface region are very different from those in the bulk region and the overall performance of the material will depend on the surface-to-volume ratio. This work has further shown that if a fresh surface is created in an amorphous material, the surface composition will evolve over time, controlled by the diffusion rate of the surface-migrating component. For the system of this study, the vertical migration rate of the polymer to the surface is reasonably well represented by its bulk diffusion rate (Figure 6c). This conclusion, if general, allows prediction of the surface-enrichment kinetics from the bulk mobility. At high temperatures, the surface composition equilibrates quickly, but if a fresh surface is created in the glassy state, the process can be slow and be highly sensitive to storage temperature, environmental moisture, and the nature of the diffusing species. This can in turn influence the stability, wettability, and dissolution of the material.

3.6 Acknowledgements

We thank BMS for supporting this work and the NSF-supported University of Wisconsin Materials Research Science and Engineering Center (DMR-1720415) for partial support and the use of its characterization facility.

3.7 References

- (1) Ediger, M. D.; de Pablo, J.; Yu, L. Anisotropic vapor-deposited glasses: hybrid organic solids. Accounts of chemical research 2019, 52 (2), 407-414.
- (2) Yu, L. Amorphous pharmaceutical solids: preparation, characterization and stabilization. Advanced drug delivery reviews 2001, 48 (1), 27-42.
- (3) Ghebremeskel, A. N.; Vemavarapu, C.; Lodaya, M. Use of surfactants as plasticizers in preparing solid dispersions of poorly soluble API: selection of polymer–surfactant combinations using solubility parameters and testing the processability. International journal of pharmaceutics 2007, 328 (2), 119-129.
- (4) Van den Mooter, G. The use of amorphous solid dispersions: A formulation strategy to overcome poor solubility and dissolution rate. Drug Discovery Today: Technologies 2012, 9 (2), e79-e85.
- (5) Yu, L. Surface mobility of molecular glasses and its importance in physical stability. Advanced drug delivery reviews 2016, 100, 3-9.
- (6) Hasebe, M.; Musumeci, D.; Powell, C. T.; Cai, T.; Gunn, E.; Zhu, L.; Yu, L. Fast surface crystal growth on molecular glasses and its termination by the onset of fluidity. The Journal of Physical Chemistry B 2014, 118 (27), 7638-7646.
- (7) Powell, C. T.; Xi, H.; Sun, Y.; Gunn, E.; Chen, Y.; Ediger, M.; Yu, L. Fast crystal growth in o-terphenyl glasses: a possible role for fracture and surface mobility. The Journal of Physical Chemistry B 2015, 119 (31), 10124-10130.
- (8) Li, Y.; Yu, J.; Hu, S.; Chen, Z.; Sacchetti, M.; Sun, C. C.; Yu, L. Polymer nanocoating of amorphous drugs for improving stability, dissolution, powder flow, and tabletability: The case of chitosan-coated indomethacin. Molecular pharmaceutics 2019, 16 (3), 1305-1311.

- (9) Siow, K.; Patterson, D. Surface thermodynamics of polymer solutions. The Journal of Physical Chemistry 1973, 77 (3), 356-365.
- (10) De Gennes, P. d. Polymer solutions near an interface. Adsorption and depletion layers. Macromolecules 1981, 14 (6), 1637-1644.
- (11) Bloch, J.; Sansone, M.; Rondelez, F.; Peiffer, D.; Pincus, P.; Kim, M.-W.; Eisenberger, P. Concentration profile of a dissolved polymer near the air-liquid interface: X-ray fluorescence study. Physical review letters 1985, 54 (10), 1039.
- (12) Lee, L.; Guiselin, O.; Lapp, A.; Farnoux, B.; Penfold, J. Direct measurements of polymer depletion layers by neutron reflectivity. Physical review letters 1991, 67 (20), 2838.
- (13) Kim, E. H.-J.; Chen, X. D.; Pearce, D. Surface composition of industrial spray-dried milk powders. 1. Development of surface composition during manufacture. Journal of Food Engineering 2009, 94 (2), 163-168.
- (14) Chen, Z.; Yang, K.; Huang, C.; Zhu, A.; Yu, L.; Qian, F. Surface enrichment and depletion of the active ingredient in spray dried amorphous solid dispersions. Pharmaceutical Research 2018, 35 (2), 38.
- (15) Chen, Y.; Chen, H.; Wang, S.; Liu, C.; Qian, F. A single hydrogen to fluorine substitution reverses the trend of surface composition enrichment of sorafenib amorphous solid dispersion upon moisture exposure. Pharmaceutical Research 2019, 36 (7), 1-12.
- (16) Yu, J.; Li, Y.; Yao, X.; Que, C.; Huang, L.; Hui, H.-W.; Gong, Y.; Qian, F.; Yu, L. Surface Enrichment of Surfactants in Amorphous Drugs: An X-ray Photoelectron Spectroscopy Study. Molecular Pharmaceutics 2022, 19 (2), 654-660.
- (17) Wyttenbach, N.; Kuentz, M. Glass-forming ability of compounds in marketed amorphous drug products. European Journal of Pharmaceutics and Biopharmaceutics 2017, 112, 204-208.

- (18) Huang, C.; Powell, C. T.; Sun, Y.; Cai, T.; Yu, L. Effect of low-concentration polymers on crystal growth in molecular glasses: a controlling role for polymer segmental mobility relative to host dynamics. The Journal of Physical Chemistry B 2017, 121 (8), 1963-1971.
- (19) Tao, J.; Sun, Y.; Zhang, G. G.; Yu, L. Solubility of small-molecule crystals in polymers: D-mannitol in PVP, indomethacin in PVP/VA, and nifedipine in PVP/VA. Pharmaceutical research 2009, 26 (4), 855-864.
- (20) Chastain, J.; King Jr, R. C. Handbook of X-ray photoelectron spectroscopy. Perkin-Elmer, USA 1992, 261.
- (21) Sun, Y.; Tao, J.; Zhang, G. G.; Yu, L. Solubilities of crystalline drugs in polymers: an improved analytical method and comparison of solubilities of indomethacin and nifedipine in PVP, PVP/VA, and PVAc. Journal of pharmaceutical sciences 2010, 99 (9), 4023-4031.
- (22) Yao, X.; Huang, C.; Benson, E. G.; Shi, C.; Zhang, G. G.; Yu, L. Effect of polymers on crystallization in glass-forming molecular liquids: equal suppression of nucleation and growth and master curve for prediction. Crystal Growth & Design 2019, 20 (1), 237-244.
- (23) Prigogine, I.; Marechal, J. The influence of differences in molecular size on the surface tension of solutions. IV. Journal of colloid science 1952, 7 (2), 122-127.
- (24) Association, G. P. Physical properties of glycerine and its solutions; Glycerine Producers' Association, 1963.
- (25) Wu, S. Surface and interfacial tensions of polymer melts. II. Poly (methyl methacrylate), poly (n-butyl methacrylate), and polystyrene. The Journal of Physical Chemistry 1970, 74 (3), 632-638.
- (26) Simon, S.; Sobieski, J.; Plazek, D. Volume and enthalpy recovery of polystyrene. Polymer 2001, 42 (6), 2555-2567.

- (27) Nakheli, A.; Eljazouli, A.; Elmorabit, M.; Ballouki, E.; Fornazero, J.; Huck, J. La viscosité du maltitol. Journal of Physics: Condensed Matter 1999, 11 (41), 7977.
- (28) Stadelmaier, D.; Kohler, W. Thermal diffusion of dilute polymer solutions: the role of chain flexibility and the effective segment size. Macromolecules 2009, 42 (22), 9147-9152.
- (29) Helfferich, F. A note on Crank's correspondence principle in diffusion with a variable diffusion coefficient. Journal of Polymer Science Part B: Polymer Letters 1963, 1 (2), 87-91. Crank, J. The mathematics of diffusion; Oxford university press, 1979.
- (30) Armstrong, J. K.; Wenby, R. B.; Meiselman, H. J.; Fisher, T. C. The hydrodynamic radii of macromolecules and their effect on red blood cell aggregation. Biophysical journal 2004, 87 (6), 4259-4270.
- (31) Pu, Y.; Rafailovich, M.; Sokolov, J.; Gersappe, D.; Peterson, T.; Wu, W.-L.; Schwarz, S. Mobility of polymer chains confined at a free surface. Physical Review Letters 2001, 87 (20), 206101.
- (32) Chen, Y.; Zhang, W.; Yu, L. Hydrogen bonding slows down surface diffusion of molecular glasses. The Journal of Physical Chemistry B 2016, 120 (32), 8007-8015.
- (33) Li, Y.; Zhang, W.; Bishop, C.; Huang, C.; Ediger, M.; Yu, L. Surface diffusion in glasses of rod-like molecules posaconazole and itraconazole: Effect of interfacial molecular alignment and bulk penetration. Soft Matter 2020, 16 (21), 5062-5070.
- (34) Yao, X.; Liu, Q.; Wang, B.; Yu, J.; Aristov, M. M.; Shi, C.; Zhang, G. G.; Yu, L. Anisotropic Molecular Organization at a Liquid/Vapor Interface Promotes Crystal Nucleation with Polymorph Selection. Journal of the American Chemical Society 2022, 144 (26), 11638–11645.

Chapter 4

Structures of Glasses Created by Multiple Kinetic Arrests

Junguang Yu, Zhenxuan Chen, Rattavut Teerakapibal, Chris Benmore, Ranko Richert, Lian Yu Yu

As published in

Journal of Chemical Physics, 2022, 156, 084504

DOI: 10.1063/5.0080846

4.1 Abstract

X-ray scattering has been used to characterize glassy itraconazole (ITZ) prepared by cooling at different rates. Faster cooling produces ITZ glasses with lower (or zero) smectic order with more sinusoidal density modulation, larger molecular spacing, and shorter lateral correlation. We find that each glass is characterized by not one, but two fictive temperatures T_f (the temperature at which a chosen order parameter is frozen in the equilibrium liquid). The higher T_f is associated with the regularity of smectic layers and lateral packing, while the lower T_f with the molecular spacings between and within smectic layers. This indicates that different structural features are frozen on different timescales. The two timescales for ITZ correspond to its two relaxation modes observed by dielectric spectroscopy: the slower δ mode (end-over-end rotation) is associated with the freezing of the regularity of molecular packing and the faster α mode (rotation about the long axis) with the freezing of the spacing between molecules. Our finding suggests a way to selectively control the structural features of glasses.

4.2 Introduction

The structure of glasses is often considered uninteresting – it is simply the structure of the precursor liquid frozen at the glass transition temperature, chaotic and hard to describe. Recent work, however, has shown that a glass structure can be highly ordered, with order parameters approaching the values typical for crystals. These anisotropic glasses are prepared by vapor deposition and by cooling liquid crystals (LCs) that possess structural order in the fluid state. Structural order in glasses is potentially useful for optimizing charge transfer and light emission in optoelectronic devices and offers an opportunity to examine how different structural features are frozen during the glass transition.

LCs can rapidly reorganize in the fluid state in response to temperature and external fields. This has led to the notion that thermotropic LC transitions are controlled by thermodynamics, rather than kinetics, and cannot be circumvented. This notion has been challenged by recent work, which finds that LC transitions in certain systems can be avoided partially or completely by cooling at moderate rates, leading to glass structures with widely different and tunable LC order. Given the multiple relaxation modes in LC systems, further work investigated whether the freezing of LC order is associated with the kinetic arrest of a given relaxation mode. For two LCs of rod-like mesogens (itraconazole and saperconazole), the freezing of smectic order has been associated with the kinetic arrest of the end-over-end rotation; for an LC of a discotic mesogen, the freezing of its columnar order has been associated with the kinetic arrest of disc tumbling.

In this study, we utilize X-ray scattering to characterize the glass structure of itraconazole (ITZ, Scheme 1), a rod-like LC mesogen, prepared by cooling at different rates. X-ray scattering can determine many structural features of a glass¹¹ and in this work, we focus on the features pertaining to the smectic layers (spacing, regularity, and shape) and the lateral

Scheme 1. Structures of itraconazole (ITZ) and posaconazole (POS).

packing within a layer (spacing and regularity). This is a fuller profiling of glass structure than the previous work on ITZ,³ which focused on the smectic-layer regularity alone. A complete profiling of glass structure is needed to determine whether different order parameters evolve together and measure specific features relevant for device performance (e.g., π – π stacking in

columnar LCs relevant for charge transfer¹²). For ITZ, we inquire whether its smectic structure and lateral packing evolve together in the equilibrium liquid and whether they freeze together by the glass transition. As a point of reference, we investigate an analogue of ITZ, posaconazole (POS, Scheme 1), which has a similar rod-like structure but no known LC phases.

We find that ITZ glasses prepared by cooling at different rates have very different structures of smectic and lateral packing. By comparison with the equilibrium liquid, we find that each glass has structural characters that correspond to the freezing of the precursor liquid at very different temperatures; that is, the glass has different fictive temperatures with respect to different structural attributes. The regularity of smectic and lateral packing is frozen at a higher temperature than the molecular spacing between or within the layers. The former corresponds to the kinetic arrest of the slow relaxation mode δ (end-over-end rotation), whereas the latter to that of the fast relaxation mode α (rotation about the long axis). These results are relevant for the rational design of glasses with specific structures.

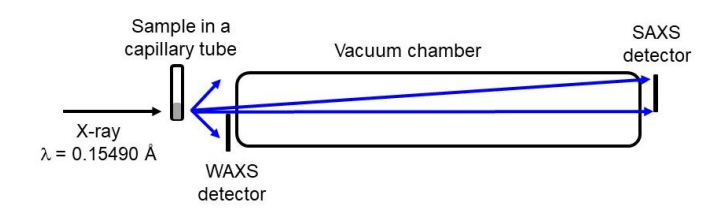
4.3 Experimental Section

Materials and Sample Preparation. Itraconazole (ITZ, 98% pure) was purchased from Alfa Aesar (Ward Hill, MA) and posaconazole (POS, 99% pure) from BioChemPartner (Shanghai). Both were used as received. Crystalline ITZ or POS powder was filled into a capillary tube (Charles Supper, MA, 1.5 mm OD, 10 μm wall thickness) and the tube was flame sealed. A glass sample was prepared by melting the crystals and cooling the melt at different rates. Cooling rates lower than 1 K/s were obtained using the DSC sample cell. Cooling rates of 1 K/s and 2 K/s were obtained using a Linkam microscope hot/cold stage. Cooling rates of 20 K/s and 120 K/s were obtained by plunging a sample tube preheated to 470 K into an ice-water

bath or a liquid nitrogen bath, respectively. The rate of cooling by a bath was measured by performing the same cooling procedure with a thermocouple coated with a layer of epoxy 1.5 mm thick.

X-ray Scattering. Simultaneous SAXS (Small Angle X-ray Scattering) and WAXS (Wide Angle X-ray Scattering) measurements were performed using a synchrotron source at the

6-ID-D beam line in the Advanced
Photon Source, Argonne National Lab.
The experimental setup is shown in
Scheme 2.^{11, 13} The temperature was
controlled by an Oxford Cryo-system
700. Two amorphous silicon area



Scheme 2. Experimental setup for simultaneous synchrotron scattering of SAXS and WAXS of ITZ glasses at 300 K.

detectors were placed at different sample-to-detector distances with each detector covering half of the azimuthal angle. Each two-dimensional image was integrated using the software FIT2D¹⁴ to yield a one-dimensional intensity vs q plot, where $q = 4\pi \sin\theta/\lambda$. Diffraction angles were calibrated using silver behenate for SAXS and CeO₂ for WAXS. The corrected intensity of coherent scattering intensity I(q) was normalized to obtain the atom-averaged X-ray structure factor:¹⁵

$$S(q) = 1 + \frac{I(q) - \langle f^2(q) \rangle}{\langle f(q) \rangle^2}$$
 (1)

where $< f^2(q) >$ is the atom-averaged self-scattering power and $< f(q) >^2$ is the atom-averaged scattering power of one molecule. The differential PDF, D(r), was obtained by a Fourier sine transform of the function F(q) = q(S(q) - 1):

$$D(r) = \frac{2}{\pi} \int_0^{q_{max}} F(q) \sin(qr) dq$$

where q_{max} is the upper bound for usable S(q) data.

X-ray scattering was also performed using the same samples with a laboratory Cu K α source. A Bruker D8 Discover Diffractometer with an Instec mK2000 heater was used to measure the q range 0.1–1 Å⁻¹; a Bruker D8 Venture Photon III four-circle diffractometer with an Oxford 700 Cryostream temperature controller was used for q = 0.35-2.8 Å⁻¹. Diffraction angles were calibrated with silver behenate or other crystals measured under the same conditions. Two-dimensional images were integrated using the software Datasqueeze¹⁶ or DIFFRAC.EVA.

Differential Scanning Calorimetry (DSC). DSC was performed with a TA Q2000 Differential Scanning Calorimeter. Each sample (3–5 mg) was placed in a crimped aluminum pan. A liquid sample of ITZ was cooled at 1–20 K/min and heated at 10 K/min to study the cooling rate effect on the glass fictive temperature $T_{\rm f}$.

4.4 Results

Structural Characterization by X-ray Scattering: Smectic and Lateral Packing.

Figure 1 shows the structure factors S(q) of two ITZ glasses prepared by cooling at different

rates: 0.08 K/s and 20 K/s. Both glasses were measured at 300 K using a synchrotron X-ray source and two detectors that covered the SAXS and WAXS regions. The structure factors of the two glasses are identical for q > 5 Å⁻¹. In this region scattering is dominated by

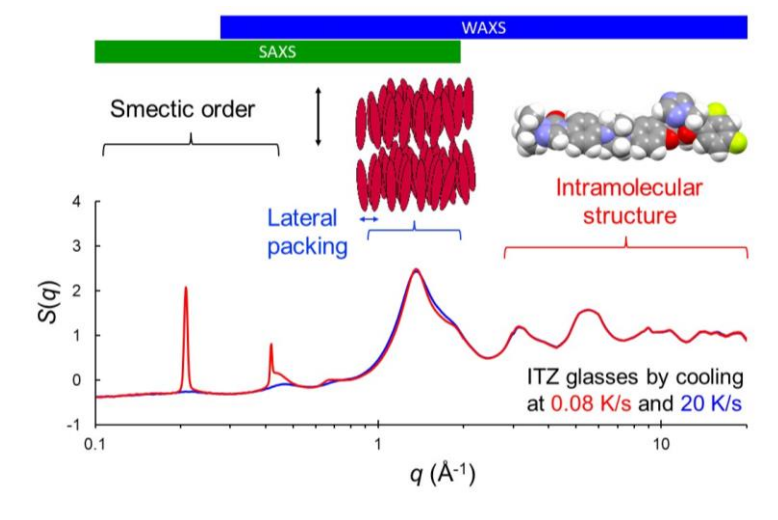


Figure 1. Structure factors of ITZ glasses at 300 K prepared by cooling at 0.08 K/s (red) and 20 K/s (blue).

the intramolecular atomic correlations. Our results thus indicate the glasses have the same intramolecular structure, as expected. The main difference between the two glasses is seen at low q. The slow-cooled glass shows sharp peaks at $q_1 = 0.2 \text{ Å}^{-1}$ and $q_2 = 0.4 \text{ Å}^{-1}$, whereas the fastcooled glass does not.³ These peaks are associated with the presence of smectic layers. The layer spacing is given by $2\pi/q_1 = 30 \text{ Å}$, about the length of the ITZ molecule. The q_2 peak is the second-order diffraction of the layers; indeed, we find $q_2/q_1 = 2$ within experimental error (see below). The broad peak at $q_L = 1.35 \text{ Å}^-$ ¹ is associated with the lateral packing of the rod-like molecule with a spacing of $\sim 2\pi/q_1 \approx 5$ Å. This peak is narrower for the slow-cooled glass than for the fast-cooled glass, indicating cooling rate not only affects smectic packing, but also lateral packing. Along with increased smectic order, the lateral packing becomes more regular. Figure 1 illustrates the range of glass structures obtainable by varying the cooling rate.

Figure 2 shows the fitting of the key structural features for later analysis. The q_1 peak (Figure 2a) is fitted with two Gaussians. The broader Gaussian arises from the excluded

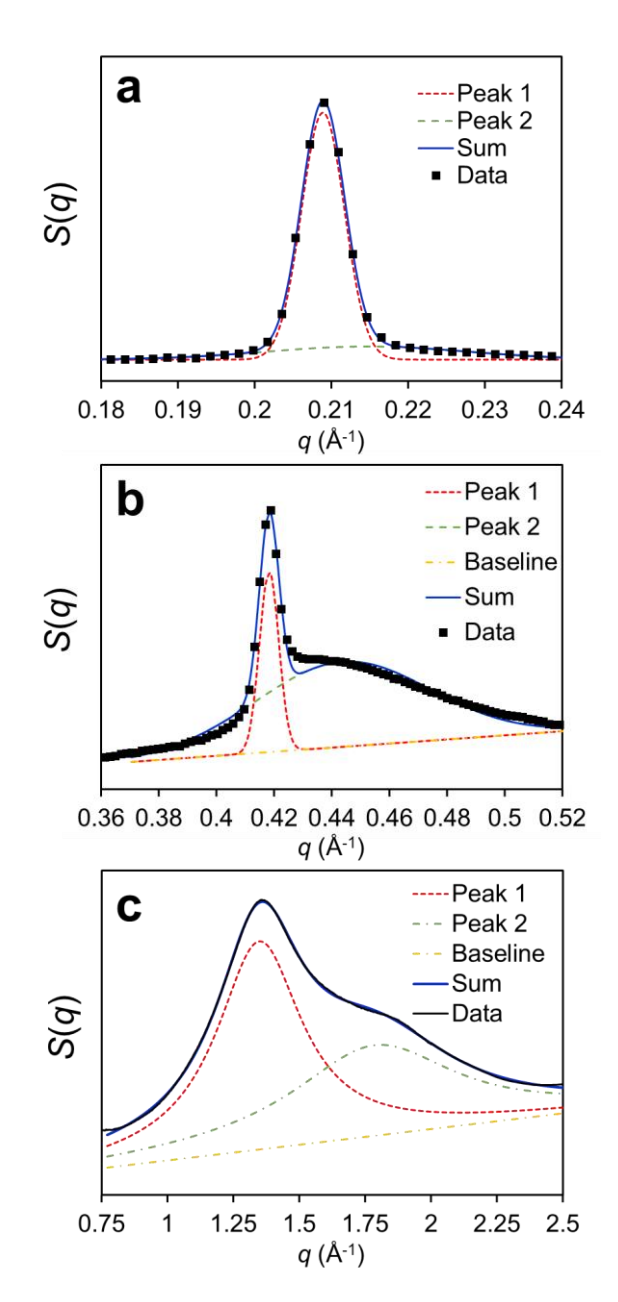


Figure 2. Fitting of key scattering peaks. The q_1 peak (a) and the q_2 peak (b) are associated with smectic order. The q_L peak (c) is associated with intralayer (lateral) packing.

volume effect¹⁷ and the sharper Gaussian (with area A_1) is used as a measure of smectic order. The q_2 peak (Figure 2b) is fitted as a sum of two Gaussians and a linear baseline. The broader component at 0.44 Å⁻¹ is again attributed to the excluded volume effect and the sharp component to the smectic structure. The presence of the q_2 peak indicates the smectic density wave is not purely sinusoidal.^{17, 18} The width of the sharp peaks is approximately 0.0066 Å⁻¹, which is mostly limited by the instrument resolution (0.0057 Å⁻¹). Thus we do not pursue the analysis of the peak width.

The feature near q_L (Figure 2c) has a main peak and a shoulder to the right. The main peak is fitted as a Lorentzian:

$$S(q) = \frac{2A}{\pi} \frac{w}{4(q - q_L)^2 + w^2}$$
 (2)

where A is the peak area, q_L is the peak position, and w is the peak width (full width at half maximum, FWHM). The Fourier sine transform of eq. 2 is an exponentially damped sine wave in real space whose wavelength is $2\pi/q_L$ and whose correlation length is $\xi = 2/w$ (ξ is the distance by which the density-wave amplitude decays by 1/e). To isolate the q_L peak, the shoulder to the right is also fitted with the function in eq. 2. Unlike the sharp smectic scattering peaks, the width of the q_L peak is not instrument-limited; in this region, the instrument resolution is $w_0 = 0.026$ Å⁻¹ (FWHM obtained by fitting crystalline diffraction peaks to Gaussian functions), approximately 5 % of the q_L peak width. Applying the correction for instrument resolution ¹⁹ to our data had no significant effect on the scattering pattern. Thus the as-observed peak width is used to calculate the lateral correlation length.

Smectic and Lateral Structures in the Equilibrium Liquid. Before investigating the

cooling rate effects on the glass structure, we first determine the temperature dependence of selected structural features in the equilibrium liquid. This is needed for calculating the fictive temperatures of glasses (see below). Figure 3 shows the temperature dependence of the positions (q_1 and q_2) and the areas (A_1 and A_2) of the smectic-scattering peaks. Results are shown near and above the DSC T_g (328 K), ensuring measurement in the equilibrium liquid state. The data were collected by accessing the temperature region both by heating a glass (open symbols) and cooling an isotropic liquid (solid symbols). The agreement of the cooling and heating data points confirms the measurement of equilibrium properties. Benmore et al. have reported the A_1 and q_1 results;¹¹ these are included in Figure 3 and in excellent agreement with our results.

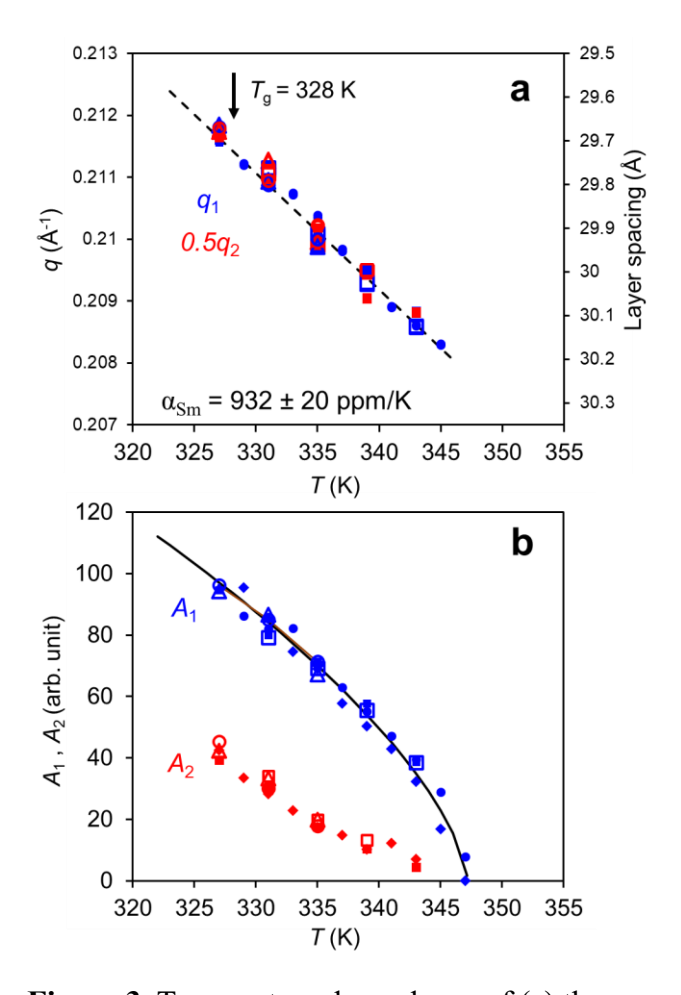


Figure 3. Temperature dependence of (a) the positions q_1 and q_2 and (b) the areas A_1 and A_2 of the smectic-scattering peaks in the equilibrium state. The data were collected by accessing the temperature region by heating a glass (open symbols) and cooling an isotropic state (solid symbols). We observe $q_2 = 2q_1$, as expected. The temperature dependence of q_1 and q_2 yields the TEC value $\alpha_{\rm Sm}$ indicated. The black curve in (b) is a power-law fitting of the A_1 data (eq. 3). Our results agree well with and extend those from Ref. 11 (solid blue circles).

With respect to the peak positions (Figure 3a), our data indicate $q_2/q_1 = 1.999 \pm 0.003$, very close to the theoretical value of 2. The spacing between the smectic layers is given by $L = 2\pi/q_1 = 4\pi/q_2$; the calculated values are shown using the right y axis. During cooling, L decreases, and the temperature dependence yields the apparent thermal expansion coefficient (TEC) for the smectic layers: $\alpha_{\rm Sm} = 932 \pm 20$ ppm/K. Notice that this one-dimensional TEC (along the LC director) is larger than the typical TEC for the volumetric expansion of molecular liquids (e.g., $\alpha_{\rm V} = 750$ ppm for o-terphenyl²⁰). The anomalously large $\alpha_{\rm Sm}$ appears to support a layer structure in which the rod-like molecules are slightly offset from each other and the degree of offset varies with temperature (see below).²¹

Figure 3b shows that with cooling, the areas of the smectic-scattering peaks, A_1 and A_2 , increase. This is expected for a smectic LC below its transition temperature. With cooling below the transition temperature, smectic order become more perfect, leading to stronger scattering. A_1 is directly related to the amplitude of density modulation¹⁷ and its temperature dependence can be described by a power law^{4, 22}:

$$A_1 = A_{10} \left[(T_{Sm/N} - T) / T_{Sm/N} \right]^x$$
 (3)

where A_{10} is a constant, $T_{\text{Sm/N}} = 347$ K is the smectic-nematic transition temperature, and x is a constant between 0 and 1. Fitting the A_1 data to eq. 3 (curve in Figure 3b), we obtain x = 0.65, close to the previous value x = 0.67 based on fewer data points.³

Figure 3b shows that the area of the q_2 peak, A_2 , has a different temperature dependence from A_1 . The presence of the q_2 peak means that the density modulation of the smectic layers is not perfectly sinusoidal. With cooling below $T_{\rm Sm/N}$, the ratio A_2/A_1 increases, from 0.2 to 0.4, indicating greater deviation from a sinusoidal density wave. To fully characterize the smectic structure, it would be of interest to determine the persistence length of density modulation from

the widths of the q_1 and q_2 peaks. But as noted above, the observed peak width is mostly limited by instrument resolution and we do not pursue this investigation here.

Figure 4 shows the temperature dependence of the lateral-packing peak q_L in the equilibrium liquid. To highlight the effect of LC order, results are also shown for the non-LC system, POS. As in Figure 3, data were collected above the DSC T_g to facilitate equilibration and the temperature region was accessed both by heating a glass (open symbols) and by cooling an isotropic liquid (solid symbols) to demonstrate the measurement of equilibrium properties.

Figure 4a shows that upon cooling, q_L increases. This signifies a reduction of the lateral spacing between molecules ($\sim 2\pi/q_L$) with cooling. ITZ and POS show very similar contraction on cooling, with comparable TEC values: $\alpha_L = 598 \pm 10$ ppm /K for ITZ, $\alpha_L = 605 \pm 10$ ppm /K for POS. This is noteworthy since in the temperature

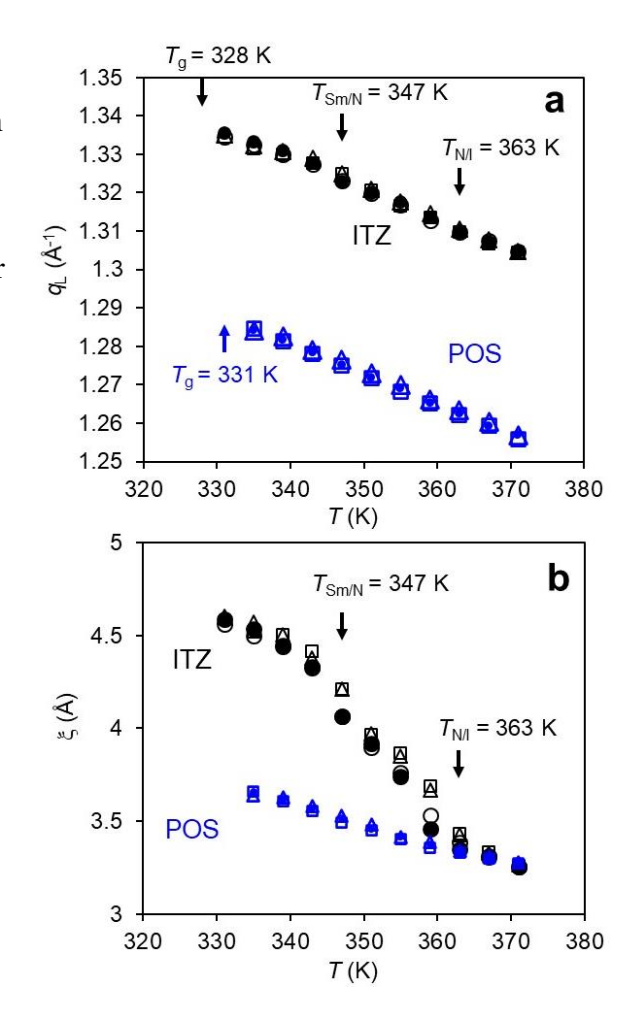


Figure 4. Temperature dependence of (a) the position q_L and (b) the correlation length ξ in the equilibrium liquid of ITZ. The data were collected by accessing the temperature region by heating a glass (open symbols) and cooling an isotropic state (solid symbols). Data are also shown for the non-LC system POS as a reference.

range studied, ITZ undergoes two LC transitions at $T_{\text{Sm/N}}$ and $T_{\text{N/I}}$, whereas POS has no LC transitions. Our results indicate that in terms of lateral spacing between molecules, the liquid

structure of ITZ evolves with temperature just like that of POS. It is also noteworthy that for ITZ, α_L is significantly smaller than the apparent TEC along the LC director α_{Sm} (932 \pm 20 ppm/K), by a factor of 1.6. This again indicates that the α_{Sm} value is anomalous and possibly a result of intralayer reorganization (see below).

Figure 4b shows the correlation length ξ for the lateral packing of ITZ and POS in the equilibrium liquid. The ξ value is calculated from: $\xi = 2/w$, where w is the width of the lateral-packing peak q_L (eq. 2). Our data show that the ξ value of POS increases linearly with cooling (densification). This behavior is well known for simple liquids (e.g., for densely packed spheres²³). In contrast to POS, the ξ value of ITZ increases more rapidly with cooling; the increase is nonlinear and appears to show jumps at the LC transition temperatures $T_{N/I} = 363$ K and $T_{Sm/N} = 347$ K. This indicates that the LC order in ITZ significantly increases the regularity of its lateral packing.

Lateral-Packing Order. Previous work has shown that cooling rate can alter the smectic order (A_1) in the ITZ glass. We now show that the same holds for other structural features but interestingly, they are affected differently by cooling rate. Figure 5 shows the cooling rate effects on the structural features associated with the smectic layers. The ITZ glasses were prepared at different cooling rates R_c and were measured at 298 K, well below its $T_{\rm g}$ (328 K). We find that faster cooling leads to lower q_1 and q_2 values (Figure 5a). This indicates that faster cooling prepares glasses with larger spacings between smectic layers. Again, we observe the relation $q_2/q_1 = 2$, allowing q_1 and $0.5q_2$ to be plotted using the same y axis.

Cooling Rate Effects on Smectic and

Figure 5b shows that faster cooling leads to lower (even zero) A_1 and A_2 values. This means that smectic order is significantly degraded (ultimately erased) by fast cooling. Figure 5c shows the ratio A_2/A_1 as a function

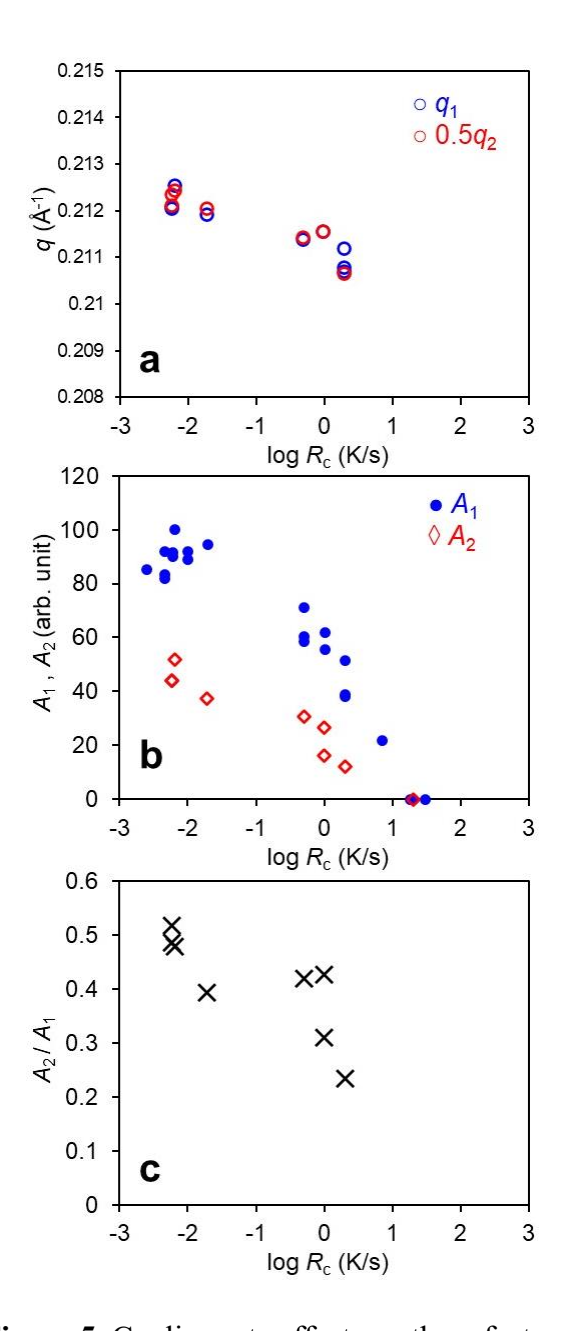


Figure 5. Cooling rate effects on three features of the smectic-scattering peaks: (a) the positions q_1 and q_2 , (b) the areas A_1 and A_2 , and the ratio A_2/A_1 . All glasses were measured at 298 K well below T_g . Faster cooling leads to lower q_1 and q_2 (larger layer spacing), lower A_1 and A_2 (lower smectic order), and A_2/A_1 ratio (more sinusoidal density modulation).

of cooling rate. Faster cooling reduces the A_2/A_1 ratio, indicating that the resulting glass contains its smectic layers with more sinusoidal density modulation.

Figure 6 shows the cooling rate effects on the structural features associated with the lateral packing. With respect to the peak position q_L (Figure 6a), faster cooling leads to smaller q_L value (larger lateral spacing). This effect is sizable, on the order of 1 % from the fastest to the slowest cooling rate. Interestingly, in terms of q_L , the cooling rate has a similar effect on ITZ and POS. This finding echoes the earlier result (Figure 4a) that the temperature has a similar effect on the q_L values of the two systems. The LC order present in ITZ is not manifested strongly in the response of the lateral spacing to the temperature

or the cooling rate.

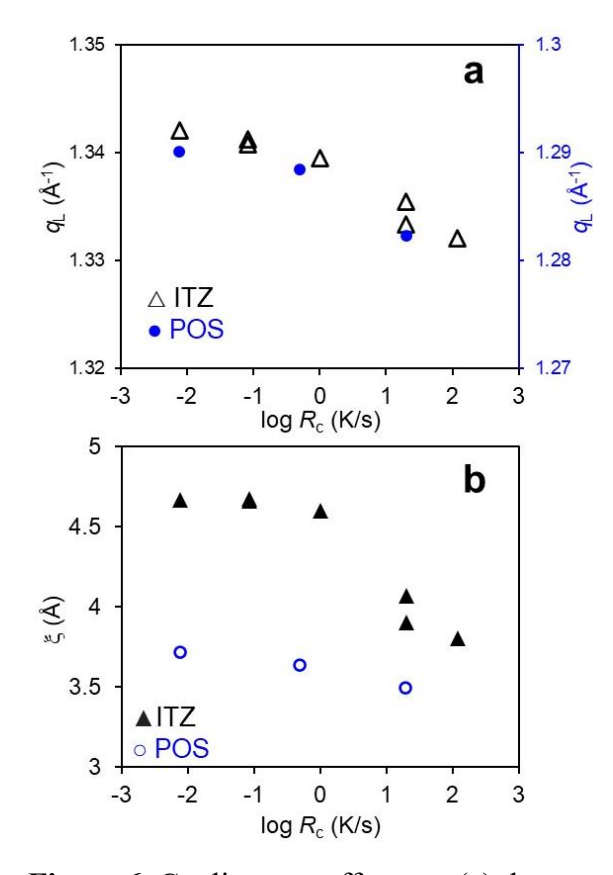


Figure 6. Cooling rate effects on (a) the position q_L and (b) correlation length ξ of the lateral-packing peak. Faster cooling produces ITZ lasses with lower q_L (larger lateral spacing) and more irregular packing. Data are also shown for the non-LC system POS as a reference.

Figure 6b shows the effect of the cooling rate on the correlation length of lateral packing ξ . Faster cooling leads to ITZ glasses with smaller ξ values (more irregular packing). In terms of this structural feature, cooling rate modifies ITZ glasses more strongly than it does POS glasses. For POS, slower cooling causes a modest increase of ξ , whereas the increase is substantially

larger for ITZ. This means that slower cooling perfects the LC structure of ITZ as well as the regularity of its lateral packing.

Fictive Temperatures of ITZ Glasses with Respect to Different Structural

Features. Having described the range of structures obtainable in glasses prepared at different cooling rates, we now consider their quantitative difference. For this purpose, we calculate the fictive temperature of each glass prepared with respect to a chosen structural measure. The fictive temperature T_f of a glass is the temperature at which the equilibrium liquid that has the same structure as the glass. A commonly used fictive temperature is defined with respect to enthalpy, $T_{\rm fH}$. For a glass of interest, $T_{\rm fH}$ is determined by measuring its enthalpy change as it is heated to the equilibrium state; from the results, one calculates the temperature $T_{\rm fH}$ at which the glass enthalpy would reach the liquid enthalpy had there been no structural change other than normal thermal expansion. In like manner, $T_{\rm f}$

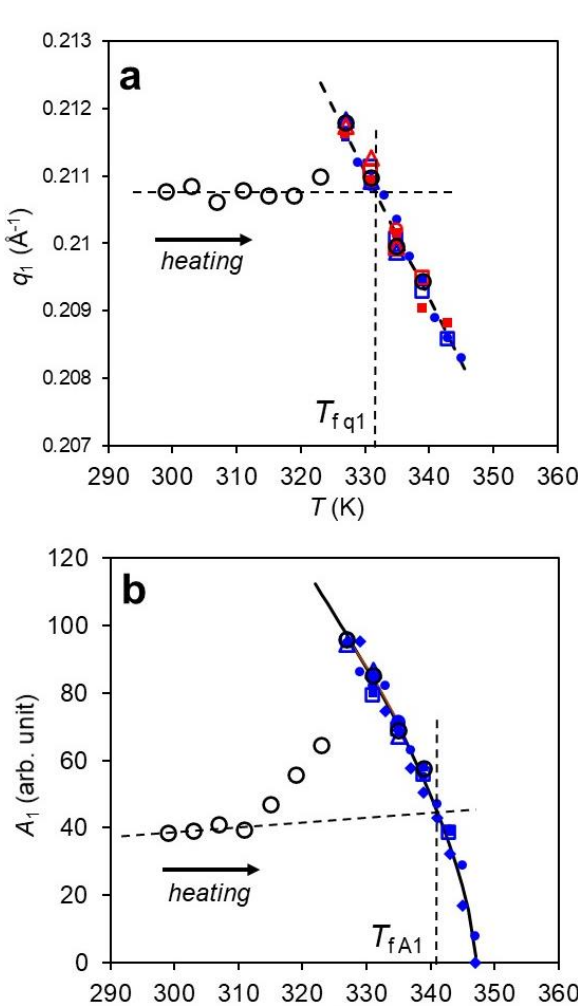


Figure 7. Measurement of the fictive temperatures of an ITZ glass with respect to two structural features characterizing the smectic layers: (a) q_1 and (b) A_1 . The glass was prepared by cooling at 2 K/s. In this experiment, it was heated while following q_1 and A_1 . The fictive temperature is the intersection of the glass line and the liquid line. The two structural measures yield significantly different T_f values.

T(K)

can be defined for volume and for the structural features studied in this work as we discuss below.

In Figure 7, we illustrate how T_f is determined for two structural features associated with the smectic layers. For a glass of interest, temperature was raised to gradually transform it into an equilibrium liquid, while monitoring a chosen structural feature. Figure 7a shows the effect of heating a glass (open circles) on its q_1 value. This glass was previously prepared by cooling at 2 K/s. At low temperatures, the q_1 value is essentially frozen in the glassy state but at high enough temperature, it joins the line for the equilibrium liquid (obtained from Figure 3a). The fictive temperature for q_1 , T_{fq1} , is obtained by extrapolating the glass line to meet the liquid line. The intersection is T_{fq1} (332 K). This procedure is completely analogous to that used to obtained the fictive temperatures based on enthalpy and volume.

Figure 7b illustrates the same procedure applied to obtain the fictive temperature of same glass as in Figure 7a but with respect to a different structural feature: A_1 (smectic order). For this property, the glass line is slightly sloped, likely a result of the effect of stress relaxation on smectic order. In addition, a rapid rise of A_1 is seen toward the equilibrium liquid line slightly below the DSC T_g , indicating a fast recovery of smectic order. From the intersection of the glass line and the liquid line, we obtain the fictive temperature, $T_{fA1} = 341$ K. Note that this value is significantly higher than T_{fq1} ; that is, in terms of q_1 , the glass corresponds to a liquid frozen at 332 K, but in terms of A_1 , it corresponds to a liquid frozen at 341 K.

Similar to Figure 7, Figure 8 illustrates how T_f is obtained for two structural features that characterize the lateral-packing order: q_L (reflecting lateral molecular spacing) and ξ (regularity of lateral packing) in the same glass. This glass was prepared by cooling at 20 K/s. Figure 8a shows the effect of heating this glass on the q_L value. At low temperatures, q_L evolves slowly in

the glassy state; at high enough temperatures, the equilibrium liquid state is reached and q_L decreases rapidly with temperature. Again, from the intersection of the glass line and the liquid line we obtain the fictive temperature, $T_{\rm fqL}$ = 337 K.

Figure 8b shows the evolution of the lateral-packing correlation length ξ during heating for the same glass as in Figure 8a. For this property, as for A_1 (Figure 7b), a rapid increase occurs near and slightly below $T_{\rm g}$. This is likely a result of the co-development of the lateral-packing order as the system gains the smectic order. Following the same procedure, we obtain the fictive temperature for ξ : $T_{\rm f}\xi = 354$ K. This value is significantly higher than T_{fqL} . In other words, the glass created by cooling at 20 K/s has the structure that corresponds to a higher temperature liquid in terms of the regularity of lateral packing and to a lower temperature liquid in terms of the lateral molecular spacing.

In Figure 9, we plot the fictive temperatures of ITZ glasses against the cooling rates used to prepare them. The fictive temperatures were calculated with respect to five structural features: q_1 , q_2 , A_1 , q_L , and ξ . In

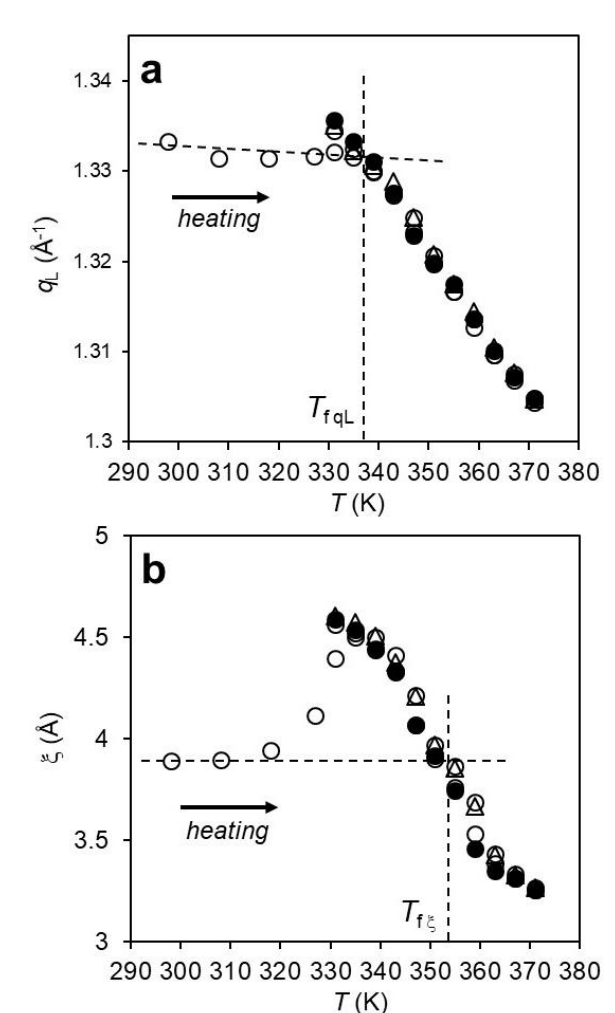


Figure 8. Measurement of the fictive temperatures of an ITZ glass relative to two features characterizing the lateral packing: (a) q_L and (b) ξ . The glass was prepared by cooling at 20 K/s. In this experiment, it was heated while following q_L and ξ . The fictive temperature is the intersection of the glass line and the liquid line. The two structural measures yield different T_f values.

addition, we include the fictive temperature based on enthalpy Hdetermined by DSC. We find that the $T_{\rm f}$ values fall into two groups. Prepared at a given cooling rate, the glass has a higher $T_{\rm f}$ with respect to $A_{\rm 1}$ and ξ and a lower $T_{\rm f}$ with respect to q_1 , q_2 , q_L , and H. Within each group, there is no significant difference between the $T_{\rm f}$ values based on different structural measures. The features frozen at a higher temperature are the perfection of the smectic layers (A_1) and the regularity of lateral packing (ξ) . These features describe the ordered arrangements of many molecules – many smectic layers in the case of A_1 and many

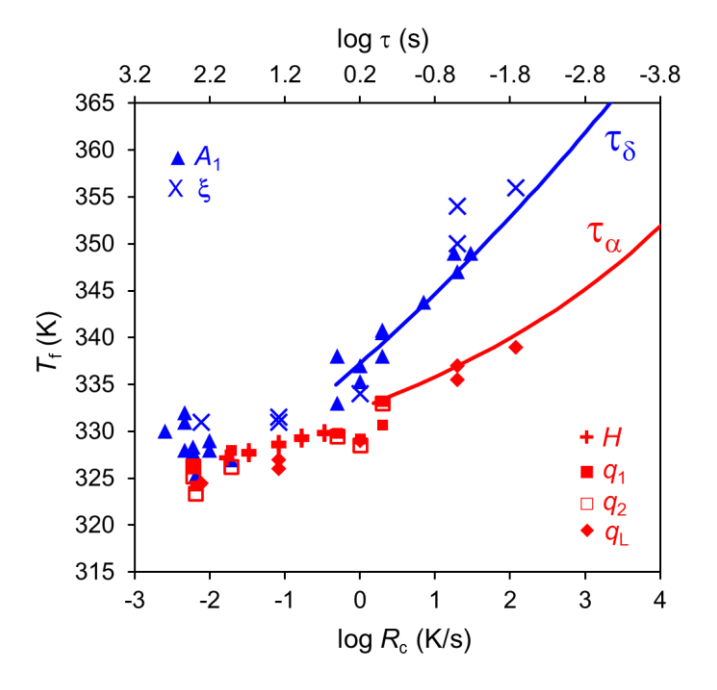


Figure 9. Cooling rate effects on the fictive temperatures T_f of ITZ glasses. For each glass, T_f has been determined relative to six of its properties. Two groups of T_f values are observed, indicating two timescales are involved in the kinetic arrest. The regularity of smectic layers and lateral packing is frozen at a higher temperature than the molecular spacings between smectic layers and within each layer as well as the enthalpy of the system.

lateral neighbors in the case of ξ . The formation of these structures presumably involves the collective movements of many molecules. The structural features that are frozen at a lower temperature include enthalpy and molecular spacings between adjacent smectic layers (captured by q_1 and q_2) and adjacent molecules within each layer (q_L). These features are closely related to the nearest-neighbor structure in the liquid. The enthalpy of a molecular liquid is dominated by the nearest-neighbor interactions; molecular spacings can be adjusted at the level of nearest neighbors, without involving the far-away neighbors. It is thus sensible that at a given cooling

rate, the order parameters that characterize the perfection of the longer-range structure (A_1 and ξ) should be frozen earlier than those that describe features that are closely related to the nearest-neighbor structure.

In Figure 9 is also plotted the two relaxation timescales of ITZ observed by dielectric spectroscopy (DS).⁸ The slower mode (δ) has been assigned to the end-over-end rotation of the rod-like molecule and the faster mode (α) to the rotation about the long axis and precession of the long axis about the electric field vector.⁹ These timescales are plotted in Figure 9 using the relation:²⁵

$$\tau R_{c} = C \tag{4}$$

where C is a constant on the order of 1 K. The physical meaning of eq. 4 is that for a system with a single relaxation time τ , kinetic arrest occurs when the cooling rate is C/τ . For this plot, C = 1.6 K, obtained by the best fit with the T_f vs R_c data. This value is slightly larger than C = 0.4 K determined by comparison with the onset of the DSC T_g during cooling.³

Figure 9 shows that for a given cooling rate, the observed T_f values are well described by the temperatures at which the α and δ relaxation modes undergo kinetic arrest according to eq. 4. Smectic order (A_1) and lateral-packing order (ξ) are frozen when the δ mode undergoes kinetic arrest; enthalpy and molecular spacings are frozen when the α mode undergoes kinetic arrest. Previous work has reached the conclusion that smectic order A_1 is controlled by the end-over-end rotation.^{3, 4} Here we expand that conclusion to include the regularity of lateral packing. Furthermore we find that the other measures of structure investigated here are frozen at a much lower temperature, the T_g of the α relaxation mode.

4.5 Discussion

We have characterized the structures of the equilibrium liquid of ITZ (Figures 3 and 4) and its glasses prepared by cooling at different rates (Figures 5 and 6). In the equilibrium liquid, the apparent thermal expansion coefficient for the smectic layer spacing significantly exceeds that for the lateral spacing and the typical value for molecular liquids. An ITZ glass prepared at a given cooling rate is characterized not by a single fictive temperature, but two (Figure 9), with the higher one associated with the regularity of smectic and lateral packing and the lower one with enthalpy, smectic layer spacing, and lateral molecular spacing. Here we discuss these results.

Anisotropic Thermal Expansion of ITZ. For ITZ, the smectic layer spacing contracts

more rapidly on cooling than the lateral spacing between molecules: $\alpha_{Sm} = 932 \pm 20$ ppm/K and $\alpha_L = 598 \pm 10$ ppm/K. Furthermore, the α_{Sm} value of ITZ is surprisingly large relative to the typical thermal expansion of molecular liquids. For example, $\alpha_V = 750$ ppm/K for *o*-terphenyl, implying a linear expansion coefficient of 250 ppm/K, almost 4-times smaller than the α_{Sm} value of ITZ. Though ITZ's α_L value is also rather large in this comparison, it is similar to that of POS (605 \pm 10 ppm/K) and thus is unrelated to LC order.

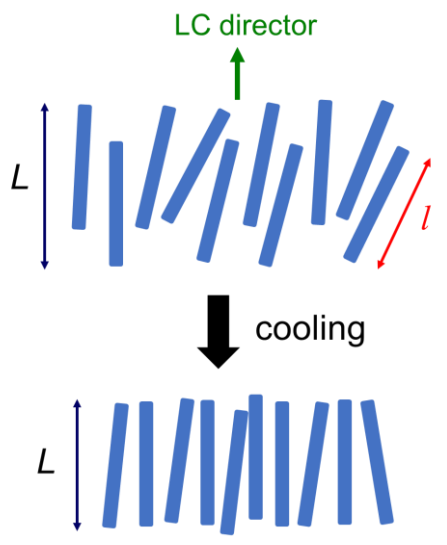


Figure 10. Internal reorganization of smectic layers that could account for a large apparent TEC.

We speculate that the unusually large α_{Sm} value of ITZ is a result of the internal reorganization of smectic layers. In a perfect smectic layer, all molecular centers of mass should lie on the same plane that is perpendicular to the LC director and the layer thickness should be the length of the molecule. But if the rod-like molecules are slightly offset from each other along

the LC director, as shown in Figure 10 with exaggeration, the apparent layer thickness would be larger. We imagine that with cooling, the offsets between the molecules become smaller and their centers of mass fall closer to the same plane. This would lead to an apparent contraction of the layer thickness that is larger than the normal thermal expansion effect. This explanation is similar to the interdigitation picture 26 to explain the much larger smectic-layer spacing L than the molecular length l and the rapid contraction of layer spacing with cooling.²¹ Relative to these systems, ITZ's values of L (~30 Å; Figure 3a) and l (~28 Å, estimated from its crystal structures) are rather close. In its smectic phase, the orientational order parameter $S = \langle 3/2 \cos^2 \theta - 1/2 \rangle =$ 0.7,8 where θ is the angle between the molecular long axis and the LC director, yielding a layer thickness $l \cos \theta = 25$ Å in the absence of molecular offsets. Comparison with observed value L = 30 Å suggests an average offset of 5 Å. This value is approximately the offset observed in the crystals of ITZ between two adjacent anti-parallel molecules along the long axis. If the average offset in the liquid state is changes by 0.5 Å in the temperature range investigated (Figure 3a), this effect alone would explain "anomalous" α_{Sm} value. The actual change of offset should be smaller if the normal contraction on cooling is considered. The picture proposed is consistent with the temperature effect on the shape of density modulation captured by the A_2/A_1 ratio (Figure 3c). If the distribution of the molecular centers of mass changes (Figure 10), so do the density modulation detected by X-ray scattering and the A_2/A_1 ratio.

Structures of Glasses Created by Multiple Kinetic Arrest. A key result of this work is that it is possible to create glasses in which the different structural features are frozen at different temperatures. Stated differently, the same glass can have multiple fictive temperatures with respect to different structural features. For an ITZ glass prepared at a given cooling rate, the regularity of its smectic layers and lateral packing corresponds to a liquid frozen at a higher

temperature, while its enthalpy and molecular spacings correspond to a liquid frozen at a lower temperature. For a glass quenched at a rate of 100 K/s, the two fictive temperatures above differ by 20 K. For this reason, some aspects of structure are altered by cooling rate to a greater extent than others. The ability to selectively alter structural features is intrinsic to glass formation since a liquid in equilibrium, by definition, is characterized by a single temperature.

The fact that smectic order and lateral correlation length are frozen at the same temperature suggests that these two aspects of structure are coupled. Since the increase of smectic order is accompanied by the more parallel alignment of the rod-like molecules (i.e., increase of orientational order),⁸ it makes sense that this also leads to more regular packing in the lateral direction. This picture is supported by the simultaneous rise of smectic order (Figure 3b) and lateral-packing order (Figure 4b) as the equilibrium liquid enters the smectic phase. The smectic order emerges from zero, while the lateral-packing order increases relative to the non-LC system POS as baseline. The lateral correlation length of POS increases linearly with cooling, while the value of ITZ shows jumps at the LC transition temperatures, supporting the simultaneous development of smectic and lateral-packing order. We note that this conclusion is contradictory to the common view that a smectic LC is ordered only with respect to the repeating layers and disordered within the layers. Instead, we find that interlayer order and intralayer order grow together.

In contrast to the regularity of smectic layers and lateral packing, we find that the glass structure gauged by enthalpy, smectic layer spacing, and lateral spacing are frozen together at a lower temperature. This result echoes the previous report that for a discotic LC, the regularity of columnar packing is frozen at a higher temperature than inter-columnar spacing.⁵ These results are sensible since the distance between molecules is easily altered at the level of the nearest

neighbors, through local vibrations and thermal expansion, without needing to rearrange molecules over long distances. As a measure of structure, enthalpy is more sensitive to the nearest neighbors than to the longer-range structure and this explains why enthalpy is placed in the same group with intermolecular spacings in its response to cooling rate.

It is intriguing that the two timescales for kinetic arrest correspond to the two relaxation modes observed by DS. The interpretation of these relaxation modes as fast rotation about the long axis (α) and slow rotation end-over-end (δ) is consistent with the picture proposed above. Between the two processes, the δ mode has a larger activation volume in the sense that molecules in a "log jam" must be shoved around in order to execute an end-over-end rotation, whereas the fast axial rotation (the α mode) requires less coordination with the neighbors and should have a smaller activation volume. It makes sense that the state of the log jam is frozen at a higher temperature than the axial rotation of individual logs. This interpretation is consistent with the finding that volume relaxation correlates with the α process.²⁷ In the case of ITZ, TMDSC shows that enthalpy relaxation correlates with the α mode.⁸

4.6 Conclusions

In this study, we characterized the structures of ITZ glasses prepared at different cooling rates by X-ray scattering. We find that these glasses have very different structures, with faster cooling leading to lower (zero) smectic order, less regular lateral packing, and larger molecular spacings. The different structures can be characterized by two fictive temperatures, the higher one related to the regularity of smectic and lateral packing and the lower one to molecular spacings and enthalpy. The difference between the two fictive temperatures is as large as 20 K. Our results indicate that the interlayer and intralayer order in a smectic structure rise and fall together as part

of liquid crystallinity, whereas the structural features associated with the nearest-neighbor environment can actively evolve even when the LC framework is frozen. At each cooling rate, the two fictive temperatures correspond to the glass transition temperatures for the two relaxation modes of ITZ observed by DS. The slower δ mode (end-over-end rotation) is associated with the freezing of the smectic and lateral-packing order and the faster α mode (axial rotation) with the freezing of molecular spacings and enthalpy.

Our results indicate that the different aspects of glass structure can be manipulated independently in systems similar to ITZ that have multiple and widely separated relaxation modes, including other saperconazole. For these systems, multiple kinetic arrests can be engineered to target selected structural features. This is an ability intrinsic to glass formation. Apart from the anisotropy of molecular shape, multiple relaxation modes in a liquid can arise from the presence of slow- and fast-relaxing components, from internal rotations of different rates, and from the supramolecular structure created by hydrogen bonds. Application of this principle could lead to glasses with tailor-made properties for applications in organic electronics and pharmaceutics. Future progress in this area will benefit from the determination of the range over which the fictive temperatures can differ in the same glass and how the fictive temperatures evolve during glass aging. Since two timescales are involved in glass preparation, it is of interest to determine whether the same two timescales control glass aging.

4.7 Acknowledgements

We thank the NSF (DMR-1904601) for supporting this work and the NSF-supported University of Wisconsin Materials Research Science and Engineering Center (DMR-1720415) for the use of its characterization facility.

4.8 References

- (1) Gujral, A.; Yu, L.; Ediger, M. Anisotropic organic glasses. Current Opinion in Solid State and Materials Science 2018, 22 (2), 49-57.
- (2) Bagchi, K.; Ediger, M. D. Controlling structure and properties of vapor-deposited glasses of organic semiconductors: Recent advances and challenges. The Journal of Physical Chemistry Letters 2020, 11 (17), 6935-6945.
- (3) Teerakapibal, R.; Huang, C.; Gujral, A.; Ediger, M. D.; Yu, L. Organic glasses with tunable liquid-crystalline order. Physical review letters 2018, 120 (5), 055502.
- (4) Chen, Z.; Yu, J.; Teerakapibal, R.; Meerpoel, L.; Richert, R.; Yu, L. Organic glasses with tunable liquid-crystalline order through kinetic arrest of end-over-end rotation: the case of saperconazole. Soft Matter 2020, 16 (8), 2025-2030.
- (5) Chen, Z.; Bishop, C.; Thoms, E.; Bock, H.; Ediger, M. D.; Richert, R.; Yu, L. Controlling the Columnar Order in a Discotic Liquid Crystal by Kinetic Arrest of Disc Tumbling. Chemistry of Materials 2021, 33 (12), 4757-4764.
- (6) Yokoyama, D. Molecular orientation in small-molecule organic light-emitting diodes. Journal of Materials Chemistry 2011, 21 (48), 19187-19202.
- (7) Yang, D.-K.; Wu, S.-T. Fundamentals of liquid crystal devices; John Wiley & Sons, 2014.
- (8) Tarnacka, M.; Adrjanowicz, K.; Kaminska, E.; Kaminski, K.; Grzybowska, K.; Kolodziejczyk, K.; Wlodarczyk, P.; Hawelek, L.; Garbacz, G.; Kocot, A. Molecular dynamics of itraconazole at ambient and high pressure. Physical Chemistry Chemical Physics 2013, 15 (47), 20742-20752.
- (9) Brás, A.; Dionísio, M.; Huth, H.; Schick, C.; Schönhals, A. Origin of glassy dynamics in a liquid crystal studied by broadband dielectric and specific heat spectroscopy. Physical Review E

- 2007, 75 (6), 061708. Kremer, F.; Schönhals, A. Broadband dielectric spectroscopy; Springer Science & Business Media, 2002. Martin, A. J.; Meier, G.; Saupe, A. Extended Debye theory for dielectric relaxations in nematic liquid crystals. In Symposia of the Faraday Society, 1971; Royal Society of Chemistry: Vol. 5, pp 119-133.
- (10) Schönhals, A.; Zubowa, H. L.; Fricke, R.; Frunza, S.; Frunza, L.; Moldovan, R. On the Dielectric Behavior of Unaligned Samples of 4-n-Octyl-4'-cyanobiphenyl (8CB). Crystal Research and Technology: Journal of Experimental and Industrial Crystallography 1999, 34 (10), 1309-1314.
- (11) Benmore, C.; Mou, Q.; Benmore, K.; Robinson, D.; Neuefeind, J.; Ilavsky, J.; Byrn, S.; Yarger, J. A SAXS-WAXS study of the endothermic transitions in amorphous or supercooled liquid itraconazole. Thermochimica Acta 2016, 644, 1-5.
- (12) Kaafarani, B. R. Discotic liquid crystals for opto-electronic applications. Chemistry of Materials 2011, 23 (3), 378-396.
- (13) Benmore, C.; Alderman, O.; Robinson, D.; Jennings, G.; Tamalonis, A.; Ilavsky, J.; Clark, E.; Soignard, E.; Yarger, J.; Weber, J. Extended range X-ray pair distribution functions. Nuclear Instruments and Methods in Physics Research Section A: Accelerators, Spectrometers, Detectors and Associated Equipment 2020, 955, 163318.
- (14) Hammersley, A. FIT2D: a multi-purpose data reduction, analysis and visualization program. Journal of Applied Crystallography 2016, 49 (2), 646-652.
- (15) Benmore, C. J. X-Ray Diffraction from Glass. Modern Glass Characterization 2015, 1-30.
- (16) Heiney, P. A. Datasqueeze: A software tool for powder and small-angle X-ray diffraction analysis. Newsletter of the IUCr Commission on Powder Diffraction 2005, 32, 9-11.

- (17) McMillan, W. X-ray scattering from liquid crystals. I. Cholesteryl nonanoate and myristate. Physical Review A 1972, 6 (3), 936.
- (18) Takanishi, Y.; Ikeda, A.; Takezoe, H.; Fukuda, A. Higher smectic-layer order parameters in liquid crystals determined by x-ray diffraction and the effect of antiferroelectricity. Physical Review E 1995, 51 (1), 400. Gramsbergenf, E.; De Jeu, W. X-ray study of the sharpness of the smectic A layer structure. Liquid Crystals 1989, 4 (4), 449-455.
- (19) Jones, A.; Misell, D. A practical method for the deconvolution of experimental curves. British Journal of Applied Physics 1967, 18 (10), 1479.
- (20) Greet, R.; Turnbull, D. Glass transition in o-terphenyl. The Journal of Chemical Physics 1967, 46 (4), 1243-1251.
- (21) Madhusudana, N.; Srikanta, B.; Subramanya Raj Urs, M. Studies on some smectogenic compounds with large bilayer spacings. Molecular Crystals and Liquid Crystals 1983, 97 (1), 49-75.
- (22) Kapernaum, N.; Giesselmann, F. Simple experimental assessment of smectic translational order parameters. Physical Review E 2008, 78 (6), 062701.
- (23) Perry, P. t.; Throop, G. Decay of pair correlations in hard sphere fluids. The Journal of Chemical Physics 1972, 57 (5), 1827-1829.
- (24) Moynihan, C.; Lee, S.-K.; Tatsumisago, M.; Minami, T. Estimation of activation energies for structural relaxation and viscous flow from DTA and DSC experiments. Thermochimica acta 1996, 280, 153-162.
- (25) Hensel, A.; Schick, C. Relation between freezing-in due to linear cooling and the dynamic glass transition temperature by temperature-modulated DSC. Journal of non-crystalline solids 1998, 235, 510-516.

- (26) Leadbetter, A.; Frost, J.; Gaughan, J.; Gray, G.; Mosley, A. The structure of smectic A phases of compounds with cyano end groups. Journal de Physique 1979, 40 (4), 375-380. Palermo, M. F.; Pizzirusso, A.; Muccioli, L.; Zannoni, C. An atomistic description of the nematic and smectic phases of 4-n-octyl-4' cyanobiphenyl (8CB). The Journal of chemical physics 2013, 138 (20), 204901.
- (27) Simon, S.; Sobieski, J.; Plazek, D. Volume and enthalpy recovery of polystyrene. Polymer 2001, 42 (6), 2555-2567.
- (28) Savin, D. A.; Larson, A. M.; Lodge, T. P. Effect of composition on the width of the calorimetric glass transition in polymer–solvent and solvent–solvent mixtures. Journal of Polymer Science Part B: Polymer Physics 2004, 42 (7), 1155-1163.
- (29) Böhmer, R.; Gainaru, C.; Richert, R. Structure and dynamics of monohydroxy alcohols—Milestones towards their microscopic understanding, 100 years after Debye. Physics Reports 2014, 545 (4), 125-195.

Chapter 5

Engineering the Glass Structure of a Discotic Liquid Crystal by Multiple Kinetic Arrests

Junguang Yu, Zhenxuan Chen, Caroline Fatina, Debaditya Chatterjee, Harald Bock, Ranko Richert, Paul Voyles, M. D. Ediger, Lian Yu

As published in

Journal of Chemical Physics, 2023, 158, 204503

DOI: 10.1063/5.0149886

5.1 Abstract

X-ray scattering has been used to characterize the columnar packing and the π stacking in a glass-forming discotic liquid crystal. In the equilibrium liquid state, the intensities of the scattering peaks for π stacking and columnar packing are proportional to each other, indicating concurrent development of the two orders. Upon cooling into the glassy state, the π - π distance shows kinetic arrest with a change of the thermal expansion coefficient (TEC) from 321 ppm/K to 109 ppm/K, while the intercolumnar spacing exhibits a constant TEC of 113 ppm/K. By changing the cooling rate, it is possible to prepare glasses with a wide range of columnar and π stacking order, including zero order. For each glass, the columnar order and the π stacking order correspond to a much hotter liquid than its enthalpy and π - π distance, with the difference between the two internal (fictive) temperatures exceeding 100 K. By comparison with the relaxation map obtained by dielectric spectroscopy, we find that the δ mode (disc tumbling within a column) controls the columnar order and the π stacking order trapped in the glass, while the α mode (disc spinning about its axis) controls the enthalpy and the π - π spacing. Our finding is relevant for controlling the different structural features of a molecular glass to optimize its properties.

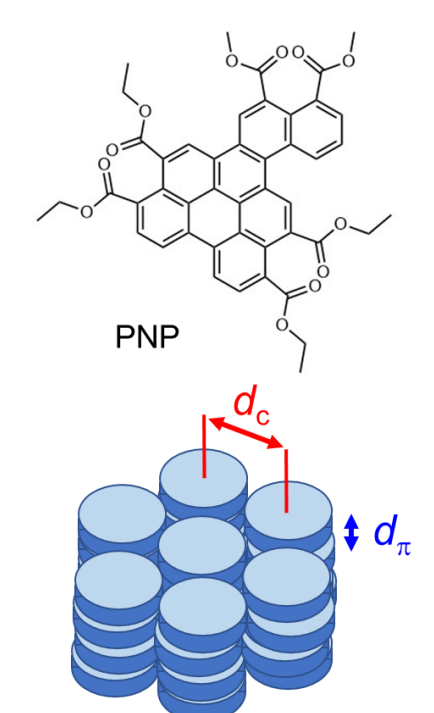
5.2 Introduction

A glass is formed by cooling a liquid while avoiding crystallization. At the glass transition, a flowing liquid hardens to a solid. As materials, glasses provide liquid-like macroscopic homogeneity, ability to dissolve multiple components in a single phase, ease of processing (e.g., drawing fibers), and higher solubility than crystals. A limitation in traditional glass fabrication, however, is that each glass has one liquid phase as precursor and thus a narrow range of structures.

In contrast, crystal polymorphs are often exploited as a tool for structural modification in crystal engineering. It is desirable to develop similar capabilities in glass engineering.

Glass-forming liquid crystals (LC) provide an opportunity to systematically control the structure of glasses. Molecules in a LC can be highly ordered in the fluid state and that order can be frozen in a glass.¹⁻⁴ Recent work has shown that LC order is not only *transferable* to a glass but also *tunable* by adjusting the cooling rate.⁵⁻⁷ For the calamitic LCs itraconazole and saperconazole, this approach enabled preparation of glasses with smectic order ranging from strong to none.^{5, 6}

Similarly, for the discotic LC phenanthro[1,2,3,4-ghi]perylene-1,6,7,12,13,16-hexacarboxylic 6,7,12,13-tetraethyl,1,16-dimethyl ester (PNP, Scheme 1), it is possible to prepare glasses with strong and zero columnar order. In both cases, the amount of LC order in the glass is determined by the kinetic arrest of a slow relaxation mode (end-over-end rotation for rods and heads-over-tails flip for discs). This relaxation mode is frozen at a higher temperature than the other degrees of freedom, producing a glass with multiple internal (fictive) temperatures for its different structural features. Given the common occurrence of multiple relaxation modes in calamitic 6,8,10,11 and discotic LCs,7,12-16 this phenomenon may have general relevance for understanding the structures of their glasses.



Scheme 1. Molecular structure of PNP (top) and the two mesoscopic orders (columnar and π stacking) studied here (bottom).

In this work, we investigate the glass structures of the discotic LC (DLC) former PNP with particular attention to the p stacking order and its dependence on glass-forming conditions.

DLCs have attracted attention for their potential applications in organic electronics. ¹⁷⁻²⁰ The system studied here, PNP, has been synthesized to have a glassy columnar LC phase at room temperature for electronic applications. ²¹ Chen *et al.* have investigated the effect of cooling rate on the columnar order of a PNP glass, ⁷ and we focus here on the π stacking order and its relation to the columnar order. As illustrated in Scheme 1, the columnar order refers to the organization of the discotic molecules into regularly arranged columns and the π stacking order to the regular face-to-face contact of the aromatic cores. The π stacking order is of interest because DLCs can provide enhanced conductance along the columnar axis²² and improved overlap of the π orbitals can improve conductance. ^{19, 23}

An interesting question concerning glass-forming LCs is the nature of their glass transition. Given the common description of a LC as having crystal-like order in some dimensions and liquid-like order in others, will a glass transition influence the two dimensions differently? For a triphenylene-based DLC, the intercolumnar spacing is less affected by the glass transition than the intracolumnar spacing,²⁴ but for the calamitic LC itraconazole⁹ and saperconazole,⁶ the glass transition has strong influence on both the structure of the smectic layers and the packing within each layer. This question is relevant for understanding the glass structures of LCs and will be investigated for PNP.

We find that by varying the cooling rate, PNP glasses can be prepared with widely different π stacking order and columnar order, including zero order. In the equilibrium liquid state, the intensities of the scattering peaks for π stacking and for columnar packing are proportional to each other, indicating concurrent development of the two orders. On entering the glassy state, the π stacking distance undergoes kinetic arrest with a 3-fold reduction of the thermal expansion coefficient (TEC), while the TEC associated with intercolumnar spacing remains constant. Upon

cooling, the columnar order and the π stacking order are frozen at the kinetic arrest temperature of the δ relaxation mode (disc tumbling), while the π stacking distance and enthalpy freeze at the kinetic arrest temperature of the α relaxation (rotation about the column axis). We discuss the relevance of our result for controlling the structural features of a glass to optimize its properties.

5.3 Experimental Section

Materials and Sample Preparation. Phenanthro[1,2,3,4-ghi]perylene-1,6,7,12,13,16-hexacarboxylic 6,7,12,13-tetraethyl1,16-dimethyl ester (PNP) was synthesized using the procedure of Kelber *et al.*²¹ Crystalline PNP powder was filled into an X-ray transmitting capillary tube (Charles Supper, MA, 1.5 mm OD, 10 μm wall thickness) and melted before flame sealing the tube. A glass sample was prepared by heating the sample above the LC clearing temperature (519 K) and cooling the isotropic liquid at a controlled rate (*R*_c). Slower cooling was performed by programed cooling in a DSC cell and faster cooling by cooling a sample preheated to 550 K in ambient air or in an ice-water bath. In the latter case, the cooling rate was measured by performing the same cooling procedure with a thermocouple coated with a 1.5 mm layer of epoxy to mimic the thermal conductivity of the sample.

X-Ray Scattering. X-ray scattering was measured with a Bruker D8 Discover diffractometer equipped with a Cu K α source (λ = 1.5406 Å), a Vantec 500 area detector, and an Instec mK2000 heating stage. Temperature was calibrated using the melting points of crystals (Benzamide, 401 K; D-mannitol Form b, 439 K; Griseofulvin Form I, 493 K) and PNP's clearing temperature (519 K). The sample in a capillary tube was irradiated perpendicularly and the scattered X-ray was measured in the transmission geometry. The area detector was placed off-center at $2\theta = 20^{\circ}$ and 20 cm from the sample to allow coverage of the q (= $4\pi \sin \theta/\lambda$) range from

0.3 to 2.1 Å⁻¹ and simultaneous measurement of the columnar and the π - π scattering. Griseofulvin Form I and silver behenate were used to calibrate the diffraction angle and to determine the instrumental resolution. Each glass sample was measured during heating and after reaching the liquid state, measured during cooling. At each measurement temperature, the sample was equilibrated for 5 min and measured for 5 min. The two-dimensional X-ray scattering data was integrated using the software Datasqueeze²⁵ to yield a one dimensional intensity vs q plot.

Differential Scanning Calorimetry (DSC). A TA Q2000 Differential Scanning Calorimeter was used to measure the relative enthalpies of different glasses. Each sample (3–5 mg) was placed in a crimped aluminum pan and analyzed under 50 mL/min N₂ purge. For each measurement, the sample was cooled at a controlled rate (1–30 K/min) from 538 K (isotropic state) to 303 K (glassy state) and heated at 10 K/min to 538 K.

5.4 Results and Discussion

shows the typical X-ray scattering data collected during cooling from an isotropic liquid of PNP. The instrument setup allowed simultaneous measurement of the columnar scattering peak and the π - π scattering peak; see a typical 2D scattering image in the inset where the two peaks are labeled c and π . The 2D scattering pattern consists of concentric rings, indicating no preferred orientation of LC domains. Azimuthal integration of the 2D pattern yielded the intensity vs. q curves in the main figure, where q is the magnitude of the momentum transfer.

With cooling below the isotropic-columnar transition temperature ($T_c = 519$ K), peaks emerge at $q_c = 0.41$ Å⁻¹ and $q_\pi = 1.8$ Å⁻¹. The peak at q_c results from the scattering by the regularly arranged columns²¹ and the peak at q_π from the regular stacking of the aromatic cores (π stacking);^{26,27} see Scheme 1. From these peak positions we obtain $d_c = 2\pi/q_c = 15.4$ Å for the intercolumnar distance and $d_\pi = 2\pi/q_\pi = 3.5$ Å for the π - π stacking distance. In addition to these two peaks, a broad peak is observed to the left of the π stacking peak near 1.5 Å⁻¹ and attributed to the correlation of the side chains attached to the aromatic core.²⁶ Figure 1 shows that with cooling below T_c , the columnar peak and the π stacking peak grow simultaneously, indicating that the two structural orders increase together. Furthermore, the π stacking peak is significantly

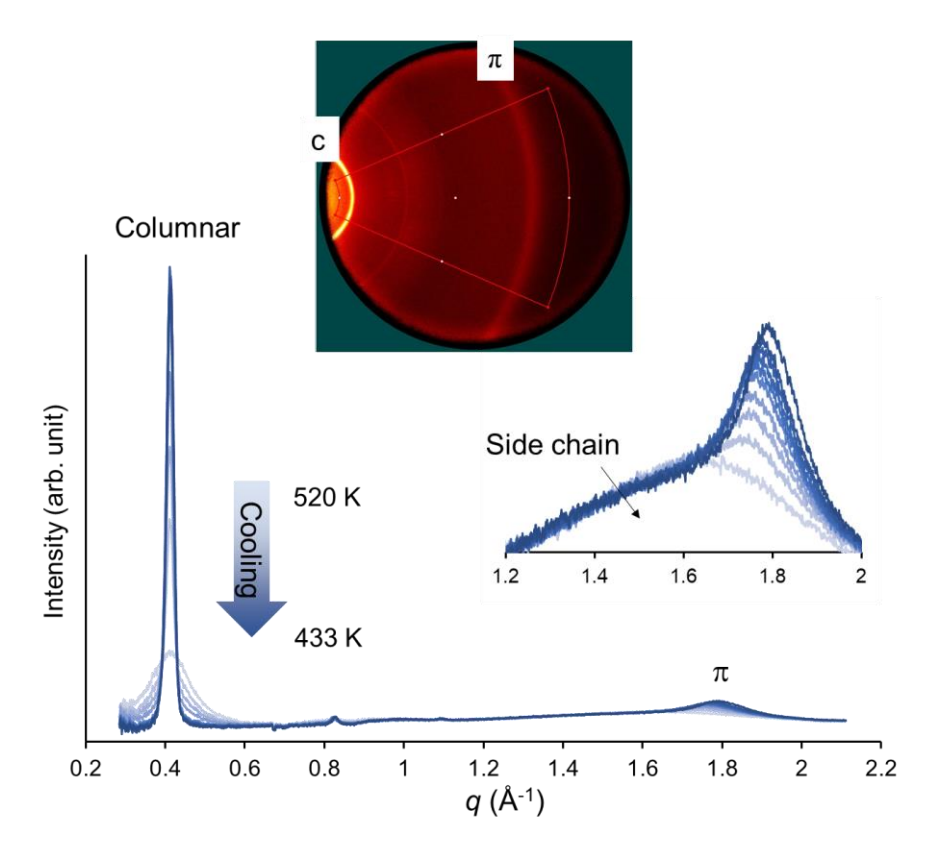


Figure 1. X-ray scattering curves of PNP measured during cooling from the isotropic liquid state. The 0.41 Å⁻¹ peak results from intercolumnar scattering, the 1.8 Å⁻¹ peak from π - π scattering, and the broad feature near 1.5 Å⁻¹ from the correlation between the side chains of the aromatic core. Insets: a typical 2D scattering pattern and an enlarged view of the π scattering peak.

broader than the columnar peak, indicating a shorter correlation length. Below we analyze these results quantitatively with aid of curve fitting.

An X-ray scattering peak provides information on the underlying molecular packing giving rise to the peak: the average atomic spacing from the peak position ($d = 2\pi/q$), the correlation length from the peak width, and the correlation strength (number of correlated atoms) from the peak area. To obtain these parameters, peaking fitting was performed to isolate each scattering peak. As shown in Figure 2, the signal near 0.41 Å⁻¹ is well described as a sum of a sharp Gaussian and a broad Lorentzian.⁷ The broader Lorentzian results from the excluded volume effect²⁸ where

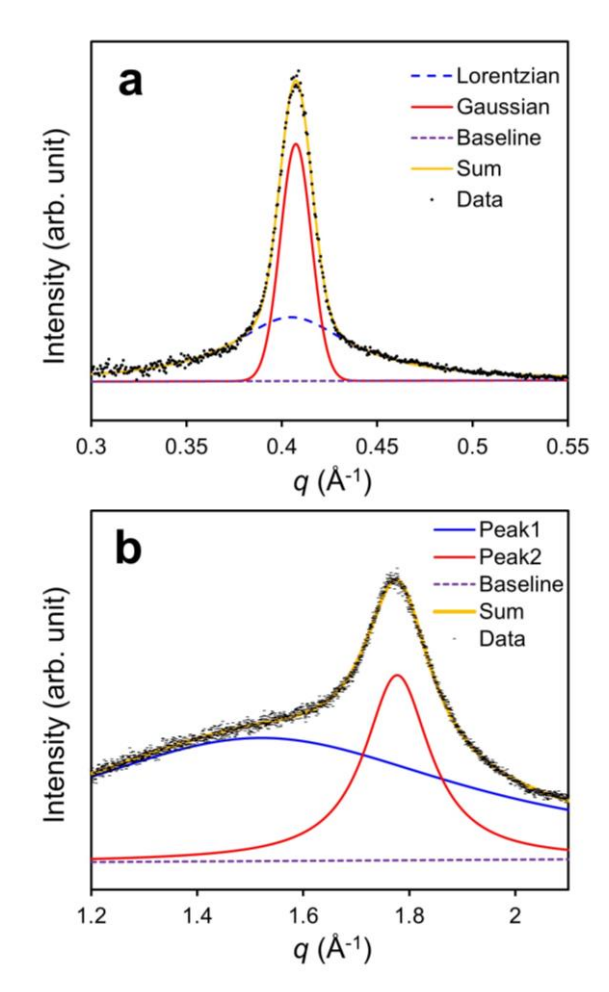


Figure 2. Fitting of (a) the columnar peak and (b) the π stacking peak.

each molecule orders its neighbors through its disc-like shape even in the isotropic liquid state ($T > T_c$) and the sharper Gaussian is used to quantify the columnar order in the LC phase.²⁹ Figure 2b shows that the signal near 1.8 Å⁻¹ is well described as a sum of two Lorentzians, with the broader component at 1.5 Å⁻¹ describing the correlation of the side chains of the aromatic cores and the sharp component at 1.8 Å⁻¹ the π stacking order.^{26,27}

Figures 3, 4, and 5 present the positions, the widths, and the areas of the columnar and p scattering peaks as functions of temperature. As shown in Figure 3a, on cooling below the clearing temperature T_c , the columnar peak position q_c increases almost linearly with temperature with a nearly constant TEC, α_c = 113 ppm/K, in good agreement with Chen et al.'s value of 117 ppm/K.⁷ The temperature range studied spans the glass transition temperature $T_{\rm g}$ detected by DSC (393 K) and $q_{\rm c}$ is insensitive to the passage through $T_{\rm g}$. The second y axis in Figure 3a shows the intercolumnar spacing, $d_c = 2\pi/q_c$, which decreases with cooling from 15.4 Å to 15.1 Å in the temperature range studied. In contrast to the temperature dependence of q_c , the π stacking peak position q_{π} is sensitive to the

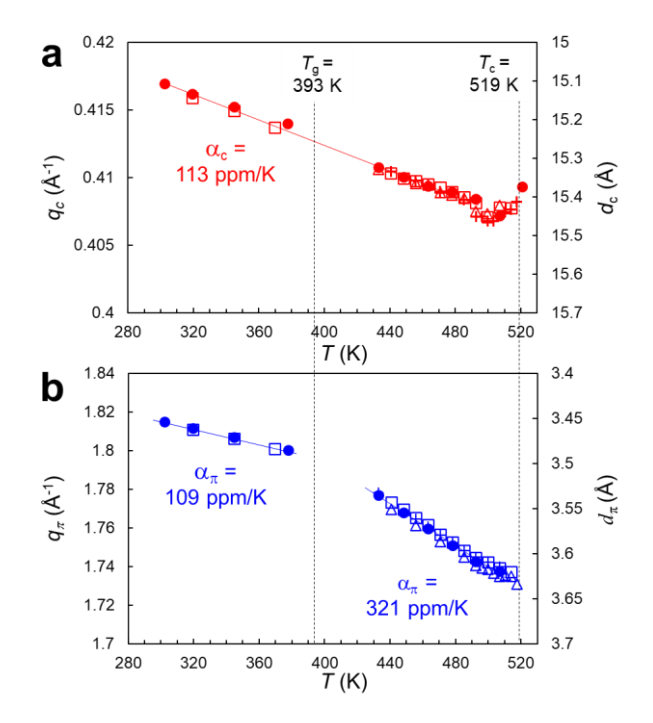


Figure 3. Temperature dependence of the positions of (a) the columnar peak q_c and (b) the π stacking peak q_π during cooling from the isotropic liquid state. The different symbols indicate different datasets. q_c is insensitive to the passage through T_g (393 K), but q_π is. The range 393 – 420 K was bypassed due to crystallization. a_c and a_π are the thermal expansion coefficients (TECs) for the intercolumnar spacing and the π - π spacing, respectively.

passage through T_g : its TEC decreases from $\alpha_{\pi} = 321$ ppm/K above T_g to $\alpha_{\pi} = 107$ ppm/K below, a drop by a factor of 3. From α_c and α_{π} , the volumetric TEC can be calculated, $\alpha_v = 2\alpha_c + \alpha_{\pi}$, yielding $\alpha_v = 547$ ppm/K above T_g and 333 ppm/K below. A change of TEC across T_g is a hallmark of a liquid's glass transition. ^{30, 31} PNP's TECs indicate that its glass transition is associated mainly with the intracolumnar structure, not the intercolumnar spacing. During cooling, the system is

crystal-like throughout the glass transition with respect to d_c but shows a glass transition in d_π . This behavior is analogous to that of a triphenylene-based DLC²⁴ where α_c decreases linearly with cooling through T_g , while α_π shows a steplike drop at T_g . This result is sensible in reference to the common view that a columnar LC has crystal-like intercolumnar packing and liquid-like intracolumnar packing, but is in contrast to the behavior of the calamitic LC itraconazole⁹ for which the glass transition influences the TECs of both the spacing between smectic layers and the distance between molecules within a layer.⁹ The literature on DLCs shows diverse thermal expansion behaviors with the α_c values ranging from positive^{24, 32} to negative²⁶ and from being larger in amplitude than α_π^{32} to smaller.²⁴ Relative to this range, the thermal expansion of PNP is not exceptional.

Figure 4 shows the full widths at half maximum (FWHM) of the columnar peak and the π stacking peak as functions of temperature. The columnar peak is much sharper than the π

stacking peak and in fact, is limited by the instrumental resolution (FWHM = 0.016 Å^{-1} , obtained by Gaussian fitting of crystalline peaks and shown in Figure 4 as the horizontal line). The width of the \square stacking peak, in contrast, exceeds the instrumental resolution, allowing calculation of its correlation length ξ . A Lorentzian scattering peak corresponds in real

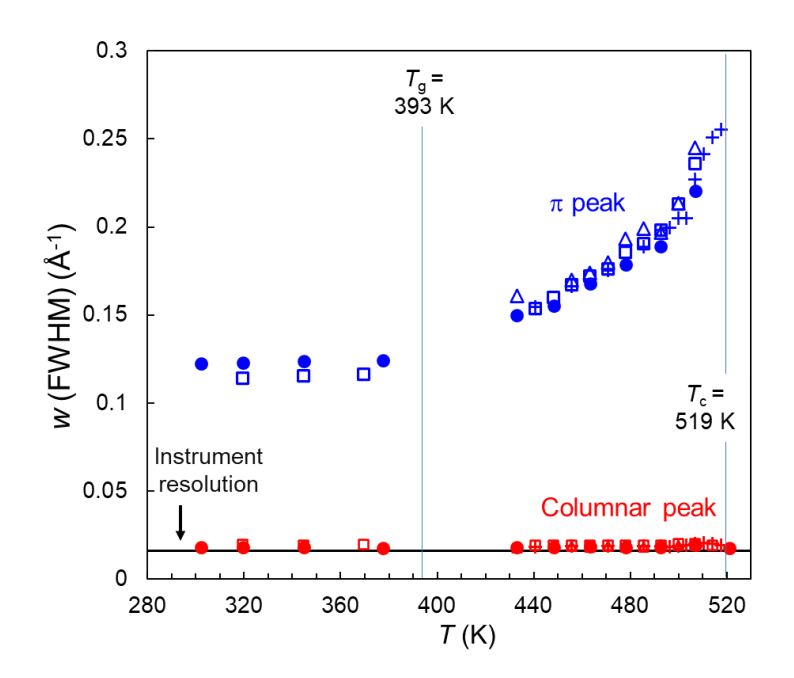


Figure 4. Widths (FWHM) of the columnar peak and the π stacking peak vs. temperature during cooling from the isotropic liquid.

space to an exponentially damped sinusoidal pair-correlation function with a decay length of $\xi = 2$ /FWHM.⁹ Upon cooling from T_c , the FWHM of the π stacking peak decreases from 0.25 Å⁻¹ to 0.12 Å⁻¹ near and below T_g ; this translates to a doubling of the correlation length from 8 Å to 17 Å (2 to 5 discs). Below T_g , ξ is insensitive to temperature, as expected. These correlation lengths are relatively short, only slightly longer than that for the non-mesogen glycerol near T_g , $\xi \approx 8$ Å.³⁰ The short correlation length for PNP's intracolumnar structure is consistent with a confined, one-dimensional liquid that exhibits a glass transition (Figure 3b). For a hexa-*peri*-hexabenzocoronene (HBC)-based DLC, Hansen *et al.*¹³ observed similarly short intracolumnar correlation length (24 Å or 7 discs) and associated it with a heterogeneous columnar structure containing segments of well-packed discs separated by disordered regions. It would be of interest to learn if PNP has a similar or a different structure.

Figure 5a shows the temperature dependence of the areas of the columnar peak A_c and the π stacking peak A_π . Both A_c and A_π rise sharply with cooling below T_c and evolve more slowly below 480 K. Below 480 K, A_c appears to decrease slightly, while A_π appears to increase slightly. In Figure 5b, the two areas are plotted against each other, and we observe an approximately proportional relation, indicating that the two types of order grow roughly in proportion. This result is sensible since better organized, tightly packed columns are expected to organize the discs within each column. It is unclear why the two orders evolve somewhat differently below 480 K. Given that each scattering peak is isolated by curve fitting from an overlapping peak (Figure 2), model accuracy plays a role. This effect, if real, could reflect the different responses of the inter- and intracolumnar structures to the glass transition (Figure 3): while the intercolumnar spacing shows no kinetic arrest, the π - π spacing does. Thus, during cooling below T_g , the intracolumnar structure could exhibit a slight glass aging effect (evolving toward equilibrium), while the intercolumnar

structure might not. The calamitic LC itraconazole shows a slight decrease of smectic order with cooling in the glassy state,⁵ which was related to the tension that developed in the glass due to the mismatch of the thermal expansion coefficients of itraconazole and its container.

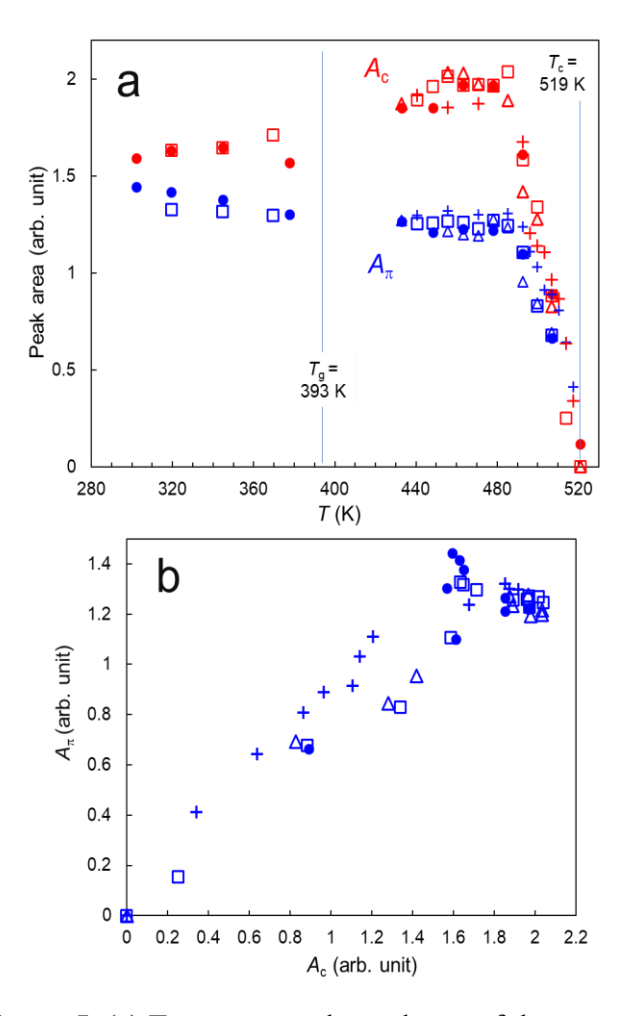


Figure 5. (a) Temperature dependence of the areas of the columnar peak A_c and the π stacking peak A_{π} during cooling from the isotropic liquid state. The different symbols correspond to different datasets. The two orders rise together below T_c and stabilize near 480 K. (b) A_{π} is approximately proportional to A_c , suggesting two orders are coupled.

Structures of PNP Glasses Prepared at Different Cooling Rates. We now turn to the effect of cooling rate on the different structural features of a PNP glass. Figure 6 shows the X-ray scattering patterns of PNP glasses prepared by cooling at different rates. The glass prepared at the lowest cooling rate (0.5 K/s) had the highest columnar order and the π stacking order, while faster cooling

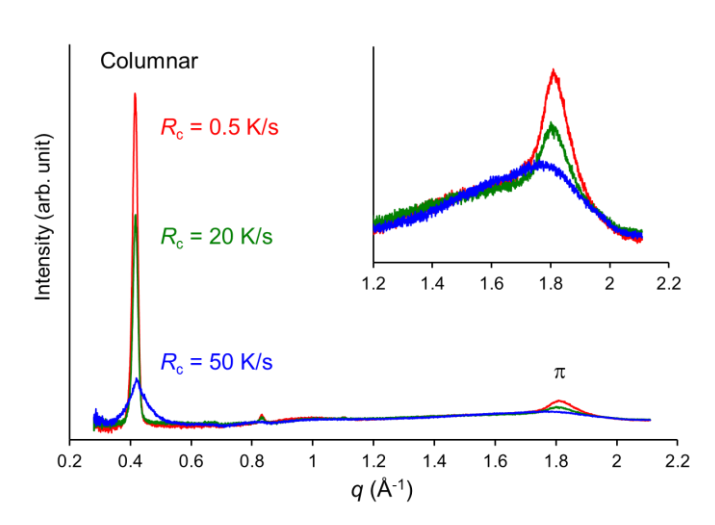


Figure 6. X-ray scattering patterns of PNP glasses prepared by cooling at different rates and measured at 298 K.

reduced both orders in the glass. Given the two orders are strongly correlated in the equilibrium liquid state (Figure 5b), it is not surprising to observe this qualitative result. But as we show below by quantitative analysis, the two orders show significant decoupling that is relevant for controlling the p stacking in the glassy state.

To quantify the structure of a glass, we adopt the standard measure of fictive temperature $T_{\rm f}$. For a liquid in equilibrium, $T_{\rm f}$ is equal to the actual temperature; for an out-of-equilibrium glass, $T_{\rm f}$ is higher than the actual temperature, corresponding to an equilibrium liquid that would display the same structural feature (e.g., enthalpy and volume) aside from the thermal-expansion effect. Figure 7 illustrates the determination of $T_{\rm f}$ for two structural features in a single PNP glass, 9 namely, the π - π spacing d_{π} (= $2\pi/q_{\rm p}$) and the p stacking order measured by the π scattering peak area $A_{\rm p}$. This glass was prepared by cooling at 20 K/s and its X-ray scattering was measured during heating from the glassy state to the liquid state (open symbols). The solid symbols indicate the equilibrium liquid behavior observed during cooling from the isotropic state (Figures 3 and 5). Figure 7a shows

that as the glass was heated, d_{π} increases linearly in the glassy state $(T \le T_g)$ and on entering the liquid state $(T > T_g)$, increases at a faster rate. A difficulty in this measurement is that above T_g , the sample crystallized from the nuclei formed at low temperature, causing a gap in the data, and the measurement could resume only after the crystals melted near 490 K. (Crystallization was less of a problem when cooling a liquid from high temperature.) Nevertheless, the glassy-state and the liquid-state data can be combined to obtain the fictive temperature $T_{\rm f}$ (Figure 7a) at the intersection of the glass line and the liquid line. For this glass, $T_f = 405$ K with respect to d_{π} . In Figure 7b, a similar procedure is used to determine the $T_{\rm f}$ with respect to the peak area A_{π} , yielding $T_{\rm f} = 509$ K. Thus, for this glass, the T_f for A_{π} is much higher than that for d_{π} , by more than 100 K. These two structural

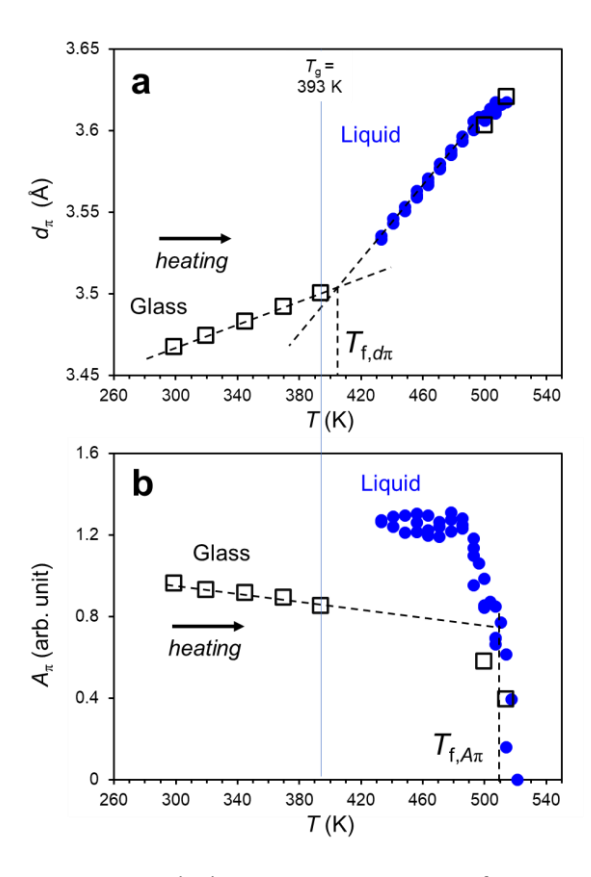


Figure 7. Fictive temperature T_f of a PNP glass with respect to two features of π stacking: (a) π - π spacing d_{π} and (b) area of the scattering peak A_{π} . The glass was prepared by cooling at 20 K/s and measured during heating (open square). T_f is the intersection of the glass line and the liquid line (solid symbols).

features both characterize the π stacking in a PNP glass but its different aspects, namely, the molecular spacing (d_{π}) and the number of correlated molecules (A_p) . The large difference between the two fictive temperatures indicates that during cooling, the two structural features are frozen at very different temperatures.

In Figure 8, we plot the fictive temperatures T_f of a PNP glass against the cooling rate R_c used to prepare the glass. The fictive temperatures have been measured with respect to different structural features, including the π - π distance d_{π} and the π stacking order $A_{\rm p}$ used in this work (Figure 7) and the enthalpy H and the columnar order A_c used by Chen et al.7 These results are displayed in the upper half of the figure (solid symbols, +, and x) with the cooling rate R_c shown on the right y axis. allows This plotting

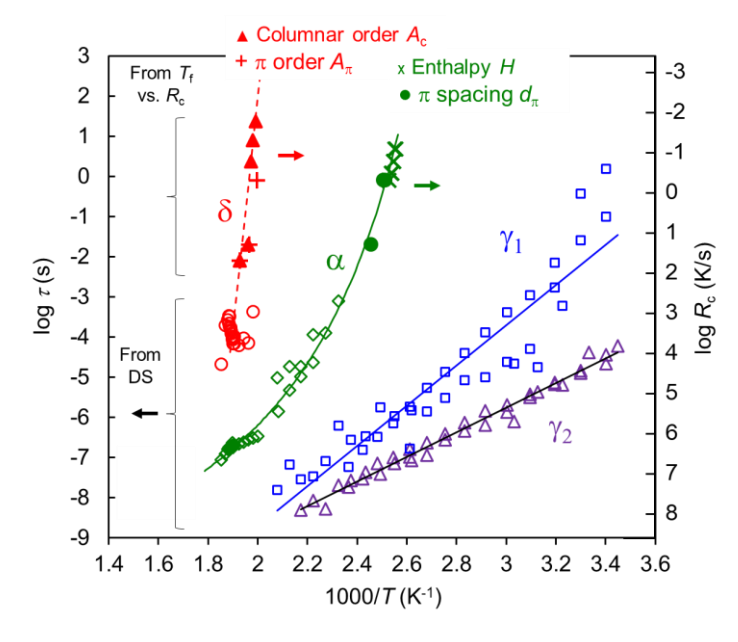


Figure 8. Relaxation map of PNP. Relaxation times from DS (open symbols) are plotted using the left y axis. $T_{\rm f}$ vs. cooling rate $R_{\rm c}$ results are plotted using the right y axis. The properties undergoing kinetic arrest are enthalpy (x),⁷ columnar order $A_{\rm c}(\triangle)$,⁷ π spacing d_{π} (•), and π stacking order A_{π} (+). The two y axes are related by $\tau R_{\rm c} = C = 0.4$ K.⁷

comparison of these results with the relaxation times from dielectric spectroscopy (DS) reported previously. Figure 8 shows that the different structural features of a PNP glass fall in two groups in terms of their fictive temperatures: H and d_{π} in one group with lower $T_{\rm f}$ and $A_{\rm c}$ and A_{π} in the other group with higher $T_{\rm f}$. These two groups of structural features differ in that H and d_{π} are controlled mainly by the nearest-neighbor correlations, whereas $A_{\rm c}$ and A_{π} by the correlations of a larger group of molecules. Since the rearrangement of the nearest neighbors is expected to be faster than that of a larger group of molecules, it is sensible that H and d_{π} can remain equilibrated during cooling down to a lower temperature than $A_{\rm c}$ and A_{π} , leading to their different fictive temperatures. Given that $A_{\rm c}$ and A_{π} are strongly coupled in the equilibrium liquid state (Figure 5), it is not

surprising that both are frozen at similar temperatures and have similar $T_{\rm f}$ values. An analogous grouping of properties has been observed in the vitrification of the smectic LC itraconazole. In this case, the smectic order and the correlation length of the intralayer packing are frozen together at a higher temperature, while the enthalpy, the interlayer spacing, and the intralayer spacing freeze together at a lower temperature.

The format of Figure 8 allows comparison of the relaxation times of PNP from DS with those from the kinetic arrest of structural features. The DS-derived relaxation times are shown as open symbols using the left y axis. The two y axes are related by $\tau R_c = C = 0.4$ K, the condition of kinetic arrest obtained previously. PNP has 4 relaxation modes: α , δ , γ_1 , and γ_2 . The α mode is associated with the molecular motions that are kinetically frozen at the DSC $T_{\rm g}$. Relative to α , the δ mode is slower and the γ_1 and γ_2 modes faster. The a mode has been assigned to disc rotation about its axis, the δ mode to the disc tumbling within a column, and the γ_1 and γ_2 modes to side chain fluctuations.^{7,12} Figure 8 shows that the kinetic arrest of the different structural features of a PNP glass are associated with the different relaxation modes. The enthalpy H and the π - π spacing d_{π} are associated with the α mode, whereas the columnar order $A_{\rm c}$ and the π stacking order A_{π} are associated with the slower δ mode.⁷ This result on PNP echoes the previous result on itraconazole where enthalpy and nearest-neighbor spacing are frozen by the kinetic arrest of the α relaxation and the regularity of molecular packing is frozen by the kinetic arrest of the δ relaxation. The association of enthalpy fluctuation with the α relaxation has been observed in molecular liquids without³³ and with LC order.^{5-7, 9}

Improving π Stacking Order in the Glassy State. Given the importance of π -orbital overlap in charge mobility, ^{19, 23} we consider how the p stacking order can be improved in the glass of a DLC. To maximize charge transport, an ideal structure should have a short π - π distance d_{π} and

a long correlation length ξ . According to this work, such a structure should be prepared at a relatively slow cooling rate. Figure 6 shows that the PNP glass prepared at the fastest cooling rate is devoid of any π stacking peak. This is because the molecular motion that controls the development of π stacking (disc tumbling) can be frozen at a high temperature (Figure 8). In addition, Figures 3 and 5 show that during cooling, d_{π} steadily decreases and ξ increases until $T_{\rm g}$ is reached. This suggests that the most efficient way to improve p stacking is slow cooling through the glass transition region. Slow cooling well above $T_{\rm g}$ is unnecessary since equilibration is fast; slow cooling well below $T_{\rm g}$ is unproductive since mobility is slow. Apart from slow cooling through $T_{\rm g}$, isothermal aging slightly below $T_{\rm g}$ could improve π stacking. Based on the result in Figure 3, we expect such aging to reduce d_{π} , but to have little effect on $d_{\rm c}$ (intercolumnar spacing).

Connection to Vapor-Deposited Glasses. The results presented here provide insight into recent experiments in which glasses of PNP were prepared by vapor-deposition. Bishop *et al.* vapor-deposited PNP glasses at a number of different substrate temperatures and deposition rates, and characterized these materials by X-ray scattering and ellipsometry.³⁴ At low substrate temperatures or high deposition rates, PNP molecules tended towards "face-on" orientation relative to the substrate. At high substrate temperatures or low deposition rates, PNP molecules had an "edge-on" orientation and formed hexagonally packed columns that propagate primarily in the plane of the substrate. Bishop *et al.* found that the vapor-deposited PNP glasses had different d_p values but that the results could be rationalized by assuming that the surface relaxation process that governs this structure formation slowed by one decade for every 17 K decrease of temperature. Similarly, they reported that the vapor-deposited glasses had different levels of columnar order (in Figure 4 of ref. 22), and that this structural feature could be rationalized with a relaxation process that slowed one decade for every 9 K.³⁴

There is a striking parallel between the results presented here and those of Bishop *et al.* ³⁴ In each case, structural order connected with the π stacking distance has a weaker temperature dependence than structural order associated with columnar order. It is reasonable that this correspondence should exist, since faster processes are generally more localized, and more localized relaxation would be expected to be faster whether in the bulk (as in the present work) or at a free surface (as in the work of Bishop *et al.*). Based upon this result, we offer the following speculation: If the measures of structural order for the vapor-deposited glasses of a given molecule all show the same temperature dependence (such as the organic semiconductor ABH113³⁵), then we expect that only a single T_f value will be observed for glasses formed by cooling.

Which Aspect of LC Structure Is Influenced by the Glass Transition? A common description of a LC structure is crystal-like order in some dimensions but liquid-like order in others. For a DLC, this view envisions a crystal-like packing of the columns but a liquid-like packing within a column (Scheme 1). Reasoning from this view, one would expect that the glass transition to influence the intracolumnar structure but not the intercolumnar structure. This view is consistent with the DLC of this work (Figure 3) and the DLC of Möller *et al.*²⁴ Both systems show a discontinuous drop of TEC for the p-p spacing upon cooling through T_g while the glass transition has less influence on the TEC for intercolumnar spacing. These systems are in contrast, however, to the smectic LC itraconazole.⁹ A smectic LC has regular, crystal-like layers that produce sharp X-ray scattering, while its intralayer structure is liquid-like and produces diffuse scattering.³⁶ In this case, one might expect the glass transition to influence the intralayer structure but not the interlayer packing. But for itraconazole, both inter- and intralayer spacings are strongly influenced by the glass transition.⁹ It is possible that the different behaviors arise from the different types of liquid crystallinity: 2D hexagonal packing of the columns in the two DLCs vs 1D stacking of layers

in itraconazole. For itraconazole, the TEC for the smectic layer spacing is anomalously large (932 ppm/K), suggesting an interdigitation of layers, which would promote a joint response of the interand intralayer structures to the glass transition.

5.5 Conclusions

We have characterized the structures of the equilibrium liquid of the discotic LC PNP and its glasses prepared by cooling at different rates. Attention is paid to the π stacking order because of its importance in charge mobility and device performance. In the equilibrium liquid state, the thermal expansion coefficient (TEC) for the π - π spacing is approximately 3 times that for the columnar spacing and in the glassy state, the two TECs are comparable. The TEC of the columnar spacing is insensitive to the passage through T_g , whereas the TEC of the π - π spacing decreases by a factor of 3 from above to below $T_{\rm g}$. These results suggest the picture of a "one-dimensional liquid" in which the intercolumnar packing is solid-like and the intracolumnar structure is liquid-like (Figure 3). On cooling below the clearing temperature T_c , the π stacking order (measured by the scattering peak area) grows almost in proportion with the columnar order, reaching a plateau together (Figure 5). By cooling at different rates, glasses can be prepared in which the structural features examined vary significantly (Figure 6). Each glass is characterized by not one, but two fictive temperatures (Figures 7 and 8), with the higher value associated with the columnar order and the π stacking order and the lower value with the enthalpy and the π - π spacing. This is a consequence of the multiple relaxation modes of PNP (Figure 8) with the kinetic arrest of the slow δ relaxation mode defining the columnar and the π stacking order and that of the fast a relaxation mode defining the enthalpy and the π - π spacing.

The finding of this work reinforces the previous conclusion that different aspects of a glass structure can be controlled through the kinetic arrest of the different relaxation modes. This result was first demonstrated with calamitic LCs, and this work extends it to a discotic mesogen. In both cases, the existence of multiple and widely separated relaxation modes leads to the freezing of structural features in separate groups. In both cases, the non-spherical geometry of the molecule is the origin for the different timescales of molecular rotations. The similarity of rod-like and discotic mesogens in this regard suggests a general principle for glass engineering. To optimize a targeted structural feature (e.g., π stacking) in a glass, a processing path should be based on the relaxation mode controlling that feature (Figure 8). For example, to optimize p stacking in PNP, cooling must be slow enough through the T_g of the δ mode, which is well above the conventional T_g of the α mode; otherwise the order may fail to develop. Meanwhile, slow cooling through the conventional T_g helps reduce the π - π spacing (Figure 3) and increase its correlation length (Figure 4).

The state of a glass is often mapped to the equilibrium liquid phase using a fictive temperature T_f . The difference between T_f and the actual temperature is used to indicate how much the glass has fallen out of equilibrium relative to the liquid phase and to model how fast it evolves toward it.³⁷ In applying this concept, each glass is usually understood as having a single T_f . The glass-forming LCs PNP, itraconazole,⁹ and saperconazole⁶ illustrate the possibility that one glass can have multiple and very different T_f values. The origin for this phenomenon is the existence of multiple relaxation modes, whose kinetic arrests occur at different temperatures and freeze different aspects of structure. In principle, the phenomenon can occur for any liquid with multiple relaxation modes. A glass with multiple fictive temperatures has a combination of structural features that is unlike the equilibrium liquid at any temperature. How such a glass evolves toward equilibrium during aging is an interesting question.

5.6 Acknowledgements

We thank the NSF (DMR-1904601) for supporting this work and the NSF-supported University of Wisconsin Materials Research Science and Engineering Center (DMR-1720415) for use of its characterization facility.

5.7 References

- (1) Tsuji, K.; Sorai, M.; Seki, S. New finding of glassy liquid crystal—A non-equilibrium state of cholesteryl hydrogen phthalate. Bulletin of the Chemical Society of Japan 1971, 44 (5), 1452-1452.
- (2) Wedler, W.; Demus, D.; Zaschke, H.; Mohr, K.; Schäfer, W.; Weissflog, W. Vitrification in low-molecular-weight mesogenic compounds. Journal of Materials Chemistry 1991, 1 (3), 347-356.
- (3) Attard, G.; Imrie, C.; Karasz, F. Low molar mass liquid-crystalline glasses: preparation and properties of the. alpha.-(4-cyanobiphenyl-4'-oxy)-. omega.-(1-pyreniminebenzylidene-4'-oxy) alkanes. Chemistry of materials 1992, 4 (6), 1246-1253.
- (4) Chen, S.; Katsis, D.; Schmid, A.; Mastrangelo, J.; Tsutsui, T.; Blanton, T. Circularly polarized light generated by photoexcitation of luminophores in glassy liquid-crystal films. Nature 1999, 397 (6719), 506-508.
- (5) Teerakapibal, R.; Huang, C.; Gujral, A.; Ediger, M. D.; Yu, L. Organic glasses with tunable liquid-crystalline order. Physical review letters 2018, 120 (5), 055502.
- (6) Chen, Z.; Yu, J.; Teerakapibal, R.; Meerpoel, L.; Richert, R.; Yu, L. Organic glasses with tunable liquid-crystalline order through kinetic arrest of end-over-end rotation: the case of saperconazole. Soft Matter 2020, 16 (8), 2025-2030.

- (7) Chen, Z.; Bishop, C.; Thoms, E.; Bock, H.; Ediger, M. D.; Richert, R.; Yu, L. Controlling the Columnar Order in a Discotic Liquid Crystal by Kinetic Arrest of Disc Tumbling. Chemistry of Materials 2021, 33 (12), 4757-4764.
- (8) Tarnacka, M.; Adrjanowicz, K.; Kaminska, E.; Kaminski, K.; Grzybowska, K.; Kolodziejczyk, K.; Wlodarczyk, P.; Hawelek, L.; Garbacz, G.; Kocot, A. Molecular dynamics of itraconazole at ambient and high pressure. Physical Chemistry Chemical Physics 2013, 15 (47), 20742-20752.
- (9) Yu, J.; Chen, Z.; Teerakapibal, R.; Benmore, C.; Richert, R.; Yu, L. Structures of glasses created by multiple kinetic arrests. The Journal of Chemical Physics 2022, 156 (8), 084504.
- (10) Schönhals, A.; Zubowa, H. L.; Fricke, R.; Frunza, S.; Frunza, L.; Moldovan, R. On the Dielectric Behavior of Unaligned Samples of 4-n-Octyl-4'-cyanobiphenyl (8CB). Crystal Research and Technology: Journal of Experimental and Industrial Crystallography 1999, 34 (10), 1309-1314.
- (11) Brás, A.; Dionísio, M.; Huth, H.; Schick, C.; Schönhals, A. Origin of glassy dynamics in a liquid crystal studied by broadband dielectric and specific heat spectroscopy. Physical Review E 2007, 75 (6), 061708.
- (12) Elmahdy, M.; Floudas, G.; Mondeshki, M.; Spiess, H. W.; Dou, X.; Müllen, K. Origin of the complex molecular dynamics in functionalized discotic liquid crystals. Physical review letters 2008, 100 (10), 107801.
- (13) Hansen, M.; Feng, X.; Macho, V.; Müllen, K.; Spiess, H. W.; Floudas, G. Fast and slow dynamics in a discotic liquid crystal with regions of columnar order and disorder. Physical Review Letters 2011, 107 (25), 257801.

- (14) Yildirim, A.; Kolmangadi, M. A.; Bühlmeyer, A.; Huber, P.; Laschat, S.; Schönhals, A. Electrical conductivity and multiple glassy dynamics of crown ether-based columnar liquid crystals. The journal of physical chemistry B 2020, 124 (39), 8728-8739.
- (15) Yildirim, A.; Krause, C.; Zorn, R.; Lohstroh, W.; Schneider, G. J.; Zamponi, M.; Holderer, O.; Frick, B.; Schönhals, A. Complex molecular dynamics of a symmetric model discotic liquid crystal revealed by broadband dielectric, thermal and neutron spectroscopy. Soft matter 2020, 16 (8), 2005-2016.
- (16) Yildirim, A.; Krause, C.; Huber, P.; Schönhals, A. Multiple glassy dynamics of a homologous series of triphenylene-based columnar liquid crystals—A study by broadband dielectric spectroscopy and advanced calorimetry. Journal of Molecular Liquids 2022, 358, 119212.
- (17) Feng, X.; Marcon, V.; Pisula, W.; Hansen, M. R.; Kirkpatrick, J.; Grozema, F.; Andrienko, D.; Kremer, K.; Müllen, K. Towards high charge-carrier mobilities by rational design of the shape and periphery of discotics. Nature materials 2009, 8 (5), 421-426.
- (18) Pisula, W.; Zorn, M.; Chang, J. Y.; Müllen, K.; Zentel, R. Liquid crystalline ordering and charge transport in semiconducting materials. Macromolecular rapid communications 2009, 30 (14), 1179-1202.
- (19) Kaafarani, B. R. Discotic liquid crystals for opto-electronic applications. Chemistry of Materials 2011, 23 (3), 378-396.
- (20) O'Neill, M.; Kelly, S. M. Ordered materials for organic electronics and photonics. Advanced Materials 2011, 23 (5), 566-584.
- (21) Kelber, J.; Achard, M. F.; Durola, F.; Bock, H. Distorted Arene Core Allows Room-Temperature Columnar Liquid-Crystal Glass with Minimal Side Chains. Angewandte Chemie International Edition 2012, 51 (21), 5200-5203.

- (22) Boden, N.; Bushby, R.; Clements, J. Electron transport along molecular stacks in discotic liquid crystals. Journal of Materials Science: Materials in Electronics 1994, 5, 83-88.
- (23) García-Frutos, E. M.; Pandey, U. K.; Termine, R.; Omenat, A.; Barberá, J.; Serrano, J. L.; Golemme, A.; Gómez-Lor, B. High Charge Mobility in Discotic Liquid-Crystalline Triindoles: Just a Core Business? Angewandte Chemie 2011, 123 (32), 7537-7540.
- (24) Möller, M.; Wendorff, J.; Werth, M.; Spiess, H. W. The nature of the glass transition in a columnar hexagonal ordered phase. Journal of non-crystalline solids 1994, 170 (3), 295-299.
- (25) Heiney, P. A. Datasqueeze: A software tool for powder and small-angle X-ray diffraction analysis. Newsletter of the IUCr Commission on Powder Diffraction 2005, 32, 9-11.
- (26) Prasad, S. K.; Rao, D. S.; Chandrasekhar, S.; Kumar, S. X-Ray studies on the columnar structures of discotic liquid crystals. Molecular Crystals and Liquid Crystals 2003, 396 (1), 121-139.
- (27) Fontes, E.; Heiney, P. A.; Ohba, M.; Haseltine, J. N.; Smith III, A. B. Molecular disorder in columnar-phase discotic liquid-crystal strands. Physical Review A 1988, 37 (4), 1329.
- (28) McMillan, W. L. Simple molecular model for the smectic A phase of liquid crystals. Physical Review A 1971, 4 (3), 1238.
- (29) McMillan, W. X-ray scattering from liquid crystals. I. Cholesteryl nonanoate and myristate. Physical Review A 1972, 6 (3), 936.
- (30) Chen, Z.; Huang, C.; Yao, X.; Benmore, C. J.; Yu, L. Structures of glass-forming liquids by x-ray scattering: Glycerol, xylitol, and D-sorbitol. The Journal of Chemical Physics 2021, 155 (24), 244508.
- (31) Simon, S.; Sobieski, J.; Plazek, D. Volume and enthalpy recovery of polystyrene. Polymer 2001, 42 (6), 2555-2567.

- (32) Grigoriadis, C.; Haase, N.; Butt, H. J.; Müllen, K.; Floudas, G. Negative thermal expansion in discotic liquid crystals of nanographenes. Advanced Materials 2010, 22 (12), 1403-1406.
- (33) Wang, L.-M.; Tian, Y.; Liu, R.; Richert, R. Calorimetric versus kinetic glass transitions in viscous monohydroxy alcohols. The Journal of chemical physics 2008, 128 (8), 084503.
- (34) Bishop, C.; Chen, Z.; Toney, M. F.; Bock, H.; Yu, L.; Ediger, M. Using Deposition Rate and Substrate Temperature to Manipulate Liquid Crystal-Like Order in a Vapor-Deposited Hexagonal Columnar Glass. The Journal of Physical Chemistry B 2021, 125 (10), 2761-2770.
- (35) Bishop, C.; Bagchi, K.; Toney, M. F.; Ediger, M. Vapor deposition rate modifies anisotropic glassy structure of an anthracene-based organic semiconductor. The Journal of Chemical Physics 2022, 156 (1), 014504.
- (36) Seddon, J. M. Structural studies of liquid crystals by X-ray diffraction. Handbook of liquid crystals 1998, 1, 635-679.
- (37) Hodge, I. M. Enthalpy relaxation and recovery in amorphous materials. Journal of Non-Crystalline Solids 1994, 169 (3), 211-266.

Chapter 6

Future work

Contributions from this dissertation fall into two areas: (1) Surface enrichment of components in amorphous solid dispersions and (2) Control of liquid-crystalline order in organic glasses. This chapter suggests future work that builds on these contributions.

6.1 Effects of surface enrichment of surfactants on surface crystallization and wetting

Surface characteristics significantly influence formulation performance of amorphous solid dispersions (ASDs). The surface diffusion rate can be orders of magnitudes faster than the bulk diffusion rate, thus facilitating rapid surface crystallization. Once crystallized, the dissolution advantages of ASDs will be lost. A hydrophobic surface is poorly wetted, resulting in slow dissolution.

In Chapter 2, we have shown that surfactants can be strongly enriched at the surface of ASDs,² but little is known about the impact of surface enrichment on surface crystallization, including surface nucleation and crystal growth. One hypothesis is that a surfactant is typically more mobile than a drug and its enrichment in the surface layer will enhance local mobility³ and accelerate crystallization. Another possibility is that the surface enrichment of surfactants slows down the surface nucleation rate because it dilutes the local drug concentration or disrupts the preferred orientation that promotes surface nucleation.⁴ Thus the intriguing question arises: how does the surface enrichment of surfactants influence surface nucleation and crystal growth?

For wetting, it is anticipated that the surface enrichment of surfactants would lead to reduced wetting because of the exposed hydrophobic tails at the surface. Hence, it's valuable to investigate how it influences wetting, and to establish guidelines for surfactant selection for optimizing wetting characteristics.

A potential model system is posaconazole (POS) doped with surfactants. Recent work has shown that the surface molecules of POS exhibit preferred orientation, thus facilitating surface nucleation and selecting a different polymorph from bulk nucleation.⁵ Also, as shown in Chapter 2, the surface of POS can be strongly enriched with the surfactant Span 80.² The samples will be prepared by melting-quenching. A control surface without surface enrichment will be prepared by melting-quenching the material between two coverslips and peeling off the top one after vitrification. In other words, we can create surfaces with different surfactant concentration, while maintaining the same bulk composition. For a similar surfactant, Span 20, we anticipate a lower degree of surface enrichment,² so a useful comparison will be conducted using Span 80 and Span 20.

The surface crystal growth rate will be measured by seeding a known polymorph at the surface. The surface nucleation rate will be measured as previously published,⁵ and the polymorph selection will be studied by X-ray diffraction, Raman spectroscopy and differential scanning calorimetry (DSC). For wetting, we will measure the contact angle of a water droplet on the flat surface. Considering the highly hydrophobic surface of POS, a ternary ASD of POS doped with surfactants and hydrophilic polymer, poly vinyl pyrrolidone (PVP), can exaggerate the wetting differences between surfaces with or without surface enrichment of surfactants.

The results will provide insight into two critical aspects of ASD development: stability and dissolution. The data are expected to answer whether surface enrichment of surfactants

accelerates surface crystallization, thus leading to poor physical stability, and whether it leads to reduced wetting by increasing surface hydrophobicity. This enhanced understanding will aid in establishing guidelines for surfactant selection in the development of high-quality ASDs.

6.2 Surface distribution of surfactant enrichment in amorphous solid dispersion

While X-ray photoelectron spectroscopy

(XPS) has been employed to quantify the surface enrichment of surfactants, little is known regarding the uniformity of surfactant distribution on the surface, that is, whether the surfactant is uniformly dispersed on the surface or forms localized domains.

For polymer blends, the surface pattern induced by (bulk) phase separation has been characterized by atomic force microscopy (AFM). For example, Figure 1 shows the surface pattern of poly vinyl methyl ether (PVME) doped with 30 wt% deuterated poly styrene (PS) determined by AFM.⁶ Induced by bulk phase separation, the surface shows

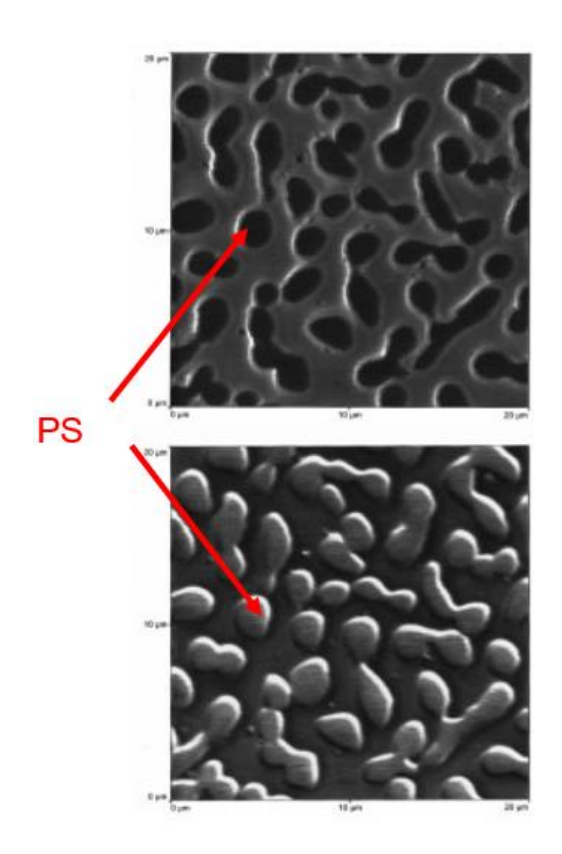


Figure 1. AFM determined the surface pattern of PVME doped with 30 wt % deuterated PS by friction (top) and compliance (bottom). AFM pictures are from Ref. 6.

a heterogenous pattern. The PS domain is glassy at the ambient temperature because its T_g is higher than the ambient temperature, while the PVME domain is a liquid under the same condition due to its low T_g . This distinction in T_g between the two domains results in a sharp contrast in terms of friction and compliance (Figure 1), which can be characterized by AFM.

The surfactant has a much lower $T_{\rm g}$ than the ambient temperature, whereas the amorphous drug has a higher $T_{\rm g}$ than the ambient temperature. Therefore, if there are surfactant-rich domains at the surface, they will be liquid-like, while the drug-rich domains will be glass-like. This distinction between a glass and a liquid will be observable under AFM.

The possible model system can be Posaconazole (POS) doped with surfactants. First, we will establish an AFM method to differentiate between the liquid-like surfactant and the glass-like amorphous drug by measuring the pure materials. Once the methodology is developed, we will measure amorphous POS doped with different concentrations of Span 80 to determine whether the surfactant is uniformly distributed or whether there exist localized domains of surfactant enrichment. We will also use a similar surfactant, Span 20, for comparison, as it is expected to exhibit lower surfactant enrichment. Furthermore, a polymer additive, PVP will be added to determine how the addition of hydrophilic polymer affects the surface distribution of surfactant enrichment.

The results will answer whether the surfactant enrichment is distributed uniformly on the surface at a sub-micron level. If there are surfactant-rich domains, this study can promote understanding about the domain size, and its dependence on composition, polymer additive, and the degree of surface enrichment. The heterogenous surface can lead to poor physical stability and an unstable interface during dissolution. This study will provide insight into surfactant selection and surface engineering for the development of high-quality ASDs.

6.3 Aging of glasses created by multiple kinetic arrests

In Chapter 4 and Chapter 5, we have discovered the multiple kinetic arrests of liquid-crystalline (LC) structure in molecular glasses.^{7,8} For a rod-like molecule, itraconazole (ITZ), we

observe two fictive temperatures T_f s in a glass, with the higher T_f associated with the regularity of smectic layers and lateral packing, while the lower value associated with enthalpy and the molecular spacings between and within smectic layers. Similarly, for a disc-like molecule, PNP, two T_f s are observed in its glass: the higher T_f corresponds to the kinetic arrest of columnar and π -stacking packing, while the lower T_f corresponds to that of enthalpy and π - π spacing.

During aging, a glassy structure evolves towards equilibrium. Previous work glass aging typically assumes that each glass has a single $T_{\rm f}$. Successful models have been developed to predict the evolution of the $T_{\rm f}$ toward equilibrium. For a glass with two $T_{\rm f}$ s, how does each $T_{\rm f}$ evolve during aging? Will the evolution be described by the previous models? Furthermore, for each structural feature, we seek to determine which mode controls the aging process. For the systems investigated in Chapters 4 and 5, the double $T_{\rm f}$ s are determined by the kinetic arrests of two distinct relaxation modes (δ and α). Will the aging rates reflective of the two relaxation modes?

The model systems can be itraconazole (ITZ), simeconazole (SAP) and PNP. The evolution of enthalpy during aging will be measured by DSC and the evolution of the glass structure will be measured by X-ray scattering as previously published.⁷ This will enable the determination of the two fictive temperatures as a function of aging time.

Figure 2 shows the preliminary results of the glass aging of saperconazole (SAP). The glass was prepared by cooling at 0.5 K/s. During aging (top panel), the smectic scattering peak area A_1 grows and its position q_1 shifts to the right. After the aging experiment, the glass was heated to the liquid state (bottom panel) to enable the determination of the T_f values for q_1 and A_1 . Figure 3 shows the evolutions of three fictive temperatures for enthalpy (H), 11 q_1 and A_1 . Of the three properties, the kinetic arrests of H and q_1 are associated with the faster relaxation mode τ_{α} , and that of A_1 with the slower mode τ_{α}^7 The $T_{\rm f}$ s for H and q_1 begin at similar values and reach equilibrium after approximately the same time, but their paths to equilibrium are different. This situation seems analogous to the evolution of polystyrene's volume and enthalpy during aging.⁹ The evolution of enthalpy agrees reasonably well with the AGV prediction (dotted curve). 12,10 For smectic order A_1 , the T_f was initially higher than those of q_1 and enthalpy and during aging, it decreases rapidly, corresponding to a surge of

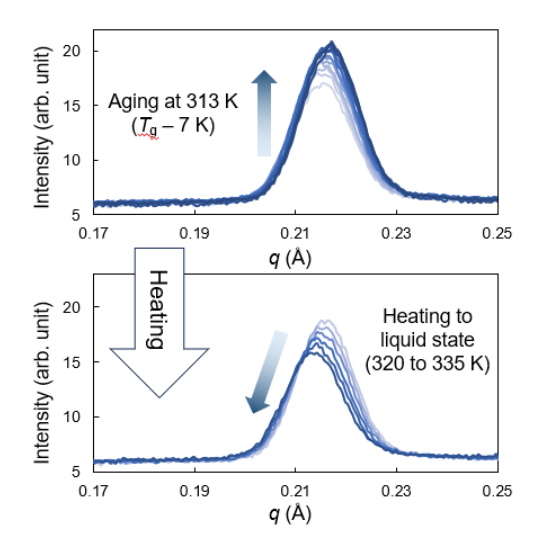


Figure 2. X-ray scattering patterns of a SAP glass prepared by cooling at 0.5 K/s during aging at 313 K (top) and subsequent heating to the liquid state (bottom).

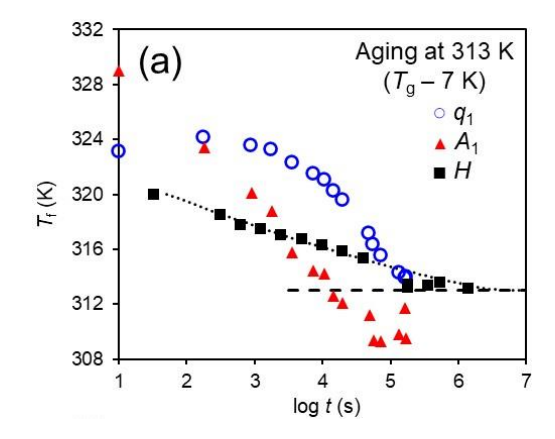


Figure 3. Evolution of three fictive temperatures $T_{\rm fS}$ for enthalpy (H), position of the smectic peak (q_1) , and area of the smectic peak (A_1) during the aging of a SAP glass at 313 K. The horizontal line at 313 K indicates the equilibrium position. The dotted line through the enthalpy data is the prediction of the AGV model.

smectic order, and even goes below the expected equilibrium value (313 K, the aging temperature). Future work is necessary to determine whether it eventually returns to 313 K. The results obtained in this area will help understand the aging of an anisotropic glass with multiple fictive temperatures and the impact on its applications in organic electronics and pharmaceutics.

6.4 References

- (1) Yu, L. Surface mobility of molecular glasses and its importance in physical stability. *Advanced Drug Delivery Reviews* 2016, *100*, 3-9.
- (2) Yu, J.; Li, Y.; Yao, X.; Que, C.; Huang, L.; Hui, H.-W.; Gong, Y.; Qian, F.; Yu, L. Surface Enrichment of Surfactants in Amorphous Drugs: An X-ray Photoelectron Spectroscopy Study. *Molecular Pharmaceutics* 2022, *19* (2), 654-660.
- (3) Li, Y.; Yu, J.; Tan, X.; Yu, L. Surface Mobility of Amorphous Indomethacin Containing Moisture and a Surfactant: A Concentration—Temperature Superposition Principle. *Molecular Pharmaceutics* 2022, *19* (8), 2962-2970.
- (4) Yao, X.; Liu, Q.; Wang, B.; Yu, J.; Aristov, M. M.; Shi, C.; Zhang, G. G.; Yu, L. Anisotropic Molecular Organization at a Liquid/Vapor Interface Promotes Crystal Nucleation with Polymorph Selection. *Journal of the American Chemical Society* 2022, *144* (26), 11638–11645.
- (5) Yao, X.; Borchardt, K. A.; Gui, Y.; Guzei, I. A.; Zhang, G. G.; Yu, L. Surface-enhanced crystal nucleation and polymorph selection in amorphous posaconazole. *The Journal of Chemical Physics* 2022, *157* (19).

- (6) Karim, A.; Slawecki, T.; Kumar, S.; Douglas, J.; Satija, S.; Han, C.; Russell, T.; Liu, Y.; Overney, R.; Sokolov, J. Phase-separation-induced surface patterns in thin polymer blend films. *Macromolecules* 1998, *31* (3), 857-862.
- (7) Yu, J.; Chen, Z.; Teerakapibal, R.; Benmore, C.; Richert, R.; Yu, L. Structures of glasses created by multiple kinetic arrests. *The Journal of Chemical Physics* 2022, *156* (8), 084504.
- (8) Yu, J.; Chen, Z.; Fatina, C.; Chatterjee, D.; Bock, H.; Richert, R.; Voyles, P.; Ediger, M.; Yu, L. Engineering the glass structure of a discotic liquid crystal by multiple kinetic arrests. *The Journal of Chemical Physics* 2023, *158* (20).
- (9) Simon, S.; Sobieski, J.; Plazek, D. Volume and enthalpy recovery of polystyrene. *Polymer* 2001, 42 (6), 2555-2567.
- (10) Hadač, J.; Slobodian, P.; Říha, P.; Saha, P.; Rychwalski, R.; Emri, I.; Kubát, J. Effect of cooling rate on enthalpy and volume relaxation of polystyrene. *Journal of non-crystalline solids* 2007, *353* (28), 2681-2691.
- (11) Moynihan, C. T.; Easteal, A. J.; De Bolt, M. A.; Tucker, J. Dependence of the fictive temperature of glass on cooling rate. *Journal of the American Ceramic Society* 1976, *59* (1-2), 12-16.
- (12) Hodge, I. Adam-Gibbs formulation of nonlinearity in glassy-state relaxations. *Macromolecules* 1986, *19* (3), 936-938.